ROMA TRE
UNIVERSITÀ DEGLI STUDI

SCUOLA DOTTORALE IN SCIENZE
MATEMATICHE E FISICHE

XXIV CICLO

Optimal identification of volcanic noise source using integral methods

Federico Di Paolo

Tutor: Prof. Roberto Scandone

Supervisor: Prof. Umberto Iemma

Coordinatori: Prof. Guido Altarelli
Prof. Orlando Ragnisco

Contents

List of Figures

List of Tables

Introduction

The measurement of dynamical parameters connected to a volcanic eruption is an important research topic which can provide important insight about the features and the energy of eruptions.

The development and the final height of an eruptive column during an explosive eruption, are governed by some physical parameters like energy or power depending if plume rises instantaneously or is sustained (Morton *et al.*, 1956; Wilson *et al.*, 1978). Furthermore, eruption column height can be related to the mass eruption rate (Wilson *et al.*, 1980) or volume flux (Sparks *et al.*, 1997) of the ejected magma during a sustained eruption. The knowledge of such physical quantities is necessary to accurately study and forecast the features of the eruptive cloud.

As well demonstrated by the 2010 eruption of Iceland volcano Eyjafjallajökull, a volcanic eruption can have a significative impact on modern society, preventing the air transport even in countries thousands of kilometers away from the volcano. An accurate prediction of eruptive cloud evolution could significantly mitigate the impact of an explosive eruption, both for safety reasons and for air transport.

Many models describe and forecast the evolution of both the volcanic plume and the ash fallout. Such models deals with the Navier-Stokes equations in atmosphere and are usually based on lagrangian (Searcy *et al.*, 1998; Barsotti *et al.*, 2008) or eulerian viewpoints (Macedonio *et al.*, 1988; Costa *et al.*, 2006), or on simplified models of advection-diffusion-sedimentation of particles (Bonadonna *et al.*, 2005; Macedonio *et al.*, 2005). However, all these models need as input some physical parameters connected to the eruption such as column height, mass eruption rate and total erupted mass.

A multidisciplinary monitoring of a volcano could provide an accurate measurement of such parameters. Thermal infrared images (Delle Donne *et al.*, 2006; Scharff *et al.*, 2008) and radar-doppler (Hort and Seyfried, 1998; Seyfried and Hort, 1999) are two useful methods to measure mass eruption rate and gas velocity during an explosive eruption.

Another efficient method for monitoring the activity of a volcano is the recording of infrasonic signals generated during explosions. Among the different information about the explosion obtainable from infrasound, dynamical quantities such as gas-magma velocity and mass flux could be estimated

under suitable conditions. From this point of view, the infrasonic monitoring of an active volcano could be a good method to extract information that can be used as input values for tephra dispersal models. However, the physical process that generates the pressure release during an explosive eruption is still unknown, or at least, not completely understood, and the extraction of physical parameters from an infrasonic signal is ineffective in many cases.

In this PhD thesis are presented a critical review of the theoretical equations used to extract gas velocity and mass eruption rate from an infrasonic signal, and a new inversion methodology to perform an acoustic source characterization from data by means of an integral method.

In the first two chapters the features of infrasonic monitoring of active volcanoes and the equations of linear acoustics used in data interpretation are illustrated.

In the third chapter the limitations connected to the measurement of infrasonic signal are accurately described, integrated by a critical review of the commonly used formulas in data analysis. By means of theoretical considerations and data analysis, the validity of simple acoustic relationships between physical quantities is investigated, pointing out that the actual cases of applicability of such relationships are rather sparse.

Such study demonstrated the need to perform accurate experiments and numerical simulations to gain some insight about the physical process at the base of sound generation during a volcanic explosion. Only in such condition it could be possible to confidently obtain dynamical parameters connected to the explosion from acoustic recordings.

In order to extract some information about the acoustic source in a strombolian explosion, an inversion model was performed on actual data collected at Stromboli volcano (Italy). A relationship connecting pressure at microphone to source condition at volcanic vent was defined in terms of a *transfer matrix*. Such transfer matrix contains the whole effect of volcano topography and acoustic propagation.

An integral representation based on a Boundary Element Method was used to extract the transfer matrix. The solution, expressed in terms of a normal derivative of acoustic pressure at the source, was obtained by two different methods: an analytical solution, enabled by the use of a symmetric geometry, and a *optimal solution* from a *Pareto set* based on an *Adaptive Weighted-Sum* optimization method (Kim and de Weck, 2005).

The optimization procedure represents a method to find the "best values" for a given set of variables that satisfy a determined condition. Since the optimization method has a general validity in terms of geometry complexity and number of parameters involved, this work permitted to test the accuracy of the optimal solution, by a comparison with the analytical solution that was obtained thanks to an approximated geometry.

Chapter 4 illustrates the integral method used, the extraction of the

transfer matrix, and the achievement of both the analytical and the optimal solutions. A description of approximations and limits of the linear acoustics is included, for an accurate interpretation of results.

In Chapter 5, results from the inversion are presented. In order to check the reliability of such methodology, a validation by means of a different integral method was performed, proving both the quality and the limitations of our inversion and suggesting possible ways to perform further refinements.

The good agreement between solutions obtained from the two methodologies make us confident about the validity of the optimization, enabling the use of it for future improvement in the methodology, for which an analytical solution can not be obtained.

On the basis of our results, an accurate source characterization from infrasonic data can be possible, by using the actual geometry of the volcano and an adequate number of microphones.

Chapter 1

Infrasound emitted by explosive eruptions

1.1 Overview on volcano acoustics

Explosive volcanic eruptions consist in a violent emission of a mixture of magma and gases at high temperature and pressure. Depending on the percentage of gas, magma rheology and thermodynamic conditions inside the conduit, magma can escape from the volcanic vent with different degrees of fragmentation, resulting in a large spectrum of eruption violence and intensity (Scandone and Giacomelli, 1998).

The intense decompression associated to the emission of gas and magma during an explosive eruption is always accompanied by a release of energy in form of earthquakes (propagating inside rocks) and pressure waves in the acoustic and (mainly) in the infrasonic band ($\nu < 20$ Hz), propagating in the free air.

Huge volcanic blasts like those of Krakatau (1883), Mount St. Helens (1980) or Pinatubo (1991) generated very long period acoustic-gravity waves that traveled in atmosphere and were registered at distance of thousands of kilometers (Donn and Balachandran, 1981; Mikumo and Bolt, 1985; Tahira *et al.*, 1996).

In the last decades the monitoring of explosive processes by the registration and interpretations of infrasonic waves have been considerably improved, since can provide some information about the eruptive activity of volcanoes that can be kilometers far away. This operation permits to perform a safe and continuous remote sensing, even during violent eruptions.

First registrations on tape of acoustic sounds generated by volcanic eruptions were made in the early years of the past century at many volcanoes including Vesuvius (Perret, 1950), followed in the subsequent years by measurements of acoustic signals both in water and in air (Foshag and Gonzales-Reyna, 1956; Snodgrass and Richards, 1956; Richards, 1963). In these works

the authors focused on the relationship between an acoustic signature (both from signal shape and frequency spectrum) and a peculiar eruptive style.

The first recording by means of a barograph was performed by Gorshkov in 1960, in order to obtain a measurement of the energy associated to the acoustic wave.

In another paper, Woulff and McGetchin (1976) tried to gather some information about the pressure source and gas velocity considering different types of acoustic source (monopole, dipole and quadrupole).

In the past two decades the monitoring techniques have been improved enormously, and microphones and pressure transducers were used to detect the airwaves in the infrasonic band (Braun and Ripepe, 1993), leading to a world-wide interest in monitoring infrasonic signals from volcanic explosions.

At present, many active volcanoes around the world are monitored in real-time by means of an infrasonic recorder, sometimes in array configuration. The wide use of this technique lies in the ample spectrum of informations obtainable from data analysis:

- discrimination between eruptive styles, and identification of changes in eruption intensity (Ripepe *et al.*, 1996; Vergniolle and Caplan-Auerbach, 2004; Ripepe *et al.*, 2009a; Fee *et al.*, 2010; Johnson *et al.*, 2011);
- source location in multi-vent volcanoes (Ripepe and Marchetti, 2002; Cannata *et al.*, 2009; Marchetti *et al.*, 2009);
- estimation of eruptive dynamics parameters such as gas velocity and mass flux (Firstov and Kravchenko, 1996; Vergniolle *et al.*, 2004; Vergniolle and Caplan-Auerbach, 2006; Johnson, 2007; Caplan-Auerbach *et al.*, 2010);
- location of fragmentation depth, integrating the infrasound with seismic and thermal data (Gresta *et al.*, 2004; Johnson, 2007).

Many authors focused on data analysis, others concentrated in the physics of the problem, that contains both fluid dynamics and acoustics. Buckingham and Garcés (1996) focused on the acoustic theory in order to gain information for a better interpretation of experimental data. Other authors tried to identify the most plausible source by means of numerical simulations (Johnson *et al.*, 2008) or spectral analysis (Matoza *et al.*, 2009). Lacanna (2010) used a bi-dimensional Finite Difference Time Domain method (FDTD) to study the effect of terrain scattering on signal shape. Kieffer and Sturtevant (1984) performed laboratory experiments to study the behavior of volcanic jet in supersonic conditions. Ogden *et al.* (2008) performed numerical simulations on volcanic jets to investigate both the gas-thrust region and the convective plume generated by a supersonic shock. Pelanti (2005)

studied a multicomponent compressible flow at the base of wave propagation by numerical methods.

1.2 Pressure source models

The main goal in volcano acoustics seems to be now the clear understanding of the source process. The wide range of typology for an explosive volcanic eruption points to different physical models describing the explosion. In this work we considered mostly the strombolian eruption, consisting in an impulsive gas thrust phase followed by a gentle plume rise because of buoyancy (Blackburn *et al.*, 1976).

Integrating experimental data with theory, three models were proposed in order to explain the generation of pressure waves during a strombolian explosion:

1. the bursting of gas *slug* at the magma-air interface (Ripepe *et al.*, 1996);

2. the oscillation of a gas bubble before bursting at the free surface (Vergniolle and Brandeis, 1994, 1996);

3. the resonance of waves trapped in the magma column, triggered by a deep pressure drop (Buckingham and Garcés, 1996; Garcés and McNutt, 1997).

The first two are in agreement in terms of a large bubble of gas or *slug* surrounded by a thin magma film exploding at the surface; but, while in the first model the authors connect the pressure pulse directly to the explosion of a gas bubble, in the second is the oscillation of a gas bubble responsible for the pressure release. However, for both models, the origin of volcanic tremor (either seismic and infrasonic) is due to gas bubbles overpressure.

Conversely in the third model an explosion inside the magma column excites the conduit into acoustic resonance, with a resulting pressure field propagating both into the ground and in the free air (Garcés and McNutt, 1997). By this consideration, the generation of the seismic wave field results strictly connected to the acoustic resonance inside the magma body. The authors analyzed pressure recordings both in time and frequency domain, concluding that the main features of signals develops from propagation effects associated to the coherent superposition of normal modes from longitudinal and radial resonances in the magma conduit (Buckingham and Garcés, 1996).

Despite the great diffusion and study of infrasound, the actual source process that leads to the generation of acoustic waves is still unknown. Although infrasonic signals have a direct connection to the source process compared to the seismic ones (because the infrasonic wave travels only in

one medium, the air), it is not possible to accurately reconstruct the actual source, with just one, or in the better cases, some microphones. Moreover, the explosion can occur inside the volcanic conduit at an unknown depth.

In this view, numerical simulations of source condition and propagation effects nearby the vent can provide an accurate method to study what really happens in the first instants of the explosion. Furthermore it can be possible to study the actual effect of some parameters (such as magma density or vent radius) that in most cases are poorly constrained.

1.3 Pressure signals features

Infrasonic signals represent the excess pressure Δp with respect to the atmospheric pressure ($\sim 10^5$ Pa). The excess pressure measured during normal volcanic activity generally range between 10 and 10^2 Pa at a distance of about $10^2 - 10^3$ m from the active vents. Even for paroxysmal explosions pressure perturbations are usually smaller than atmospheric pressure: in this condition infrasound can be treated as a linear elastic wave rather than non-linear shock wave, which allows simplified modeling of the source by using the linear theory of sound. As the frequency associated to infrasound is below 20 Hz, the wavelength associated to this signals will vary in the range of $10 - 10^3$ m.

Signals can assume different shapes, sometimes complicated, but there are some features connected to peculiar eruptive styles:

- impulsive and isolate bubble bursting like strombolian explosions shows a *N-wave* signature (Deihl and Carlson, 1968) lasting less than one second, with a decaying tail of one or more seconds (Figure 1.1A);
- multiple pulsation of strombolian activity and persistent *active degassing* lead to a continuous infrasonic tremor (Figure 1.1B);
- long-lasting fire fountains show signals that can persist for several hours, with a continuous tremor (generated by both the repeated bubble explosions and the fallout of ejecta) overlapped by single pulses;
- *passive degassing* with no emission of magma that shows at Stromboli volcano a typical signature of small amplitude pulses with a period of 1-2 s, called *puffing* (Ripepe *et al.*, 1996; Ripepe and Gordeev, 1999; Figure 1.2);
- explosive eruptions like vulcanian, sub-plinian and plinian can have both huge pressure peaks and long lasting tremor, connected to turbulence inside the volcanic jet or pyroclastic flows (Marchetti *et al.*, 2009; Matoza *et al.*, 2009; Caplan-Auerbach *et al.*, 2010).

Sometimes, the intensity of the eruption leads to the generation of pressure waves in the transonic and supersonic regime, or eventually shock waves, and the linear theory of sound results no more valid for the interpretation of data.

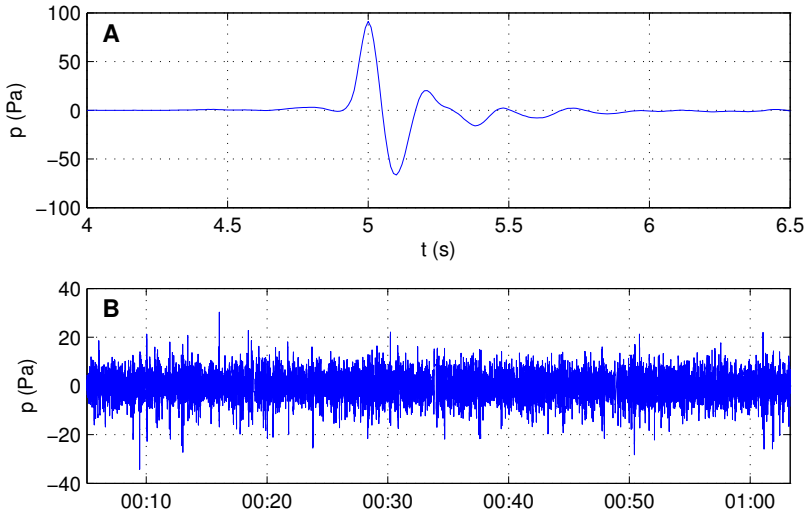

Figure 1.1: A. Impulsive pressure signal generated by strombolian activity at Stromboli volcano (Italy). Stacking of 150 signals recorded at 280 m from the active vent. B. Continuous infrasonic tremor registred at Etna volcano (Italy) at 1 km from the active vent.

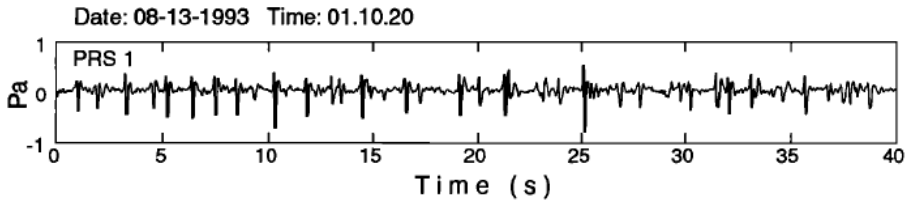

Figure 1.2: Repeated infrasonic transient in a range between 0.8 and 1.2 s associated to small gas bubble bursting at Stromboli volcano (Ripepe and Gordeev, 1999). No transient in the seismic signal are associated to this activity.

Chapter 2

Linear acoustics

2.1 Basic equations of acoustic theory

Propagation of sound waves in a fluid is governed by the balance between compressibility and the inertia of the fluid itself.

The use of a linear theory means that the disturbances in the equations of motion are so weak that we can neglect the products between them, since they will be small quantities.

Let's consider the inertial nature of a fluid of density ρ using the Newton's equation of motion applied to a small fluid element: in absence of external forces the acceleration will be due solely to the internal stresses between the fluid element and the neighboring fluid around it, represented by the gradient of fluid pressure ∇p:

$$\rho \left(\frac{\partial \mathbf{u}}{\partial t} + \mathbf{u} \cdot \nabla \mathbf{u} \right) = -\nabla p. \tag{2.1}$$

The acceleration of a fluid element depends on two terms: the first, $\partial \mathbf{u}/\partial t$ represents the local change of velocity $\mathbf{u}$ at a fixed point; the second *non linear*, $\mathbf{u} \cdot \nabla \mathbf{u}$ describes the changes in velocity of fluid element due to its changes in position in space.

Related to the equation of motion, the equation of continuity governs the changes in density of a fluid element (compressibility):

$$\frac{\partial \rho}{\partial t} + \mathbf{u} \cdot \nabla \rho + \rho \nabla \cdot \mathbf{u} = 0, \tag{2.2}$$

where the first two terms in (2.2) represent together the total change of density for a fluid element.

Since we are interested in a linearization of these equations, we will consider as "small quantities" all departures from an equilibrium state in which the fluid is at rest with a uniform density ρ_0 (Lighthill, 1978). In the absence of external forces also pressure will take a uniform value p_0.

Considering neglectable the terms $\mathbf{u} \cdot \nabla \mathbf{u}$ in (2.1) and $\mathbf{u} \cdot \nabla \rho$ in (2.2), and replacing ρ with ρ_0, the basic equations of linear acoustics will become

$$\rho_0 \frac{\partial \mathbf{u}}{\partial t} = -\nabla p, \tag{2.3}$$

and

$$\frac{\partial \rho}{\partial t} = -\rho_0 \nabla \cdot \mathbf{u}. \tag{2.4}$$

As a consequence of equation (2.3), the vorticity field defined as

$$\mathbf{\Omega} = \nabla \times \mathbf{u}, \tag{2.5}$$

will be independent of time. In fact as long as the curl of ∇p is zero, equation (2.3) implies that

$$\frac{\partial \mathbf{\Omega}}{\partial t} = 0. \tag{2.6}$$

As the rotational part of the velocity field related to $\mathbf{\Omega}$ is independent of time, the remaining part of the velocity field will be irrotational and, according to the Helmholtz's theorem, it can be written as the gradient of a scalar, the "velocity potential":

$$\mathbf{u} = \nabla \phi. \tag{2.7}$$

The fluctuations associated to the sound propagation will affect only this quantity. On linear theory this irrotational propagating velocity field shows no interaction with any steady rotational flow field (Lighthill, 1978).

Inserting (2.7) in equation (2.3), and considering the properties of the gradient operator we have:

$$p - p_0 = -\rho_0 \frac{\partial \phi}{\partial t}. \tag{2.8}$$

This is an expression of the *Bernoulli equation* for unsteady irrotational flows with the absence of the term $-\frac{1}{2}\rho_0(\nabla\phi)^2$, negligible on a linear theory.

Inserting (2.7) in equation (2.4), changes in density can be connected to the Laplacian of the velocity potential:

$$\frac{\partial \rho}{\partial t} = -\rho_0 \nabla^2 \phi. \tag{2.9}$$

The linearization of the theory comes out form the explicit relationship between changes of pressure and density: assuming the functional dependence $p = p(\rho)$, and expanding p in Taylor series about $\rho = \rho_0$, we'll have:

$$p = p(\rho_0) + (\rho - \rho_0)p'(\rho_0) + ... \tag{2.10}$$

Now, neglecting all the terms with order higher than $\rho - \rho_0$:

$$\frac{\partial p}{\partial t} = p'(\rho_0)\frac{\partial \rho}{\partial t}. \tag{2.11}$$

Inserting equation (2.8) in (2.11), and then in equation (2.9) we obtain:

$$\frac{\partial^2 \phi}{\partial t^2} = c^2 \nabla^2 \phi, \tag{2.12}$$

which is the wave equation.

The constant c has the dimension of a velocity and is defined as:

$$c^2 = p'(\rho_0). \tag{2.13}$$

Anyway, to obtain the actual sound speed we must consider some thermodynamic effects associated to the adiabatic compression of fluid particles during to the propagation of the wave. In doing so, the sound speed c will assume its proper form:

$$c^2 = \gamma \frac{p}{\rho} = \gamma R T, \tag{2.14}$$

where γ for a perfect gas is defined as

$$\gamma = \frac{R + c_v}{c_v}, \tag{2.15}$$

with R and c_v being the gas constant (8314 J $\mathrm{K}^{-1}\mathrm{kmol}^{-1}$) and the isochoric specific heat.

Equation (2.12) describes a propagation in a homogeneous medium at a single wave speed c independent of waveform and direction of propagation. Such an equation has a generic solution in the form

$$\phi(\mathbf{x}, t) = f(\mathbf{x} - ct) + g(\mathbf{x} + ct), \tag{2.16}$$

in which $f(\mathbf{x} - ct)$ and $g(\mathbf{x} + ct)$ are two plane waves propagating in opposite directions.

Acoustic intensity

Since sound waves transport energy without the need for transporting any material, the acoustic energy associated to a sound wave is usually described by the *acoustic intensity* I, which means the rate of transport of energy through unit area.

Acoustic intensity is a vector quantity defined as the product of pressure perturbation Δp and particle velocity $\mathbf{u}$

$$\mathbf{I} = \Delta p \ \mathbf{u}, \tag{2.17}$$

where Δp is the departure from equilibrium pressure p_0:

$$\Delta p = p - p_0. \tag{2.18}$$

For a traveling plane wave with solution $\phi = f(x - ct)$, equations (2.7) and (2.8) give

$$\Delta p = \rho_0 c u, \tag{2.19}$$

then the acoustic intensity can be related to the square of particle velocity:

$$I = \rho_0 c u^2. \tag{2.20}$$

Acoustic intensity can be measured in W m^{-2}, but because of its wide range of variability (human ear is sensible to pressure variations, not to the absolute value of pressure itself), a logarithmic scale proves more accurate. So I is usually expressed in a *decibel* scale, in comparison to a reference level:

$$\begin{aligned} I(\text{dB}) &= 10 \log_{10} \left(\frac{I}{I_0} \right) \\ &= 10 \log_{10}(I) + 120, \end{aligned} \tag{2.21}$$

wiht I_0 being the standard reference sound intensity

$$I_0 = 10^{-12} \text{ W m}^{-2}. \tag{2.22}$$

Another frequently used quantity is the *sound pressure level* (*SPL*), which represents the deviation from the ambient pressure caused by a sound wave:

$$\begin{aligned} SPL(\text{dB}) &= 10 \log_{10} \left(\frac{\Delta p^2}{p_0^2} \right) \\ &= 20 \log_{10} \left(\frac{\Delta p}{p_0} \right), \end{aligned} \tag{2.23}$$

where p_0 is a reference sound pressure p_0 which in air has a value of 20 μPa and is considered as the threshold of human hearing at the frequency of 1 kHz.

2.2 Acoustic sources

In acoustic theory there are three kinds of sources: monopole (or simple source), dipole and quadrupole. Actually there can be poles of still higher order, conveniently described in terms of Hankel and Legendre functions (Morse and Ingard, 1968), though they have less practical interest. Since in volcano acoustics these kind of sources are not commonly used, they will not be considered here.

Monopole is the simplest source, point-like and expanding radially in all directions. Dipole is a combination of two monopoles of the same intensity and opposite sign positioned at small distance to each other compared to the source-receiver distance. Quadrupole is a combination of two dipoles, and can assume different configurations.

In the next subsections are shown the main features of these sources, introducing some physical quantities useful for data analysis.

2.2.1 Simple source

Monopole is the elementary acoustic source, a point-like source expanding spherically without any directional nature. The strength of the source is related to a mass acceleration and can be physically represented by a sudden burst of a balloon. In three dimensions the excess pressure for a simple source is given by:

$$\Delta p(t) = \frac{\dot{q}(t - r/c)}{4\pi r}, \tag{2.24}$$

where $q(t)$ has the dimensions of a rate of mass outflow from the source (kg s^{-1}).

As one can see, pressure perturbation decay with distance as r^{-1}. As mass injection have to be instantaneous, pressure signal will be (ideally in three dimensions) composed by a single oscillation around the equilibrium pressure (and pressure perturbation Δp will oscillate around zero) as in Figure 2.1. Pressure signal has a clear time delay between the source event, due to the propagation of the signal at the sound speed c. By now the time dependency will be omitted.

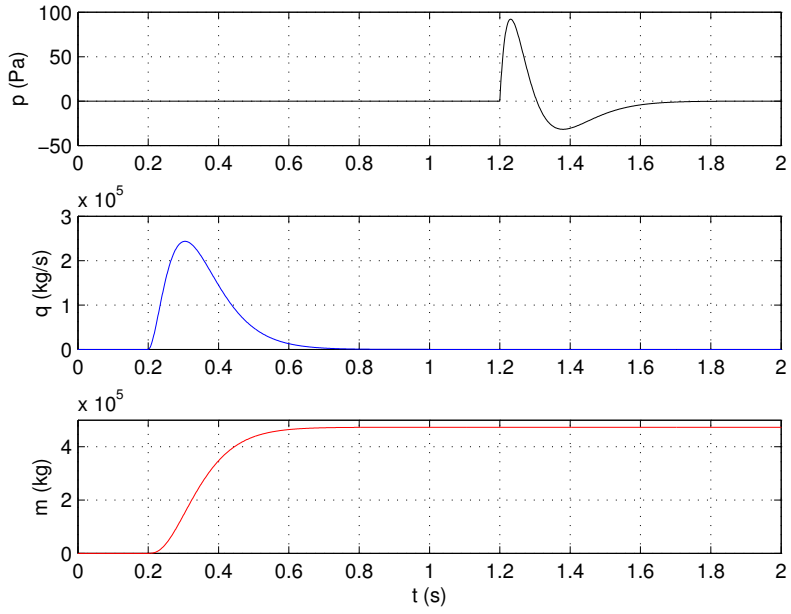

Figure 2.1: Mass outflow and pressure perturbation generated by the source $q(t)$. Pressure perturbation has the shape of a *blast wave* (Reed, 1977). The time delay of 1 s for the pressure perturbation is due to a distance of 340 m from the source.

Since we want to calculate acoustic power, we have to consider the acous-

tic intensity I. In the *far field condition* (2.31), I is related to the radial velocity of fluid; inserting the (2.19) in the (2.20), I can be written as

$$I = \frac{1}{\rho_0 c}\Delta p^2, \tag{2.25}$$

with ρ_0 being the density of medium.

In order to calculate acoustic power we have to integrate I over a sphere of radius r. In doing this, power Π emitted by a monopole will be:

$$\Pi = \frac{4\pi r^2}{\rho_0 c}\Delta p^2 = \frac{\dot{q}^2}{4\pi\rho_0 c}. \tag{2.26}$$

This quantity represents the power output generated by the source and passing after a time delay r/c through the area $4\pi r^2$ at a distance r from the source. Figure 2.2 shows the radiation pattern generated by a monopole. Amplitude decay due to geometrical spreading is evident.

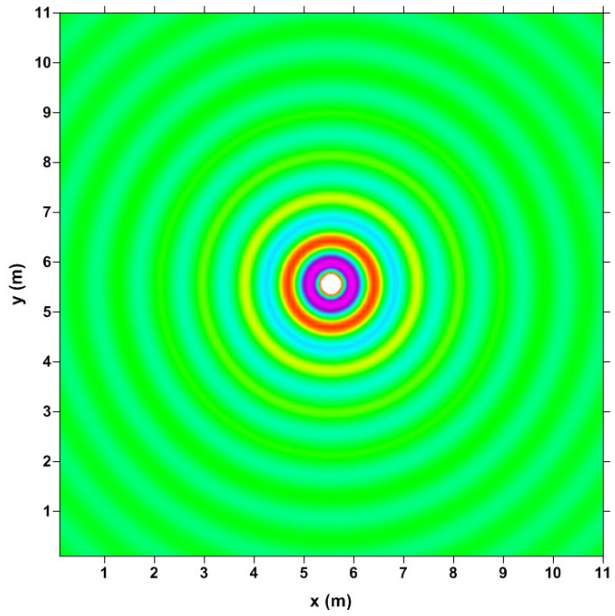

Figure 2.2: Monopole radiation pattern for an oscillating source with a frequency of 400 Hz calculated by the code AcouSTO.

2.2.2 Dipole source

Dipole source is a system composed by two coupled simple sources with the same intensity and opposite sign in an infinite space:

$$\Delta p(t) = \frac{\dot{q}(t - r/c)}{4\pi r} - \frac{\dot{q}(t - r'/c)}{4\pi r'}, \tag{2.27}$$

where r and r' are the distances of the two simple sources from the point P (Figure 2.3). If the distance l between the two sources is small compared to r and r', the difference $(r' - r)$ can be approximated with $l \cos\theta$. In this condition the difference between the two monopole terms in (2.27) can be expressed in terms of a derivative with respect to r (Lighthill, 1978):

$$\Delta p(t) = l \cos\theta \frac{\partial}{\partial r} \left[\frac{\dot{q}(t - r/c)}{4\pi r} \right]. \tag{2.28}$$

Calculating the derivative we have:

$$\Delta p(t) = l \cos\theta \left[\frac{\dot{q}(t - r/c)}{4\pi r^2} + \frac{\ddot{q}(t - r/c)}{4\pi r c} \right]. \tag{2.29}$$

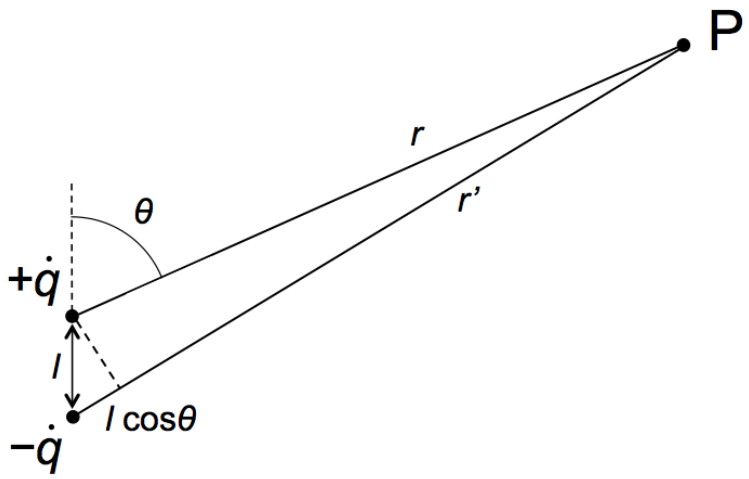

Figure 2.3: Dipole source geometry. If $r \gg l$ it is possible the approximation $r' \approx r$.

This approximation is valid if the derivative varies by only a small fraction of itself when r changes by at most l. The limit of applicability is expressed by the *acoustic compactness condition* (Curle, 1955; Lighthill, 1978):

$$l \ll \frac{c}{\omega} = \frac{\lambda}{2\pi}, \tag{2.30}$$

with ω and λ being the pulsation and the wavelength of the acoustic wave. This condition is considered rather important since in general allows the use of elementary sources as monopole and dipole to model more complex systems.

Pressure signal of dipole described by (2.29) is composed by two terms; the first has a quadratic dependency on source-receiver distance, and it is

possible to neglect it for large values of r. This condition, known as the *far field approximation*, is mathematically expressed by

$$r \gg \frac{c}{\omega} = \frac{\lambda}{2\pi}, \tag{2.31}$$

and it is well satisfied in most cases of volcanology.

As one can see, in (2.29) appears the angle θ between the axis of dipole and the position of the receiver (Figure 2.3). So pressure perturbation will be maximum in the direction of dipole axis and zero at right angles. Furthermore, pressure perturbation is negative for angles exceeding 90°(Figure 2.4).

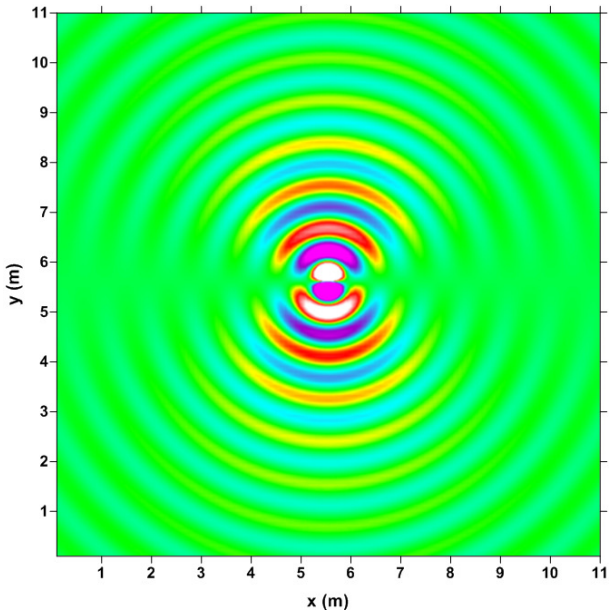

Figure 2.4: Dipole radiation pattern for an oscillating source with a frequency of 400 Hz calculated by the code AcouSTO. Also in proximity of the sources, the field goes to zero at right angles from the dipole axis.

Inserting (2.29) in (2.25) we obtain the acoustic intensity for a dipole source:

$$I = \frac{l^2 \cos^2\theta \; \ddot{q}^2}{16\pi^2 \rho_0 r^2 c^3} \tag{2.32}$$

Integrating equation (2.32) on a sphere of radius r, the power emitted by a dipole source will be:

$$\Pi = \frac{l^2 \ddot{q}^2}{12\pi\rho_0 c^3}. \tag{2.33}$$

It is important to point out that the pressure field generated at distance $r \gg l$ by an acoustically compact dipole is rather small compared to the

pressure fields generated by the two sources separately. Then, the dipole is quite inefficient with respect to a simple source, with a power output inferior for a factor of order $(\omega l/c)^2$.

Sometimes in equation (2.28) is used the notation $G(t) = l\dot{q}(t)$, and this quantity is called the *strength* of the dipole, having the dimensions of a force. Thus, for a general force $\mathbf{G}$, (2.28) becomes:

$$\Delta p(t) = -\nabla \cdot \left[\frac{\mathbf{G}(t - r/c)}{4\pi r}\right]. \tag{2.34}$$

In this way, it is possible to relate the properties of a dipole to a force generating a rate of change of momentum in the external fluid, as the monopole is associated to a rate of change of mass outflow into the external fluid.

2.2.3 Quadrupole source

A compact source radiating sound in a condition that both the total monopole and dipole strength are zero is called quadrupole. This kind of radiation is typically associated to turbulent flows separated from any foreign body that can act on the air with some forces (Lighthill, 1978). Physically, a quadrupole can be obtained by two dipoles coupled together, and can assume different geometric configurations (Figure 2.5).

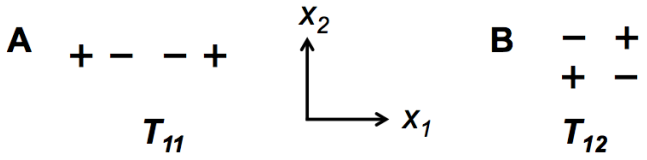

Figure 2.5: Quadrupole source geometries for different configurations: A. Longitudinal quadrupole; B. Lateral quadrupole.

In the far field the sound generated by a quadrupole is significantly weak compared to that of the individual dipoles. So, although the dipole source is less efficient with respect to the simple source, is still more efficient than a quadrupole. This does not mean that the quadrupole far field (in absence of other simple sources) has no consequences, in fact the turbulent *jet noise* generated by aircrafts has its peculiarities (Lighthill, 1963; Tam *et al.*, 1996; Tam, 1998) and is studied to mitigate the impact on the human ear, for the people living near airports (Caves *et al.*, 1997; Manneville *et al.*, 2004; Diez *et al.*, 2007; Barbot *et al.*, 2008).

Since the strength of a quadrupole involves two directions (orientation and displacement between the two coupled dipoles) it is a *tensor* quantity. So we must consider this nature and modify the previous equations for linear acoustics.

If we express the vectors position and velocity as $\mathbf{x} = (x_1, x_2, x_3)$ and $\mathbf{u} = (u_1, u_2, u_3)$, and we use the *Einstein notation* (summing for a index appearing twice), we can express equations (2.1) and (2.2) for the i-th component as

$$\rho \frac{\partial u_i}{\partial t} + \rho u_j \frac{\partial u_i}{\partial x_j} + \frac{\partial p}{\partial x_i} = 0, \tag{2.35}$$

and

$$\frac{\partial \rho}{\partial t} + \frac{\partial (\rho u_j)}{\partial x_j} = 0. \tag{2.36}$$

Now, multiplying equation (2.36) by u_i, and inserting it in equation (2.35), we have:

$$\frac{\partial (\rho u_i)}{\partial t} + \frac{\partial (\rho u_i u_j)}{\partial x_j} + \frac{\partial p}{\partial x_i} = 0. \tag{2.37}$$

Using the properties of the *Kronecker delta*, δ_{ij}, we can express equation (2.37) as:

$$\frac{\partial (\rho u_i)}{\partial t} + \frac{\partial}{\partial x_j} \left[\rho u_i u_j + (p - p_0)\delta_{ij} \right] = 0 \tag{2.38}$$

The term in square brackets in (2.38) represents a *total momentum flux* tensor equal to the rate of transport of the i-th component of the momentum in the j-th direction, due to convection by the j-th component of velocity and action of the excess pressure $p - p_0$. The rate of change of the i-th component of momentum in an elementary region is equal to minus the integrated action of that total flux across the region's surface (Lighthill, 1978).

The form of (2.38) is useful to understand the generation of sound by turbulent fluid flows, as represents the connection between linear acoustics and fluid dynamics. Neglecting the product of small quantities like $u_i u_j$ as discussed before, and transforming the pressure perturbation in $c^2(\rho - \rho_0)$ according to (2.10) and (2.13), equation (2.38) becomes:

$$\frac{\partial (\rho u_i)}{\partial t} + c^2 \frac{\partial \rho}{\partial x_i} = 0. \tag{2.39}$$

Now, performing the derivative operation $\partial / \partial x_i$, and substituting equation (2.36) in (2.39), we obtain

$$\frac{\partial^2 \rho}{\partial t^2} - c^2 \frac{\partial^2 \rho}{\partial x_i^2} = 0, \tag{2.40}$$

that is the linear wave equation in absence of forcing terms (which implies no radiation of sound). Since the sound radiation in a fluid flow is caused by departure of the total momentum flux, we can write this contribution as:

$$T_{ij} = \rho u_i u_j + \left[(p - p_0) - c^2(\rho - \rho_0) \right] \delta_{ij}. \tag{2.41}$$

Inserting equation (2.41) in (2.38), the momentum equation becomes:

$$\frac{\partial(\rho u_i)}{\partial t} + c^2 \frac{\partial \rho}{\partial x_i} = -\frac{\partial T_{ij}}{\partial x_j}. \tag{2.42}$$

Performing the derivative operation $\partial/\partial x_i$, and considering the continuity equation (2.36), equation (2.42) transforms in:

$$\frac{\partial^2 \rho}{\partial t^2} - c^2 \frac{\partial^2 \rho}{\partial x_i^2} = \frac{\partial^2 T_{ij}}{\partial x_i \partial x_j}. \tag{2.43}$$

The forcing term at the right side of (2.43) is responsible for any generation of sound. This equation is also known as the *Lighthill's acoustic analogy*, and connects directly the acoustic wave propagation to the fluid dynamics described by T_{ij}.

The tensorial nature of T_{ij} give rise to different quadrupole configurations: the diagonal elements correspond to aligned dipoles, called *longitudinal quadrupole* (Figures 2.5A, 2.6A), while the off-diagonal elements corresponds to dipoles separated in a perpendicular directions, called *lateral quadrupole* (Figures 2.5B, 2.6B).

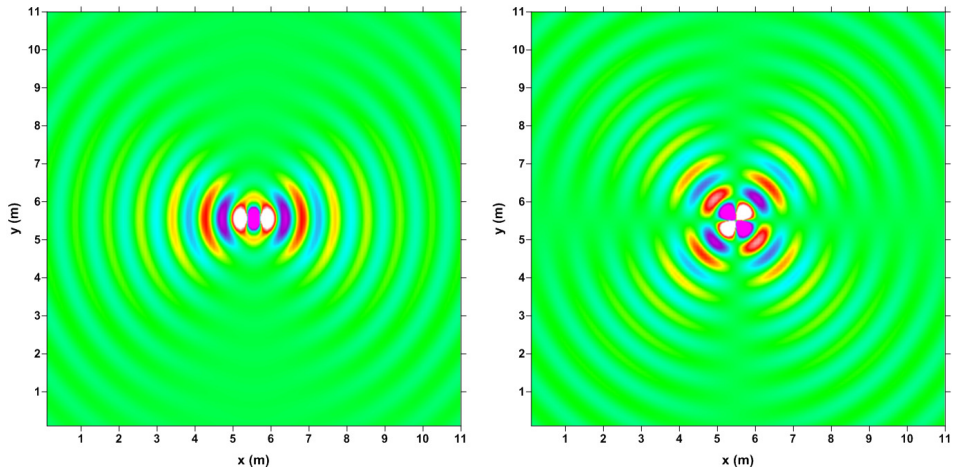

Figure 2.6: Quadrupole radiation pattern for an oscillating source with a frequency of 400 Hz calculated by the code AcouSTO. A. Longitudinal quadrupole with the configuration of Figure 2.5A. B. Lateral quadrupole with the configuration of Figure 2.5B.

A jet involving no fluctuation in mass outflow (monopole) and no external forces on the fluid (dipole), will generate quadrupole radiation associated to the excess momentum flux tensor T_{ij}. The solution of (2.43) will be

$$c^2 \left[\rho(\mathbf{x}) - \rho_0\right] = \frac{\partial^2}{\partial x_i \partial x_j} \int \left[\frac{T_{ij}(\mathbf{y}, t - r/c)}{4\pi r}\right] \mathrm{d}\mathbf{y}, \tag{2.44}$$

where $\mathbf{x}$ is the position vector inside the fluid, $\mathbf{y}$ is the position vector inside the source region where the integration is performed, and r is defined as

$$r = |\mathbf{x} - \mathbf{y}|. \tag{2.45}$$

The corresponding far field of (2.44) will be:

$$c^2 \left[\rho(\mathbf{x}) - \rho_0\right] = \int \left[\frac{r_i r_j \ddot{T}_{ij}(\mathbf{y}, t - r/c)}{4\pi r^3 c^2}\right] \mathrm{d}\mathbf{y}. \tag{2.46}$$

Since T_{ij} depends on u^2, and their characteristic frequency increase like u, T_{ij} will increase like u^4. Thus the far field amplitude will vary like u^4, while the acoustic intensity and power output will vary like u^8. This is the so called *Lighthill's 8 th power law* (Lighthill, 1952, 1954), and is one of the main features of the quadrupole radiation generated by turbulence.

Considering the condition of acoustic compactness for the quadrupole, the quantity l appearing in the (2.30) is the effective size of the eddies that radiate coherently, and the product wl is typically in the order of the root-mean-square velocity fluctuations, which commonly make the compactness condition $wl \ll c$ being satisfied (Lighthill, 1978).

2.3 Acoustic waves in ducts

Since we'll take in consideration actual volcanic systems and pressure signal sometimes generated inside conduits, it is useful to introduce briefly some features of the acoustic waves in ducts.

When a sound wave generated by a piston propagates inside a tube, the ratio between its wavelength λ and the transverse dimension of the pipe a will determine the behavior of the wave. If $\lambda \gg a$, the fluid motion will be mainly parallel to the tube axis, and the wave motion can be treated as one-dimensional. In this condition, there is a close analogy between the duct and an electric transmission line: the total flux of fluid plays the role of the electric current i, and sound pressure p is the analogue of the voltage V; any variation in the cross section of the tube, will be represented as an impedance contrast barrier which will determine the wave propagation (Morse and Ingard, 1968).

Acoustic impedance $\mathcal{Z}$ is a frequency dependent (usually complex) quantity defined as the ratio between sound pressure p and the product of fluid velocity u and the area A in which the wave propagates through:

$$\mathcal{Z} = \frac{p}{uA} = \frac{\rho c}{A}. \tag{2.47}$$

If the tube walls are completely rigid, the wave will not undergo any energy loss, and the amplitude will be maintained without decaying. This

condition leads to a better efficiency in the propagation of sound than in the three-dimensional free space, where the amplitude of a pressure perturbation decays with distance as r^{-1} (Lighthill, 1978). Differently, if the tube walls are not perfectly rigid, or if there are significative effects of viscosity and thermal conduction, the wave will undergo attenuation, although usually the unattenuated part (represented by the real part of the complex quantity $k = 2\pi/\lambda$) will be predominant.

An interesting case, close to the actual volcanic systems, is that of a source (piston) at one side of the tube, in $x = 0$, and the free space at the open end, in $x = l$ (where l is the length of the tube). In this case the pressure distribution across the opening is not uniform, even for long-wavelength sound waves (Morse and Ingard, 1968). It is then possible to assume that the air at the open air acts like a piston, radiating sound out into the free space, as well as reflecting sound back inside the tube. At very long λ, the most of the energy remains trapped inside the tube, and only a little is radiated out. Diminishing the wavelength, more and more sound will escape from the open end of the tube.

The air at the open end of the tube, can be thought (for high values of λ) acting like a piston of zero mass radiating some energy out, and reflecting some back inside the tube: in this view, it is possible to look at the open end as an impedance contrast surface: for $\lambda > 10a$ (where a is the radius of the conduit) the majority of the energy remains trapped inside the tube.

Besides the effect on energy radiation outside the tube, the ratio between wavelength and radius of the conduit controls also the radiation pattern in the free air:

- For $\lambda > 2\pi a$, sound spreads out uniformly in all directions from the tube: if the walls were not present, the piston would act like a monopole. The effect of wall reflection doubles the amplitude with respect to the free monopole condition.
- For $\lambda < 2\pi a$, there will be a lobe of radiation along the tube axis, eventually surrounded by secondary maxima due to diffraction effects.

Figure 2.7 shows the effect of tube radius a at different frequencies.

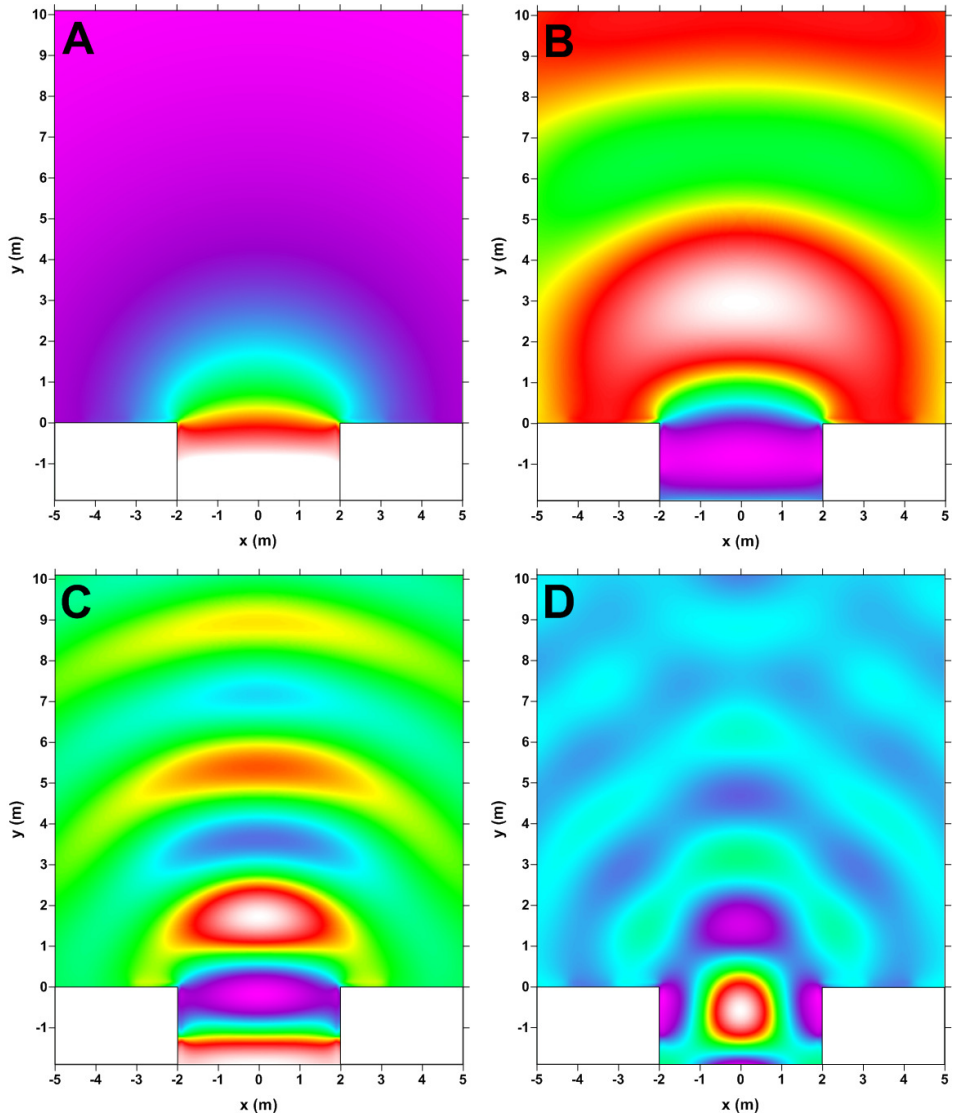

Figure 2.7: Radiation pattern for different frequencies from a duct of radius a=2 m. Source is located at a depth of 20 m inside the tube. A. ν=10 Hz; the most of energy is trapped inside the tube. B. ν=50 Hz; the tube radiates likewise a compact source. C. ν=100 Hz; a radiation lobe is developing along the tube axis. D. ν=130 Hz; secondary lobes develops around the main one.

Chapter 3

A critical data analysis

Although pressure signals could provide a method to extract many eruptive parameters, it is actually difficult to make an accurate quantitative analysis of data. Moreover many authors uses different formulas for the same physical quantities, giving rise to some paradoxes.

In this chapter is presented a critical analysis of formulas commonly used in literature, evaluating their actual applicability and limits. An analysis of the three acoustic compact sources provides more insight to their actual cases of applicability. Before this, the different sources of uncertainty that can affect measurements are showed. Considering the limits of the theory, an accurate data analysis was performed on some pressure signals from two italian volcanoes: Etna and Stromboli.

Results demonstrate the almost impossibility in the most cases to extract some eruptive parameters, like velocity and mass flux, being confident to the source model applied, as long as **this** is the actual unknown.

3.1 Sources of error

Since detection of infrasonic waves is an experimental technique, it will be clearly affected by some sources of errors. Most of these are unfortunately unquantifiable, but for sure they must be considered in doing an accurate analysis, especially if pressure signals are used to extract some other physical quantities.

The common sources of uncertainty that affect pressure values measured by the sensor are:

1. sensor response;
2. wind;
3. temperature;
4. atmospheric attenuation;

5. scattering and reflection;

6. poorly constrained parameters.

All these effects together can affect significantly the signal with the result of a poor accuracy in any physical quantity extracted. The farther the distance from the vent, the higher the effect of all these uncertainty sources will be. So care must be taken during data analysis.

Sensor response

Pressure detector must have a well known response, to be confident in the measured values. Since many physical quantities like energy or acoustic power depends on Δp^2, any fluctuation on pressure perturbation will be critical.

Moreover, it is important to know the transfer function of the instruments, that have to be as flat as possible in the frequency band interesting for the analysis (Ripepe *et al.*, 2004). Accurate calibration is mandatory for a quantitative analysis on pressure signals.

Wind

The main influence on pressure measurements is due to the wind. Moreover the effect of wind is twofold:

- can significantly distort the acoustic wave, creating shadow zones;
- represents a source of noise at the receiver, with amplitude up to 100 Pa that can completely cover the signal.

The effect of wind is almost unremovable, and can affect both the location of vent that the shape and the amplitude of the signal (Garcés *et al.*, 1998; Ripepe *et al.*, 2004).

As the effect of the wind can be significative, it must not be underestimated. In many cases, pressure recorders are located at a distance of many kilometers from the volcanic vent, sometimes in hostile weather conditions (volcanoes can be mountains of thousand meters of altitude), where strong wind can develop.

The wind can significantly affect the acoustic ray path and give rise to shadow zones (Johnson, 2003; Figure 3.1). As this effect is well known, but not quantifiable, maybe it can be better to install a meteorological station nearby the pressure sensor, to perform a real-time monitoring of weather parameters. In this condition, a measurement of wind speed and direction could give an estimation of the perturbation on the signal from the receiver neighborhood, providing an evaluation of the signal-to-noise ratio.

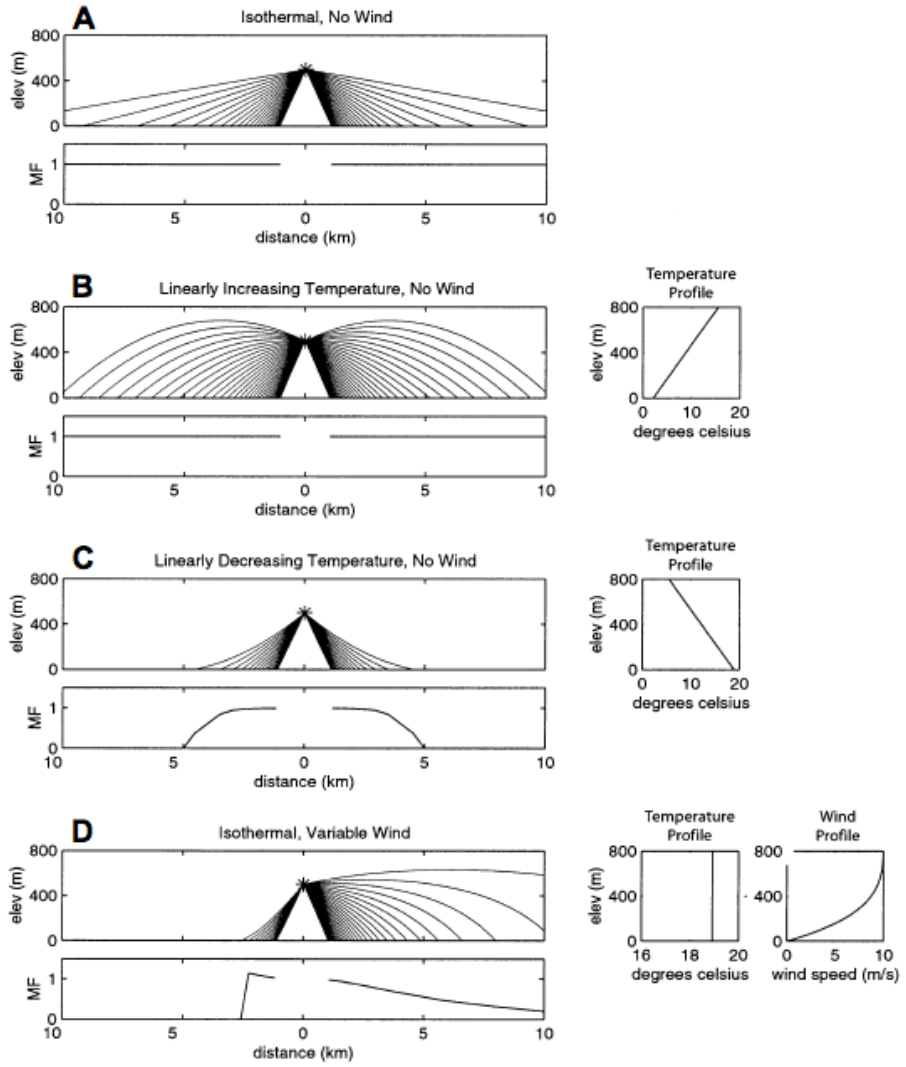

Figure 3.1: Ray path focusing on infrasound under the effect of wind and temperature (Johnson, 2003). A. Homogeneous temperature profile, no wind. B. Temperature inversion, no wind. C. Normal temperature gradient, no wind. D. Isothermal atmosphere and wind increasing with altitude. Acoustic rays are drawn at 1° increments. An absence of ray paths impacting the ground constitutes a shadow zone. Magnification factors (MF) represents a departure from the expected pressure amplitude for an isotropic acoustic source radiating spherically into a homogenous atmosphere, and are shown for each scenario.

Temperature

As shown by equation (2.14) sound speed depends on the atmospheric temperature. Then c will be affected either by any temperature fluctuation or by the temperature gradient with the altitude. In normal conditions the atmosphere is stratified with temperature decreasing with the elevation. But in particular cases, an isothermal or inverted profile can develop connected to many causes. The effect of temperature fluctuations, known as atmospheric refraction, results in the bending of the ray path of the acoustic wave towards regions of low values of c; Figure 3.1 shows both the effect of temperature gradient and wind shear on acoustic wave propagation in atmosphere.

Also humidity has an effect on pressure recordings, inducing a distortion in the transfer function of electret condenser microphones, and can be reduced by an appropriate shielding of the sensor (Ripepe *et al.*, 2004).

Atmospheric attenuation

Since the acoustic wave propagates in a non-ideal atmosphere, together with the amplitude decay with distance $\propto r^{-1}$ associated to the geometrical spreading of the wavefront, pressure perturbation will be attenuated by propagation inefficiencies through the atmosphere. Such an attenuation is due to either viscous friction and thermal conduction losses, or absorption due to the molecular relaxation (both vibrational and rotational) of atmospheric gases, mainly oxygen and nitrogen (Morse and Ingard, 1968). All these effects are associated to the conversion of acoustic energy in heat, with the consequent attenuation of the wave amplitude.

Experimental measurements and theoretical analysis demonstrated that the atmospheric attenuation decays exponentially with the square of frequency of the acoustic wave (Reed, 1972; Sutherland and Bass, 2004), as

$$\Delta p = \Delta p_0 \exp\left(-\frac{\alpha \nu^2}{\rho_0}\right) r, \tag{3.1}$$

where Δp_0 is the initial pressure perturbation, ρ_0 is the air density, ν is the wave frequency, r the distance and α is the attenuation coefficient, dependent upon the atmospheric moisture content (Bass *et al.*, 1972).

However, the attenuation effect for infrasound seems to be significative only in high atmosphere, and can be safely neglected in most cases.

Scattering and reflection

If during the propagation in air the acoustic wave encounters obstacles or topographic barriers, phenomena of scattering, reflection and diffraction will be important.

The effect deriving from the incidence of a wave with an angle θ with respect to the surface normal to a discontinuity plane between two media, results in a splitting of the incident wave in two new waves: the reflected wave in the first medium (with an angle equal to θ from the normal), and the refracted wave in the second medium (with an angle depending on the acoustic properties of the two media, Figure 3.2). If an acoustic wave propagating in air encounters to an *acoustically hard* medium, no transmitted wave will propagate in it and the incident wave will be reflected in air maintaining amplitude and phase.

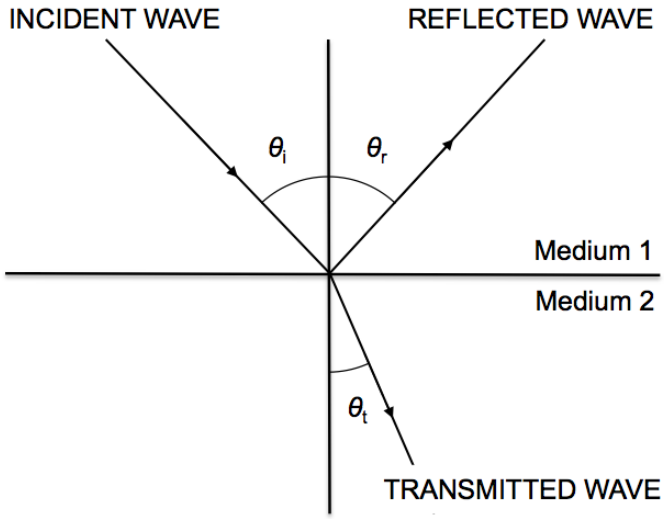

Figure 3.2: Reflected and transmitted waves at a discontinuity surface between two different media.

Otherwise, if the wave encounters an obstacle or a barrier can be blocked, producing any shadow zones. This can be an actual cases for volcanic infrasound, as long as both the source and the receiver usually lies at the ground level, or can not be in line of sight.

When a wave encounters an obstacle, the further propagation depends on frequency and is controlled by diffraction. If the wavelength is bigger than the linear dimension of the obstacle, the wave will undergo no perturbation; instead if the linear dimension of the obstacle is comparable to λ, the effect of diffraction become important and some shadow zones can appear.

In the actual cases of volcanology, signal frequency is usually below 10 Hz, then will be: $\lambda > 34$ m. For such a wavelength, only significant topographic barriers like hills can affect the propagation of the signal. Any roughness of the terrain will not have any effect on the wave. Anyway, since the pressure recorder is locater nearby the ground, effect of reflection can be significative.

Also diffusion due to atmospheric turbulence or clouds (that represents localized density perturbations) is a typical mechanism of energy dissipation for sound waves. But since diffusion is effective at small spatial scales, for the wavelength related to infrasound does not have any contribution.

Poorly constrained parameters

The formulas used to extract any physical quantities about the eruption from pressure signals contain many parameters, and these will introduce further uncertainties on the extracted values. Moreover, the exponent in the dependence from a parameter gives an indication of the degree of uncertainty associated to that parameter. For example, in equation (2.26), distance r and density ρ_0 have a different exponent. Since r appears at the second power, a higher accuracy is required in the measurement of such parameter.

Physical parameters usually connected to pressure perturbation are:

- source-receiver distance, r;
- vent radius, R;
- empirical constants, K;
- magma-gas mixture density, ρ_m.

Any bad constrained quantity between these will affect results in the analysis.

3.2 A critical approach

As showed in Chapter 2, there are three kind of elementary sources in acoustic theory. The possibility to apply these sources on actual cases in volcanology depends on many factors, and the choice is often tricky. Furthermore, the source model often depends on some unknown or bad constrained parameters, and the identification of the source characteristics from data results almost impossible.

The whole process of data analysis and source choice is strictly connected and twofold, because each depends on the other:

1. the choice of a source model permits to extract important dynamical quantities such as velocity and mass flux;
2. data analysis can (or "maybe could") provide a tool to identify the source mechanism on the basis of the most likely results.

The uncertainties connected to both choices are still high, and neither the way 1 nor the 2 are capable to provide results with high accuracy.

Woulff and McGetchin in 1976 performed a quantitative analysis in volcanology to obtain dynamical quantities from acoustic recordings. The authors extracted gas velocity for Acatenango volcano (Guatemala) fumaroles from acoustic power, and proposed the first connection between volcanic eruptions and acoustic sources:

- **Monopole** can be associated to extremely impulsive blast-type eruptions. Since the source intensity is connected to a time varying mass flux (2.24), no monopole radiation will result from a volcanic eruption where the gas velocity is constant.
- **Dipole** can be associated to a stationary flowing gas, interacting with solid boundaries (as the vent wall) or solid particles.
- **Quadrupole** can result from a turbulent hot jet of gas and solid particles.

In volcanology, of course the source can't be a single point but an extended source. Anyway, measuring signals at long distance from the source (typically at $1-10$ km) it can be possible to consider the source as point-like.

The authors calculated velocity starting from the Lighthill's 8^{th} power law (Lighthill, 1952, 1954):

$$\Pi \propto u^8, \tag{3.2}$$

that is valid for subsonic jets. This condition is usually satisfied for volcanic jets, except for the most violent explosions.

Considering an extension to the cases of monopole and dipole sources on the basis of dimensional analysis, Woulff and McGetchin obtained the following formulas:

$$\Pi_M = K_M \frac{\rho_0 A u^4}{c}, \tag{3.3}$$

$$\Pi_D = K_D \frac{\rho_0 A u^6}{c^3}, \tag{3.4}$$

$$\Pi_Q = K_Q \frac{\rho_0 A u^8}{c^5}, \tag{3.5}$$

where the subscripts M, D, and Q refers respectively to the monopole, dipole and quadrupole cases; ρ_0 is the air density, c is the sound speed, A is the vent area, and the term $\rho_0 A u^8/c^5$ in (3.5) is known as the *Lighthill's parameter*.

K_M, K_D, and K_Q, are three *empirically determined proportionally constants*. K_M have to be equal to 1, as will be demonstrated later; anyway, monopole radiation was not considered by Woulff and McGetchin, since the

gas flow from Acatenago fumaroles where almost steady. For K_D and K_Q, the authors provided the following values, on the basis of their experimental results:

- $K_D \approx (10^{-2} \div 10^{-1})$;
- $K_Q \approx (3 \cdot 10^{-5} \div 5 \cdot 10^{-4})$.

Since the velocities connected to a quadrupole source where too high (a value of ~ 10 m s^{-1} was measured by video recordings), the authors deduced that the source had to be a dipole, and extracted the velocity considering a value of $K_D = 1.3 \cdot 10^{-2}$, from the exact solution of the highly-idealized aeolian tones (Leehey and Hanson, 1970).

A crucial point lies inside these empirical constants. Many authors used different value in order to have a better fit for data. Furthermore the range of values associated to constants K together with the uncertainty about the vent area A can prevent the identification of the actual acoustic source. In the following subsections I propose some considerations about the three kind of sources, considering the different approach followed by other authors.

3.2.1 Monopole source

As shown in Chapter 2, monopole source is a spherical expansion related to a rapid injection of mass, like a bursting balloon. Now, let's consider the cases of applicability of this kind of source in volcanology.

Some authors (Vergniolle and Brandeis, 1996; Vergniolle *et al.*, 1996; Johnson, 2003; Vergniolle *et al.*, 2004; Vergniolle and Caplan-Auerbach, 2004; Vergniolle and Caplan-Auerbach, 2006; Johnson *et al.*, 2008) assume that a strombolian explosion can be associated to a simple acoustic source. This can be true considering that we usually look at a strombolian explosion as caused by a sudden decompression and explosion of a gas bubble surrounded by a thin layer of magma (in the order of some centimeters) at the top of a magma column. In this view, it can be better to consider a simple acoustic source radiating only in a half-space. Some authors (Johnson, 2003; Vergniolle *et al.*, 2004), considered that this condition could be more reliable in actual cases. The problem is that a half-sphere radiating in a half-space is not actually a *half monopole*, because of the effect of reflection of the expansion at the borders (Figure 3.3). However, we will see how to deal with this effect further.

The second actual problem connected to the monopole source for a strombolian explosion is the **depth** of the explosion, because in many cases this occurs inside the conduit. As shown in Figure 3.4, strombolian explosions, also in cases of steady eruptive style and persistent activity, as at Stromboli volcano, can have some different shapes (Patrick *et al.*, 2007). This phenomenon, although is related to the rheology of magma and the

gas content, is undoubtedly dependent on the depth of the explosion of the gas bubble. Unfortunately this parameter is in most cases unknown. Moreover, by using a monopole source model, we must consider the expansion and propagation in the free-space, so if we dip the source inside the conduit, this model is no more valid.

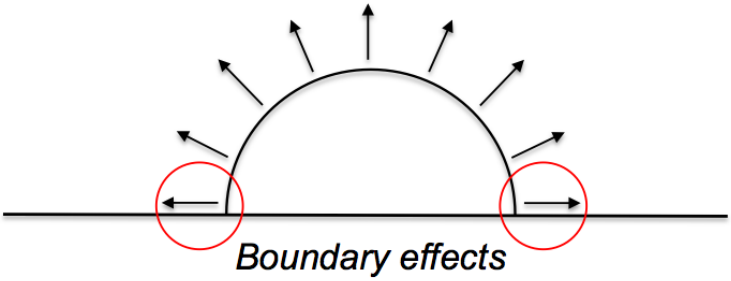

Figure 3.3: Reflection of acoustic waves at the edge of the hemisphere for interaction with the floor prevents the free propagation described by the physics of the monopole.

In this condition, what does become a monopole forced to expand inside a cylindrical geometry (if the conduit geometry can be really though as a cylinder)? Can it behave like a dipole? Maybe something similar, most likely a piston, but there are no formulas to extract directly the pressure perturbation of such a source. Furthermore, the depth of the explosion remains an unknown parameter. It is necessary to investigate this effect with some experiments or numerical simulations. So, care must be taken in data analysis considering a simple source at the base of pressure perturbation generation, because there are two significative problems:

1. the explosion of a hemispherical bubble is **not** a monopole;
2. the depth of the explosion inside the conduit is unknown, and prevent the free-space propagation of the simple source.

A peculiar case for Stromboli volcano considering a simple source will be analyzed in the following.

3.2.2 Dipole source

Dipole is a system composed by two coupled simple sources with the same intensity and opposite sign, in an infinite free-space. As long as the distance between the two simple sources is small compared to the distance at which one calculates pressure perturbation, this quantity will be expressed by equation (2.29). Furthermore, since in volcanology the source-receiver

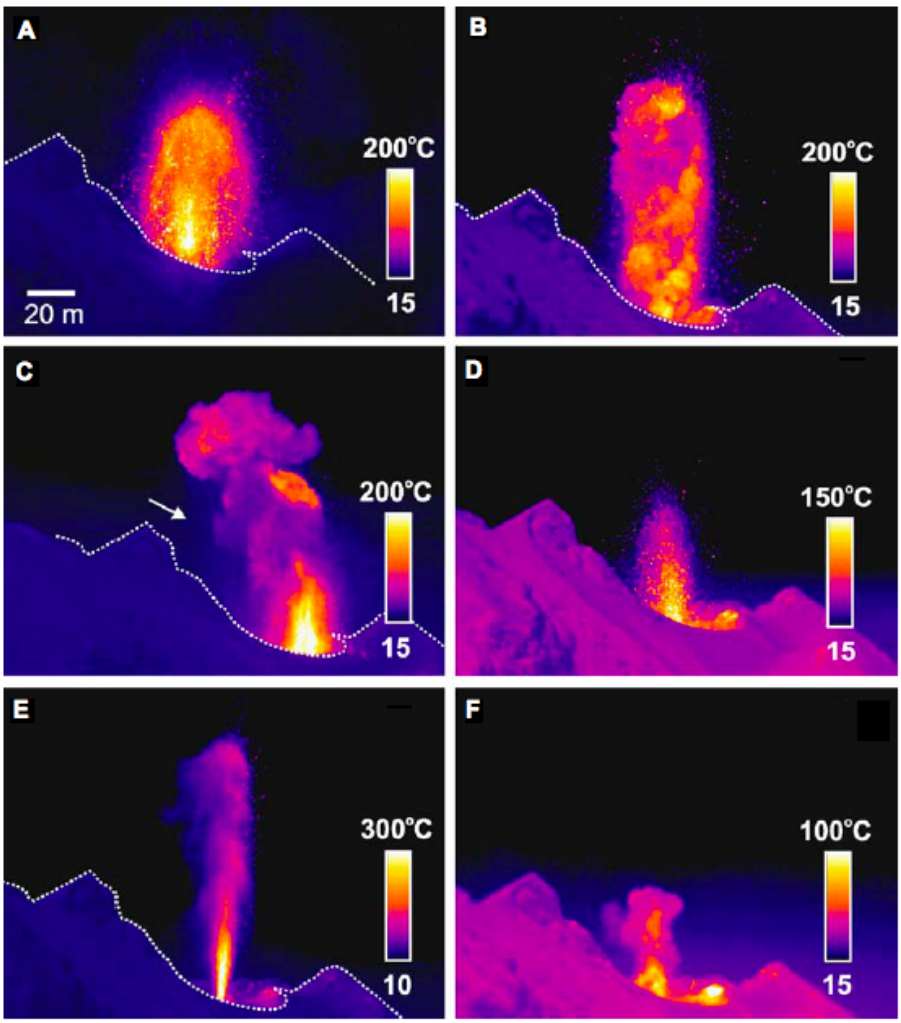

Figure 3.4: The varying styles of eruptions at Stromboli (Patrick *et al.*, 2007). A. Poor collimated Type 1 eruption. B. High-velocity ash plume, Type 2a eruption. C. Low-velocity, particle-laden plume with a high degree of visible sedimentation (arrow), Type 2b eruption. D. Mild Type 1 eruption with moderate collimation. E. Intense Type 1 eruption with excellent collimation. F. Small Type 2b eruption. Type 1 are ballistic-dominated eruption, with little to no visible plume due to the absence of ash-sized particles; Type 2a eruptions involve both ballistic particles and ash plume; Type 2b eruptions contains mainly ash, with few ballistics.

distance is usually in the order of some kilometers, the condition of far field (2.31) can be considered satisfied.

In volcanology the dipole is the most used source in the interpretation of infrasonic signals from different kinds of explosive eruptions. As long as the simple source is related to a sudden explosion with a short duration, dipole can fit better prolonged eruptions. Woulff and McGetchin (1976) considered the dipole source as the product of interaction of a gas flow with the solid boundaries of the conduit wall. Actually this effect is a result of the interaction of a turbulent (therfore quadrupole) gas flow with solid boundaries (Curle, 1955; Meecham, 1967), and consists in a distribution of dipoles. So it is not so immediate the application of the physics of a point-like dipole source. However, there are many applications of dipole sources in volcano acoustics. Woulff and McGetchin (1976) used dipole to analyze some fumaroles; some authors used it in analyzing sub-plinian plumes and thermals (Vergniolle and Caplan-Auerbach, 2006), others for vulcanian explosions (Caplan-Auerbach *et al.*, 2010). Johnson *et al.*, 2008 considered the explosion of gas bubble at the surface of the lava lake of Erebus volcano having the nature of a monopole with dipolar asymmetries connected to the film rupture.

Despite the wide use however, there are some basic problems in the application of this model. The first is the presence of the angle θ. None of the previously quoted authors considered this quantity at all. But it is for sure mandatory if one want to use a compact dipole as actual source, because pressure perturbation will depend both on r and θ also in the far field, as shown by equation (2.29). The omission of θ in the analysis necessarily leads to a paradox.

Let's look at a simple example. If we perform a measurement of the pressure perturbation of an explosion in two different spatial points P_1 and P_2 placed at the same distance r from the source, but with different angles from dipole axis (Figure 3.5), for sure we'll have two signals with different amplitude (the smaller the angle, the higher the amplitude of pressure perturbation). So if we do not consider the angle θ in the interpretation of signals (as in calculating acoustic power to extract the jet velocity), we will get two different values for the same physical quantity and the same event! This is obviously impossible!

The second problem is relative to the length of the dipole. Vergniolle and Caplan-Auerbach (2006) derived from equation (2.33) a formula similar to (3.4) used by Woulff and McGetchin (1976), but containing the dipole length l:

$$\Pi_D = \frac{\rho_0 \pi l^2 u^6}{12 c^3}, \tag{3.6}$$

Using the (3.6) they considered the dipole as long as vent diameter. Such a consideration put some doubts about the actual positioning of the dipole axis by the authors, leading to two possible choices:

1. dipole axis is placed horizontally, lying on the plane of the volcanic vent (Figure 3.6A), and has a length equal to the vent diameter;
2. dipole axis is placed vertically (Figure 3.6B), and the authors used the vent diameter to make an estimation of dipole length.

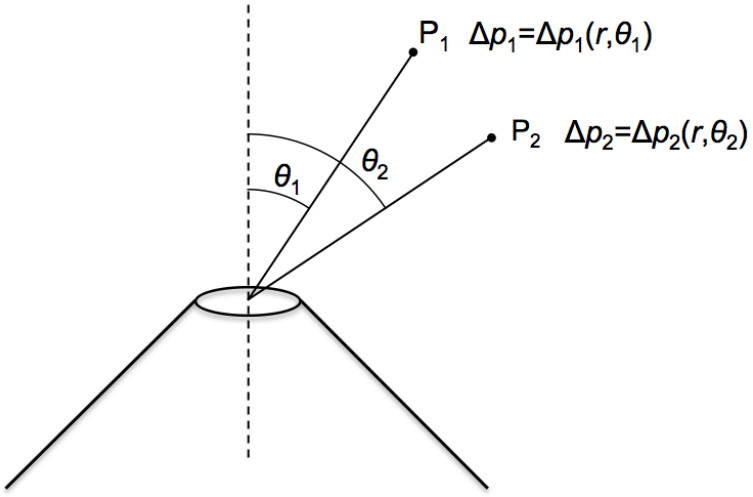

Figure 3.5: Points P_1 and P_2 are at the same distance r from volcanic vent. But, having a different angle θ from it, pressure perturbations Δp_1 and Δp_2 will be different, with $\Delta p_1 > \Delta p_2$.

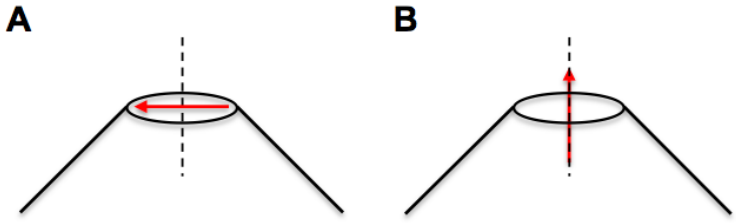

Figure 3.6: Possible orientation of dipole (represented by the red arrow) by Vergniolle and Caplan-Auerbach (2006). A. Dipole lies a the plain parallel to the volcanic vent. B. Dipole is perpendicular to the vent, oriented along the conduit axis.

The first case seems almost impossible for some reasons: if the dipole is horizontal, at some azimuthal angles around the volcano (for $\theta > 90$) there must be a negative first pulse in pressure perturbation. This situation was never reported in literature, and moreover experimentally denied (Ripepe, pers. comm.). Furthermore, since the volcanic conduit is directed vertically, the gas flow must have the same direction, and the dipole axis will do the

same. Therefore the authors probably considered the dipole axis directed vertically, but used the vent radius to estimate the length of the dipole, in absence of any measurements of this quantity. Assuming this assumption valid, anyway, this value do not satisfy the compactness condition (2.30), making the use of an elementary dipole no more valid (Curle, 1955; Lighthill, 1978).

The third main problem connected with this source lies in the actual size and position of the dipole. The physics of the dipole described by equations of Chapter 2 is valid for a source lying in an infinite free space. But, where and how the dipole have to be positioned in the volcano? For sure the dipole axis must be vertical, and coincide with the axis of the volcanic conduit (with the only exception of the case of Johnson *et al.*, 2008, where the dipole term is considered as a random asymmetry in the bubble explosion). So, although we know how to put the dipole in the volcanic vent, we still don't exactly know where. Maybe it can be positioned, as the monopole, at the separation interface vent-air. But, in this case, what will happen to the negative pressure perturbation? For sure this is not a dipole source anymore. Maybe we can put the dipole inside the conduit: but at which depth? In doing this, we fall again out of the cases of applicability of the theory.

So, although dipole source seems to be better than the simple source (because of the different types of eruptions that can fit, and the cylindrical nature of the volcanic conduit), the actual cases of applicability are strongly reduced because of some primary unknowns (angle θ, length of dipole and position of source). Also for dipole source, as for the monopole, it seems to be necessary to perform accurate numerical simulations and experiments suited to study the effect these parameters for volcanological applications:

1. angle θ from the dipole axis;
2. dipole length;
3. source positioning with respect to the volcanic vent.

Only with a clear insight of the behavior of such a source it will be possible to use it for data analysis to confidently extract physical quantities.

3.2.3 Quadrupole source

Since quadrupole radiation is generated by a turbulent flux, it seems natural to connect this kind of acoustic source to the explosive eruptions with a high degree of turbulence. These are typically eruptions with a moderate to high degree of violence like vulcanian, sub-plinian, plinian and phreatomagmatic.

As shown in Chapter 2, the equations describing the physics of a quadrupole are rather complex. So, there is no possibility to apply directly a relationship between pressure perturbation and another physical quantity

like velocity. Furthermore, the length scale of the turbulence is related to the average eddies size, a quantity quite difficult to estimate.

An effective method to associate an acoustic signal from a volcanic eruption to a quadrupole turbulence, can be made by means of a spectral analysis. That can be really useful, because pressure signals in time-domain from violent explosions can be rather complex, with the feature of a long-lasting infrasonic tremor. However, its frequency spectrum can be compared to a jet noise spectrum, which represents the typical signature of a high speed turbulent flow. First investigations on jet noise were performed by Lighthill (1952), whose name is related to the previously quoted eight-power low (3.2).

Experimental results showed that similarity spectra of this kind of noise can assume two different shapes depending on the scale of turbulent structures or instability waves of the jet flow (Tam *et al.*, 1996; Tam, 1998). The functions describing these similarity spectra depend only on the peak frequency. Large scale turbulence similarity spectrum is described by the function F:

$$10\log_{10} F(\mathrm{dB}) = \begin{cases} 2.53895 + 18.4\log_{10}\left(\frac{\nu}{\nu_L}\right); & \frac{\nu}{\nu_L} \leq 0.5 \\ -38.19338\left(\log_{10}\left(\frac{\nu}{\nu_L}\right)\right)^2 & \\ -16.91175\left(\log_{10}\left(\frac{\nu}{\nu_L}\right)\right)^3; & 0.5 \leq \frac{\nu}{\nu_L} \leq 1.0 \\ \left[1.06617 - 45.29940\log_{10}\left(\frac{\nu}{\nu_L}\right)\right. & \\ \left. +21.40972\left(\log\left(\frac{\nu}{\nu_L}\right)\right)^2\right] & \\ \cdot\log\left(\frac{\nu}{\nu_L}\right); & 1.0 \leq \frac{\nu}{\nu_L} \leq 2.5 \\ 5.64174 - 27.7472\log\left(\frac{\nu}{\nu_L}\right); & \frac{\nu}{\nu_L} \geq 2.5 \end{cases} \tag{3.7}$$

where ν_L is the peak frequency.

Fine scale turbulence function G has the form:

$$10\log_{10} G(\mathrm{dB}) = \begin{cases} 9.9 + 14.91126\log_{10}\left(\frac{\nu}{\nu_F}\right); & \frac{\nu}{\nu_F} \leq 0.05 \\ -3.5 + [11.874876 & \\ +2.1202444\log_{10}\left(\frac{20\nu}{3\nu_F}\right) & \\ +7.5211814\left(\log_{10}\left(\frac{20\nu}{3\nu_F}\right)\right)^2\Big] & \\ \cdot\log_{10}\left(\frac{20\nu}{3\nu_F}\right); & 0.05 \leq \frac{\nu}{\nu_F} \leq 0.15 \\ \left[-1.0550362 + 4.9774046\log_{10}\left(\frac{\nu}{\nu_F}\right)\right] & \\ \cdot\left(\log\left(\frac{\nu}{\nu_F}\right)\right)^2; & 0.15 \leq \frac{\nu}{\nu_F} \leq 1.0 \\ -\left[8.1476823 + 3.6523177\log_{10}\left(\frac{\nu}{\nu_F}\right)\right] & \\ \cdot\left(\log\left(\frac{\nu}{\nu_F}\right)\right)^2; & 1.0 \leq \frac{\nu}{\nu_F} \leq 10 \\ -11.8 - \Big[27.2523 + 0.8091863\log\left(\frac{\nu}{\nu_F}\right) & \\ +14.851964\left(\log\left(\frac{\nu}{\nu_F}\right)\right)^2\Big] & \\ \cdot\log\left(\frac{\nu}{\nu_F}\right); & 10 \leq \frac{\nu}{\nu_F} \leq 30 \\ 29.77786- & \\ 38.16739\log\left(\frac{\nu}{\nu_F}\right); & \frac{\nu}{\nu_F} \geq 30 \end{cases} \tag{3.8}$$

where ν_F is the peak frequency. Figure 3.7 depicts the similarity spectra for the two length scale of jet noise.

Some authors (Matoza *et al.*, 2009; Fee *et al.*, 2010), made a comparison between the large scale turbulence similarity spectrum and some frequency spectra from different violent volcanic eruptions, obtaining a pretty good fit. This method results rather simple because does not involve any manipulation of data but a Fourier transform, moreover ensuring no approximations or uncertainties. Although can not provide any extraction of dynamic quantities, this analysis is a simple and powerful method to detect the presence of a quadrupole radiation from the jet noise signature. Since quadrupole source has a poor efficiency in acoustic radiation compared to monopole and dipole, the detection of a jet noise spectrum at long distance from the source can be a proxy to notice the presence of intense turbulence in volcanic eruptions.

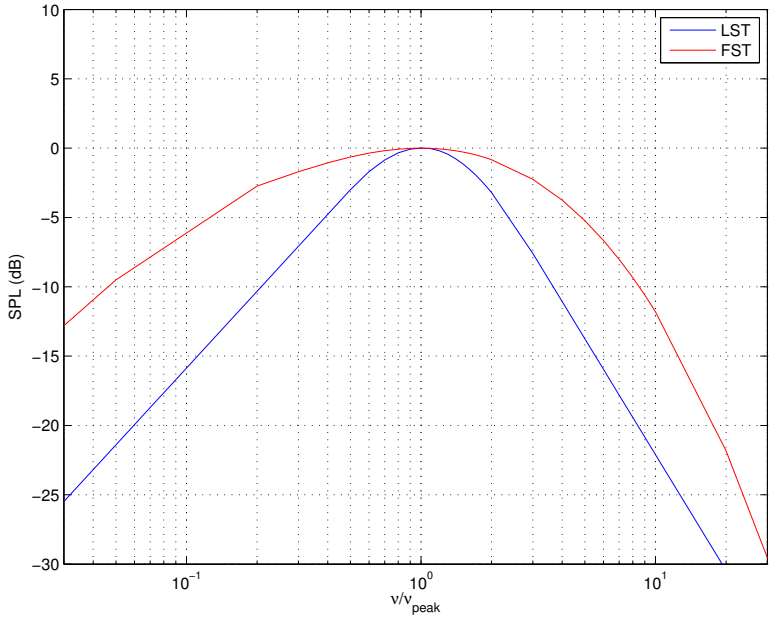

Figure 3.7: Large Scale Turbulence (LST) and Fine Scale Turblence (FST) similarity spectra described by (3.7) and (3.8) (Tam *et al.*, 1996).

3.3 Data analysis

In this section is reported an experimental validation of the methodology of source identification proposed by Woulff and McGetchin (1976) and followed by many authors (Vergniolle *et al.*, 2004; Vergniolle and Caplan-Auerbach, 2006; Caplan-Auerbach *et al.*, 2010). The method consists in using equations (3.3), (3.4) and (3.5) to extract the gas velocity and identify the source process from the most likely value of u for the eruption. Although it has been yet demonstrated in the last section the inefficiency of this methodology on the basis of theoretical considerations, a detailed analysis from experimental data is shown in the following.

3.3.1 Etna

Mount Etna is an active stratovolcano situated in the Sicily island in south of Italy, with an elevation of about 3300 m amsl. Historical volcanism of Etna has been dated back to 1500 BC. At the present there are three main summit craters (Central Crater, NE Crater and SE Crater), but flank eruptions with generation of cones and eruptive fissures are frequent (Giacomelli and Scandone, 2007). The prevalent activity style is effusive, with a low to

medium degree of explosivity. Typical explosive phenomena associated to the presence of gas are strombolian explosions and fire fountains, but ash emissions and vulcanian explosions (due to the interaction of magma with water or snow) sometimes occur.

In the last decade, a multi-parametric real-time monitoring network was installed at Etna volcano by geologists of the University of Florence (Italy). In the night between 23 and 24 november 2007, pressure sensor recorded a long-lasting infrasonic tremor generated by a continuous fire fountaining activity from the SE Crater (Burton and Neri, 2007; Ulivieri *et al.*, 2008). Figure 3.8 shows the infrasonic signal recorded at a distance of 5 km from the active vent where fire fountaining was generated. A 50 Hz sampling rate was used for data acquisition. Signal amplitude is quite low and the shape complicated since represents a seven hours continuous tremor with abrupt pulsation connected to strombolian explosions of large gas bubbles.

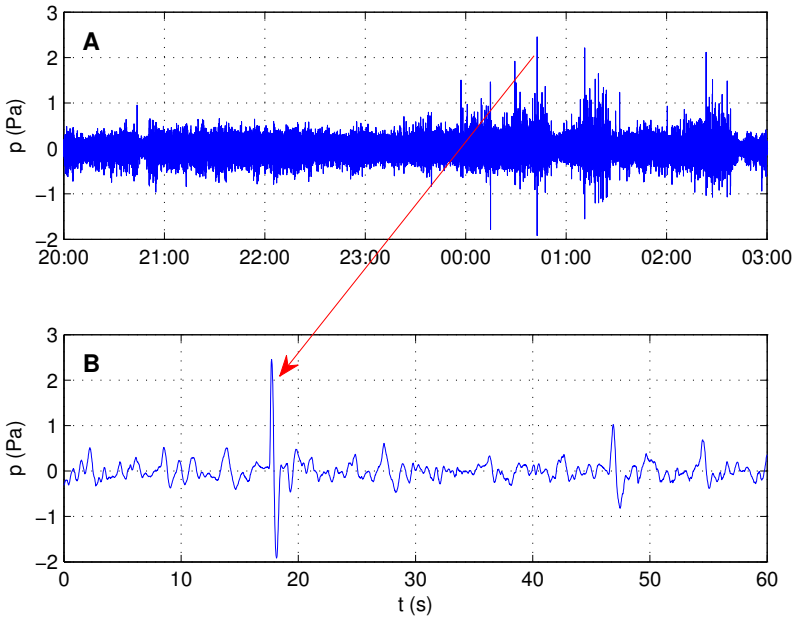

Figure 3.8: A. Seven hours infrasonic tremor generated by the 23-24 november 2007 fire fountain from SE Crater. B. Zoom around the main peak: signal is composed by a superimposition of strombolian explosions on a continuous tremor. A 50 Hz sampling rate for data acquisition was used. Pressure sensor was located at a distance of 5 km from the active vent.

A fire fountain is a peculiar low explosive activity typical of basaltic volcanoes like Etna in Italy and Pu‘u ‘Ō‘ō at Kīlauea (Hawaii). To explain the mechanism that governs the transition between a strombolian explosion

and a fire fountain there are two competing models:

1. gas content and bubble coalescence drive the transition from a bubbly flow (strombolian explosion) to an annular flow (fire fountain) (Jaupart and Vergniolle, 1988; Vergniolle and Jaupart, 1990);

2. magma rise speed controls the eruption style, from strombolian activity (at low rise speed) to fire fountains (at higher rise speed) (Parfitt and Wilson, 1995).

Since the acoustic source connected to the degassing during a fire fountain is unknown, let's follow the approach of Woulff and McGetchin. From the pressure perturbation Δp recorded by the sensor, it is possible to go back to the acoustic power radiated. Considering an infinite free space, the power output obtained from a pressure perturbation Δp measurement will be:

$$\Pi = \frac{4\pi r^2}{\rho_0 c T} \int_0^T \Delta p^2 \mathrm{dt}, \tag{3.9}$$

with r being the distance from the source, ρ_0 the air density, c the sound speed and T the duration of the signal.

Equating the (3.9) to equations (3.3), (3.4) and (3.5) of Woulff and McGetchin it is possible to extract the velocity for the three different acoustic sources. Figure 3.9 shows gas velocity u for the seven hours of fire fountaining obtained calculating the acoustic power in 5 s windows with a 50% of overlapping. A value of 5 s is rather accurate, since it smooths any little departure from a medium value letting clearly identifiable all the instantaneous pulsations in activity. Two values of 10 m and 20 m were considered for vent radius.

Estimates of the height of fire fountain from thermal images let suppose that it was as high as 500 m from the volcanic vent (Andronico and Cristaldi, 2007). This information results rather important since enable the calculation of exit velocity of gas from the vent by using a simple ballistic relationship:

$$\frac{1}{2} m u^2 = mgh, \tag{3.10}$$

from which it can be extracted u:

$$u = \sqrt{2gh}. \tag{3.11}$$

From equation (3.11) it is possible that the exit velocity reached a value of about 100 m s^{-1}. Being aware of this information upon the height of fire fountain, it seems from Figure 3.9 that the most likely source model for the generation of infrasound can be the dipole.

If vent radius is about 10 m, dipole gives a mean value of 70 m s^{-1} for velocity; for a vent radius of 20 m, mean velocity for a dipole is around

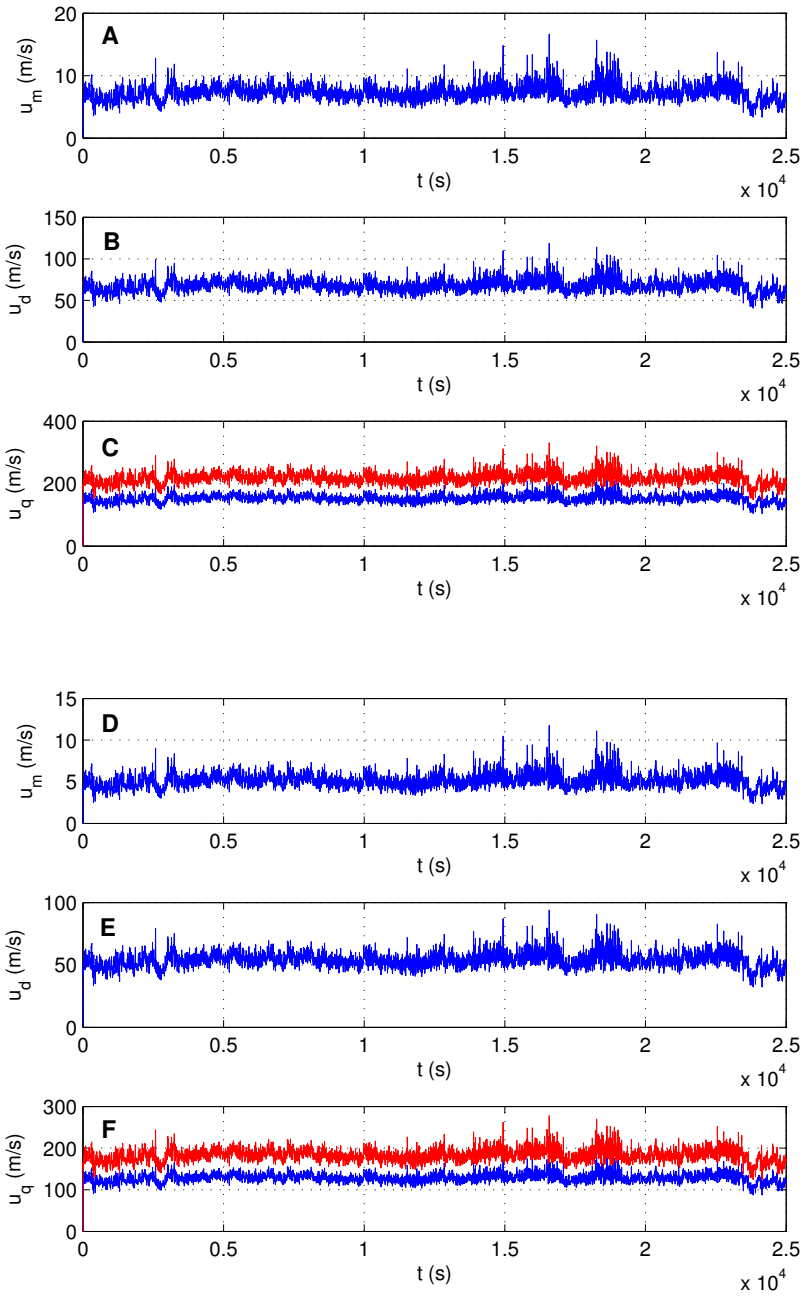

Figure 3.9: Time series of velocity extracted by infrasound using equations (3.3), (3.4) and (3.5). For A, B and C is considered a vent radius $R = 10$ m. For D, E and F is considered a vent radius $R = 20$ m. C and F show two lines, associated to different values of K_Q: $3 \cdot 10^{-5}$ (red) and $5 \cdot 10^{-4}$ (blue).

50 m s^{-1}, with main pulsations reaching the ballistic value of 100 m s^{-1}. Monopole model gives values of velocity too low, and is discarded. Furthermore, a "continuous" monopole seems almost unreal.

Figure 3.9 shows another interesting remark: if we suppose a quadrupole source for the eruption, the wide range of variability for the coefficient K_Q makes any estimation of velocity almost impossible for the huge range of likely results. However, for a vent radius of 20 m quadrupole gives a mean velocity of about 120 m s^{-1}, that is not so far from the ballistic value. Actually, if the radius was larger than 20 m, by this methodology quadrupole model could fit data as the dipole for a vent radius of 10 m.

Another method to detect the presence of turbulence as a source for the infrasound consists in the comparison between the frequency spectra of the signal and the similarity spectra of jet noise (Matoza *et al.*, 2009).

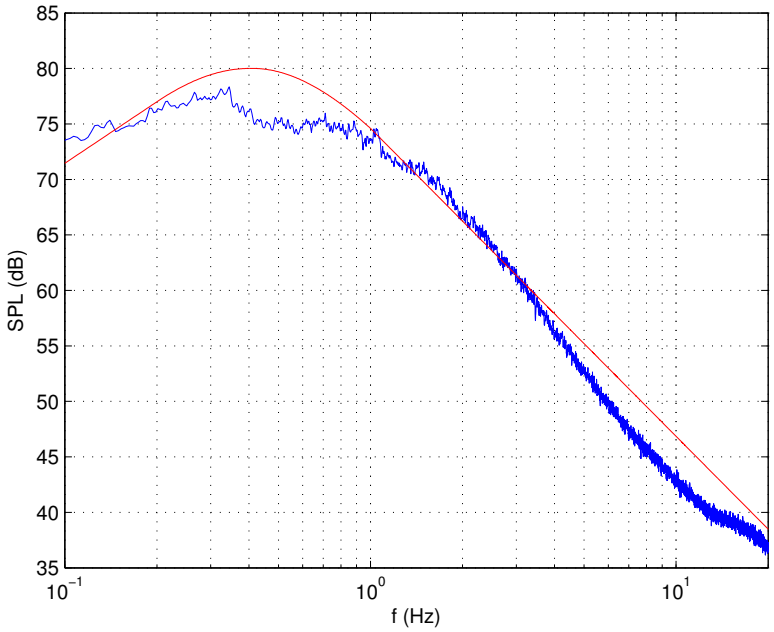

Figure 3.10: Comparison between the frequency spectrum of the pressure signal from fire fountain (blue) and the Large Scale Turbulence similarity spectrum (red).

Figure 3.10 shows that the large scale turbulence similarity spectrum almost fits the spectrum of the eruption. Although there is a pretty good overlapping between the curves, this seems to be not significative at all frequencies. Therefore we can conclude that the turbulence in the fire fountain, although present is not enough efficient to play a significant role in the generation of infrasound.

Although a confident measurement of gas velocity results quite compli-

cated, in this case the method could permits to identify the most probable acoustic source as a possible combination between dipole and quadrupole because supported by other experimental evidences:

1. the long-duration activity rejects the monopole model;
2. the height of the fountain can provide a range of reasonable values for u that helps in the "choice" of the source model.

However, because of the lack of information about the vent radius, whose value has a significant effect upon the calculation of velocity, it is not possible to discriminate accurately between dipole and quadrupole. Moreover, during a long-lasting and intense eruption, it is possible that the vent radius can change because of the building of a scoria cone.

Furthermore, still remains the lack of information about the angle from the dipole axis, a mandatory information as we said in the previous section. Then the realistic values provided by the monopole are be affected by the presence of the unknown parameter θ: how can we be confident about a measurement like that?

3.3.2 Stromboli

Stromboli island is a stratovolcano in the south of Italy with an elevation of 924 m amsl. Since the volcanic structure develops underwater, the island represents less than a half of the entire edifice. Volcanic activity started thousands years ago, and the typical style is the bursting of a gas bubble at the top of the magma column with the ejection of pyroclasts from the magma film surrounding the bubble (Vergniolle and Brandeis, 1996; Scandone and Giacomelli, 1998), the so called *strombolian explosion*.

Thanks to its non-stop activity Stromboli is one of the most studied and monitored volcano in the world. In the last years geologists of the University of Florence developed and installed on the flank of Stromboli an experimental geophysics laboratory, for a real-time monitoring and analysis of many physical parameters useful to improve the scientific research in volcanology, and important for evaluating the volcanic risk connected to population safety. Figure 3.11 shows the complex monitoring system installed at Stromboli by Ripepe *et al.* (2009b).

To evaluate the approach of Woulff and McGetchin, a peculiar *major explosion* of Stromboli volcano was analyzed. The persistent "ordinary" activity of Stromboli is sometimes interrupted by more energetic events called *major explosions*. That kind of activity can eject scoria and bombs to 150 m of height above the eruptive vents, and occurs at Stromboli a few times in a year. In some years, occurs even larger explosions called *Paroxisms*, with many long-to-medium time precursory phenomena. These events are usually associated to lava extrusions lasting some months and intense explosions with the development of some kilometers high eruptive columns. The

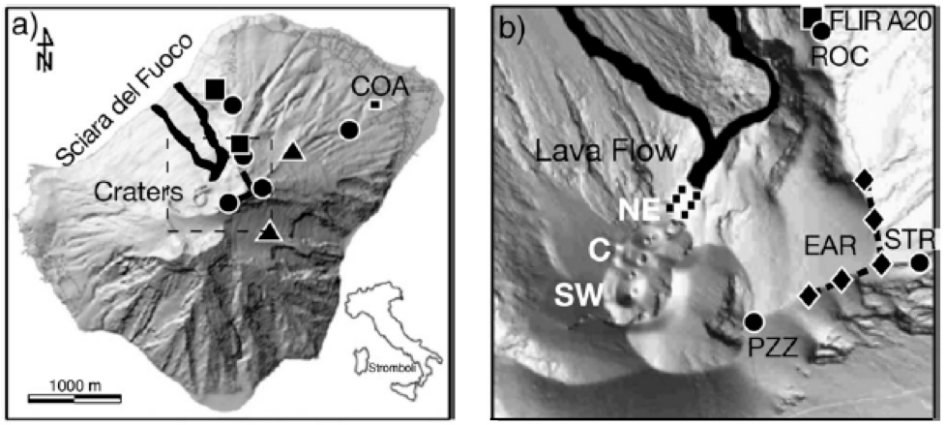

Figure 3.11: Multi-parametric monitoring system installed at Stromboly by geologists of University of Florence (Ripepe *et al.*, 2009b). Circles represent seismo-acoustic stations; diamonds represent the L-shaped infrasonic array; triangles represent tiltmeters; squares represent thermal cameras.

presence of two distinct magma it has been observed in paroxismal events (Landi *et al.*, 2009).

In using the monopole model, it is important to study an explosion as shallower as possible, in order to eliminate the effect of propagation in the volcanic conduit. Stromboli major explosion of 24 november 2009 seems to be a good candidate for the analysis. The event consisted a succession of two main explosions separated by 13 s, causing bombs fallout in the summit area and lapilli dispersal on the lower slopes of the volcano. A red-colored eruption column rose up almost vertically for more than 300 m (Andronico and Pistolesi, 2010). The EAR infrasonic array of University of Florence (800 m amsl, Figure 3.11) located the acoustic source at the Central crater.

In Figure 3.12 is shown the eruptive sequence observed by the thermal camera at the station ROC, at distance of 450 m from active vents. The explosions seems to be rather shallow, mostly the second stronger explosion B. As it can be seen from the thermal image, the second explosion shows a firework-like feature, with sustained magma jets radially dispersed in all directions, followed by a long-lasting vertical jet of hot material.

Figure 3.13 shows the infrasonic signals associated to the event measured at the stations ROC and SCI at a respective distance of 450 m and 1 km from active vents.

Signals demonstrate the almost instantaneous generation of pressure perturbation (first pulse have a duration of less than 1 s for a complete positive and negative oscillation) with the most intense event having a shorter duration of the first. Figure 3.13 shows another remarkable feature: compared to the pressure pulse B, the subsequent jet of gas lasting many seconds results

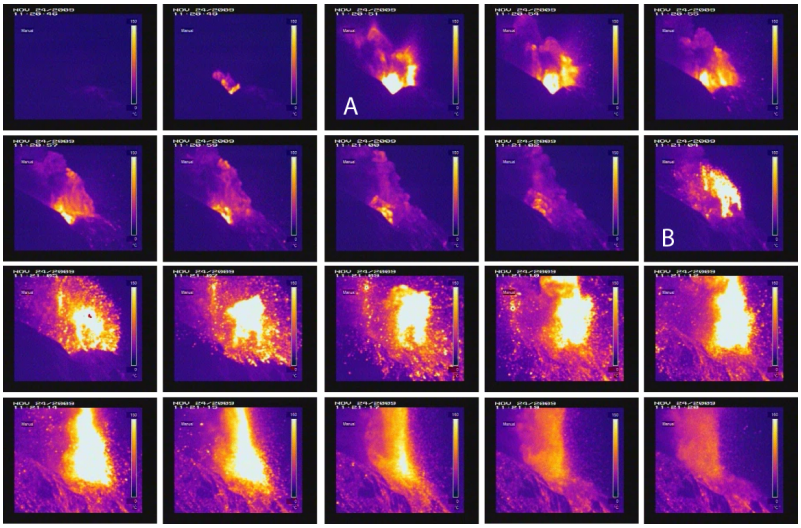

Figure 3.12: Plume evolution of the 24 november 2009 major explosion recorded by the FLIR thermal infrared camera installed at station ROC, at 450 m from the active vents. A and B represents the two explosive events. Sampling rate was 4 Hz. FOV (Field Of View) of thermal camera is about 200 m.

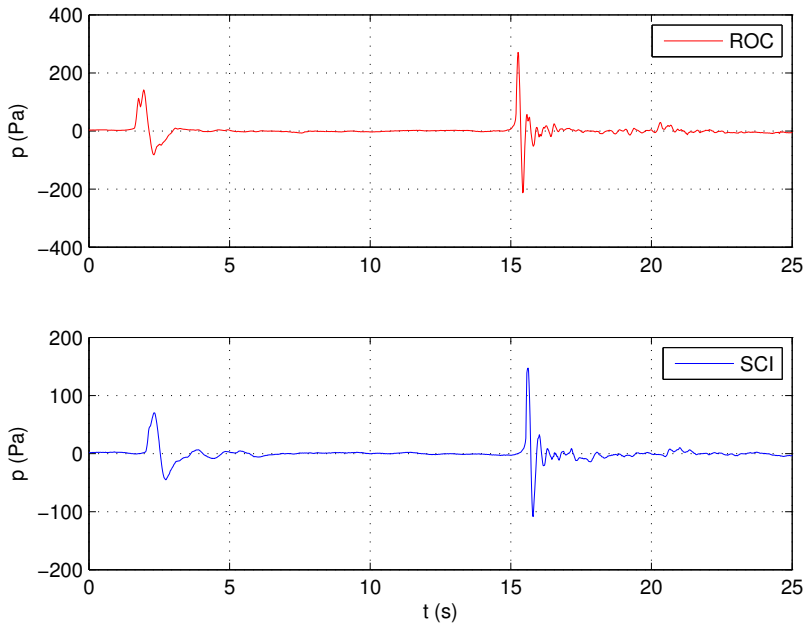

Figure 3.13: Pressure signals from the major explosion of 24 november 2009, recorded at station ROC (red) and SCI (blue), respectively at a distance of 450 m and 1 km from active vents. Sampling rate for data acquisition was 50 Hz.

almost noiseless. This aspect promotes the model of generation of infrasound from the sudden bursting of a gas bubble (Ripepe *et al.*, 1996). In

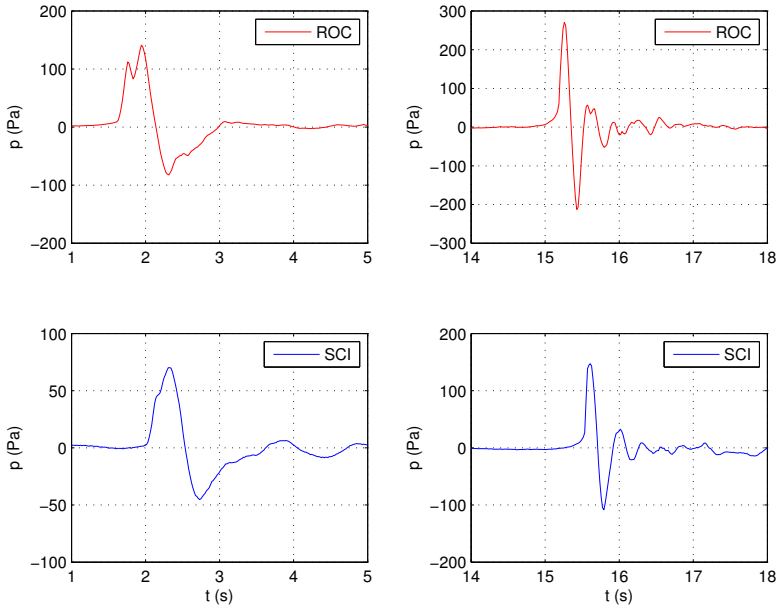

Figure 3.14: Detailed image of the signals shown in Figure 3.13. Signals on the left side represent pulse A, the ones at the right represent pulse B. Both signals recorded at ROC (red) and SCI (blue) stations show that pulse A is the result of a superimposition between two peaks.

Figure 3.14 is visible another interesting feature: Andronico and Pistolesi (2010) pointed out that the first explosion (A of Figure 3.12) consisted of two simultaneous bursts ejecting products in opposite direction towards Pizzo and outside the crater terrace. This remark seems to be in agreement with the pressure recordings: first positive pulse seems to be composed by the superimposition of two peaks, mostly and the station ROC, nearer to the vent. This information will be useful in the interpretation of results.

Now let's follow the approach of Vergniolle and Caplan-Auerbach (2006) for a monopole source, putting some insight into the limitations of the model.

Pressure perturbation for a monopole source is described by equation (2.24). As we want to extract the velocity, let's make appear this quantity in the equations. To accurately use the equations governing the physics of monopole, I will consider its definition as a sphere expanding in an infinite free space. Many authors consider for volcanological applications a half sphere, but as we have seen, this is not an actual monopole. However,

if care is taken in writing the correct equations, the relationship between acoustic power and gas velocity for an actual monopole will be the same of that for a "half monopole" expanding in an infinite 2π semi-space.

Assuming a harmonic source oscillating with pulsation ω, the source term $\dot{q}$ becomes (Morse and Ingard, 1968):

$$\dot{q} \approx \omega q. \tag{3.12}$$

Now, considering a spherical surface expanding radially, the expansion velocity u comes out:

$$q = \dot{m} = \rho \dot{V} = \rho_0 4\pi R^2 u, \tag{3.13}$$

where ρ_0 is the air density and R is the vent radius.

Putting the (3.12) and (3.13) in equation (2.26), the power output for a monopole becomes:

$$\Pi = \frac{4\pi\rho_0\omega^2 R^4 u^2}{c}. \tag{3.14}$$

In the following, we make the assumption that the velocity u of the oscillating body is **small** compared to the speed of sound, and we can make the approximation:

$$u \approx a\omega, \tag{3.15}$$

with a being the amplitude of oscillation (Landau and Lifshitz, 1987).

Taking the amplitude of oscillation equal to the vent radius R, the constraint $u \ll c$ becomes

$$R \ll \frac{c}{\omega} = \frac{\lambda}{2\pi}, \tag{3.16}$$

that is exactly the compactness condition (2.30).

Inserting the (3.15) in the expression of acoustic power (3.14), the pulsation ω disappears, obtaining:

$$\Pi = \frac{4\pi\rho_0 R^2 u^4}{c}. \tag{3.17}$$

This formula is exactly the (3.3) proposed by Woulff and McGetchin (1976), and it is now clear that the value of K_M in (3.3) have to be equal to 1.

Now, putting the (3.17) equal to the acoustic power extracted from pressure signal (3.9), gas velocity for a monopole source can be expressed as:

$$u = \left(\frac{r^2}{\rho_0^2 R^2 T} \int_0^T \Delta p^2 \mathrm{dt} \right)^{0.25}. \tag{3.18}$$

By using the (3.18), gas velocity from a monopole source was calculated for pressure signals recorded at stations SCI and ROC. A value of 2 m was considered for the vent radius R. Time windows of 0.6 s with 50% of overlapping proved to be good to identify velocity peaks in both signals. Figure 3.15 shows the time series of velocity for the eruption.

A comparison between velocity calculated from infrasound and by thermal images was performed tracking plume height from the thermal infrared camera recording (Delle Donne *et al.*, 2006). Figure 3.16 shows the comparison between velocities time series obtained from the two methods. Pressure station ROC and Forward Looking Infrared Radiometer (FLIR) thermal infrared camera were located in the same place.

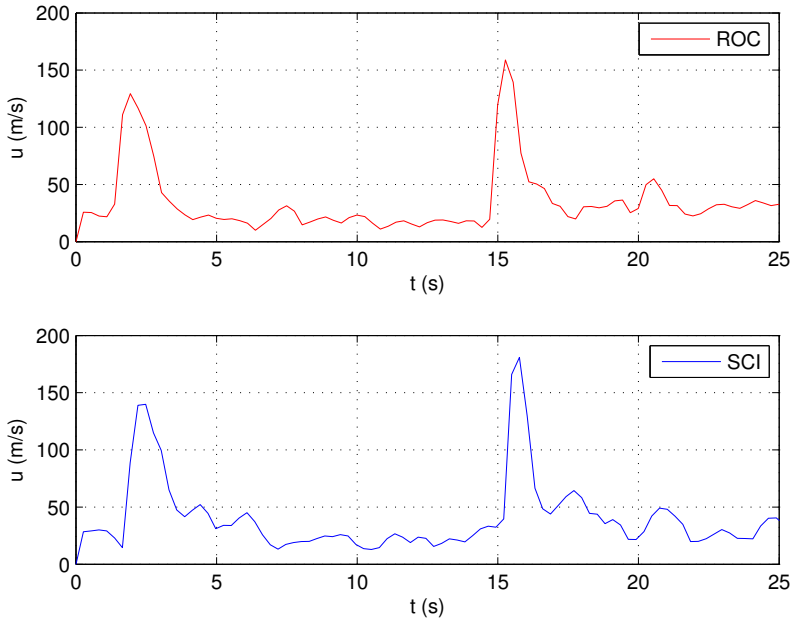

Figure 3.15: Velocity time series for 24 november 2009 major explosion of Stromboli. u is calculated by equation (3.18). There is a good agreement between results from the stations ROC and SCI.

For the second pulse, the agreement between the two methodologies is pretty high. Conversely, for the first peak the velocity measured by thermal camera is considerably lower than the value extracted from infrasound. Furthermore, there is not a well developed velocity peak from the thermal recording. This mismatch can be addressed to the fact that this explosion consisted of two simultaneous bursts. So this effect can have its influence both to the thermal recording and the infrasonic signal. As the dual explosion ejected products in opposite directions, it means that the jet were not vertical. Since the plume tracking method from thermal images is valid for vertical jets, an underestimation from this method is reasonable.

Conversely, for the infrasonic signal the summation of two peaks can result in a increase in the pressure recorded, producing a consequent overestimation of jet velocity. Furthermore, the assumption of monopole can be

no more valid, so gas velocity connected to the first explosion probably has a intermediate value between those measured by the two methodologies.

However, the good matching between the methodologies for the second explosion allows the actual applicability of monopole model, but only because the eruption had some peculiarities occurring at the same time:

1. probably due to the previous explosion magma was shallow, and no propagation of the acoustic wave inside volcanic conduit occurred;

2. thanks to the radial bursting (well demonstrated by thermal video) the use of a model based on spherical symmetry was enabled.

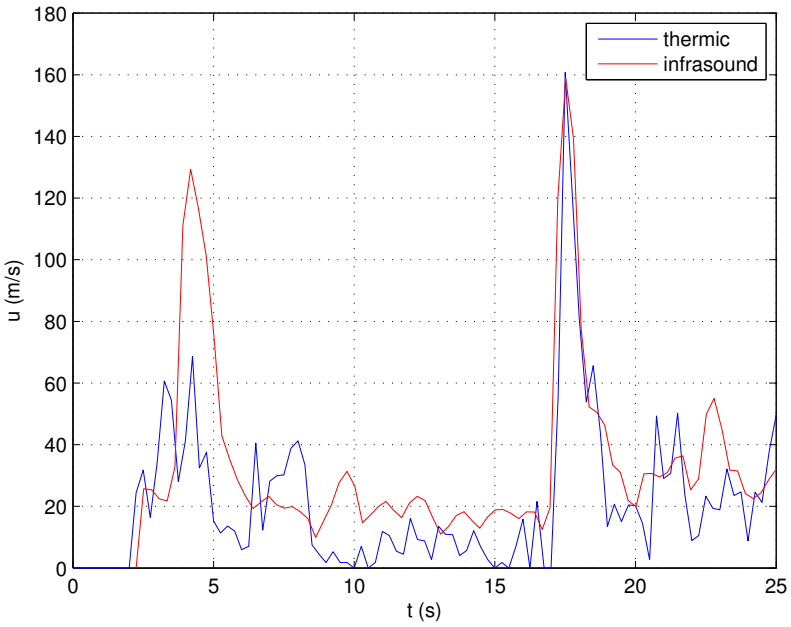

Figure 3.16: Comparison between velocity obtained from infrasonic and thermal recordings. Pulse B shows a pretty high agreement between the methodologies. Pulse A does not give an impulsive velocity peak for the thermal recording.

To test the accuracy of the monopole model at the base of a velocity estimation as described by the (3.18), a comparison with the methodologies proposed by other authors was performed.

Some authors (Vergniolle and Caplan-Auerbach, 2004; Vergniolle *et al.*, 2004; Vergniolle and Caplan-Auerbach, 2006) used the same procedure showed above to obtain the (3.18), but some differences:

1. the acoustic power associated to an acoustic wave was calculated as:

$$\Pi = \frac{\pi r^2}{\rho_0 c T} \int_0^T \Delta p^2 \mathrm{dt}, \tag{3.19}$$

   that is the same of (3.9) but without the coefficient 4 in the geometrical spreading;

2. the coefficient K_M is considered equal to 1/16, for a monopole source radiating from a *circular flat orifice*;

3. the power output for a dipole source was calculated as:

$$\Pi = \frac{\pi \rho_0 l^2 u^6}{12 c^3} = K_D \frac{\rho_0 A u^6}{c^3}, \tag{3.20}$$

   that is the same of Woulff and McGetchin (1976), but with $K_D = 1/3$, having estimated the dipole length l from the vent radius R: $l = 2R$. No consideration about the angle θ from the dipole axis were made.

Figure 3.17 shows a comparison between the time series of velocity extracted from the pressure signals recorded at the stations SCI and ROC considering three different models:

1. red lines represent the monopole model described by (3.18), for both the signals ROC and SCI;

2. blue line represents the monopole of Vergniolle and Caplan-Auerbach (2004) described by (3.19) and (3.3) with $K_M = 1/16$;

3. dashed blue line represents the dipole model of Vergniolle and Caplan-Auerbach (2006) described by (3.19) and (3.20).

Figure 3.17 highlight two interesting features:

1. models proposed by other authors produce high values of velocity, that can not agree with the assumption (3.15);

2. monopole model of Vergniolle and Caplan-Auerbach (2004) and dipole model of Vergniolle and Caplan-Auerbach (2006) are almost indistinguishable for this eruption, since both gives similar values of velocity.

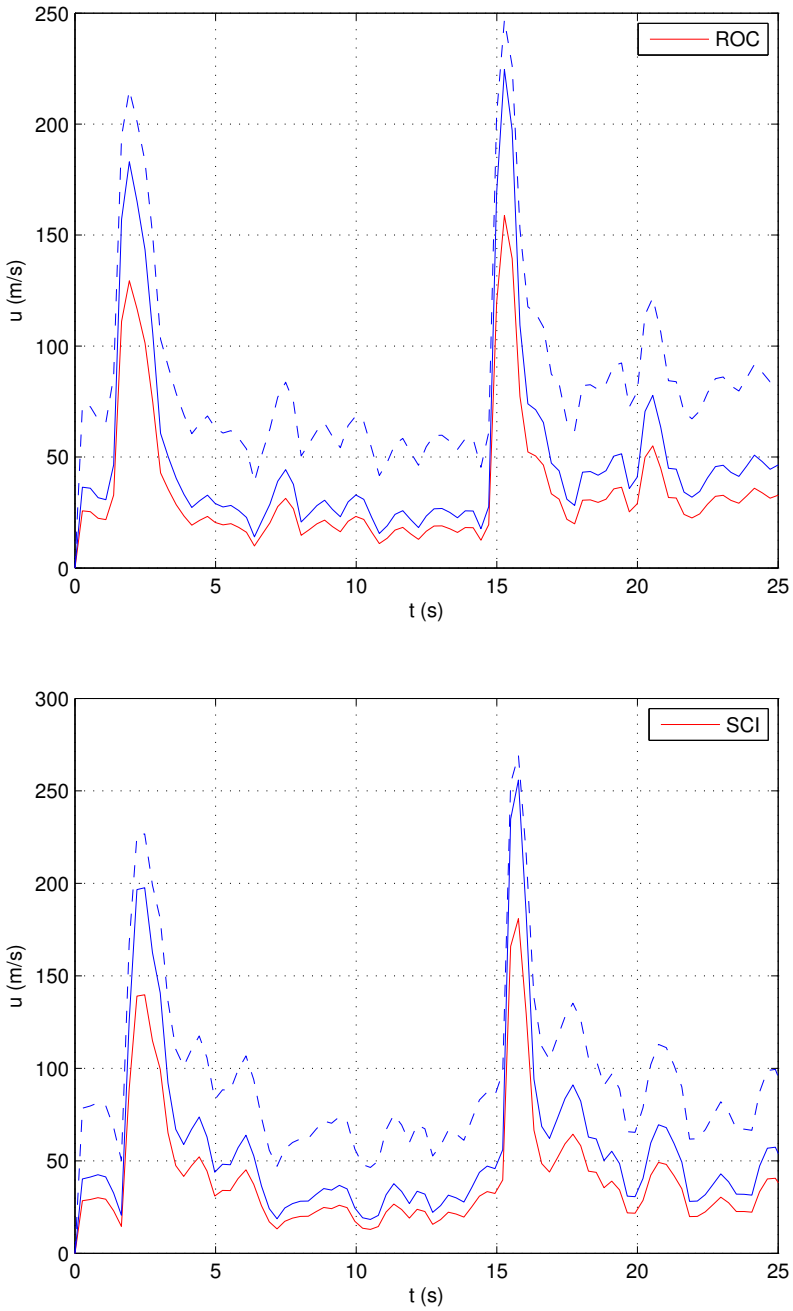

Figure 3.17: Comparison of velocity obtained by equation (3.18) (red) with the velocity monopole model of Vergniolle and Caplan-Auerbach, 2004 (blue) and dipole model Vergniolle and Caplan-Auerbach, 2006 (dashed blue).

Conclusive remarks

As a conclusion, although too simple for the most of cases, monopole seems to be the most applicable acoustic source to model a strombolian explosion, since the equation are rather simple, and it is possible to use the exact acoustic relationship between physical quantities. Furthermore, monopole does not require any information about quantities difficult to obtain, like angle θ from the dipole axis and dipole length l.

Moreover, performing a measurement of the pressure perturbation Δp at large distance from the volcanic vent (many kilometers, as usual), the spherical wavefronts will be almost plane, and both dipole and quadrupole radiation pattern will approximate to a monopole.

To accurately investigate the problem it seems to be necessary the use of numerical simulations. Clearly, it is almost impossible to study the whole phenomenon since it include non linear acoustics, thermodynamics of multiphase fluids, and a lot of unknown. Unfortunately, still there is also the impossibility to have many data for a single event, like in seismology, and an effective inversion problem it is not applicable.

Some experiments (like that proposed in the last chapter), or improved monitoring on actual volcanoes can provide more insight in the physics of the process, and significantly help in the interpretation of data.

Chapter 4

Source characterization by integral methods

As demonstrated in the previous chapter, the measurement of dynamic quantities related to the volcanic explosion from the analysis of infrasonic signals seems to be ineffective. In this chapter, a new methodology to put some insight on the acoustic source in volcanic explosions is proposed.

By means of a combined use of experimental data and numerical simulations, an inverse problem has been set up. Using an integral method to study the effect of volcano geometry on infrasonic wave propagation, pressure recorded at the microphone has been related to source conditions at volcanic vent by a *transfer matrix*. In such a way, the acoustic source has been conditioned to the base of experimental data.

The approximations made for the analysis allowed to solve analytically the equations relating the pressure at microphone to source conditions. This advantage permitted us to test a more complex methodology based on a bi-objective optimization. The comparison of results from the two methods made us confident about the optimization, that will be necessary for future improvements where no analytical solution is admitted.

In the first section are illustrated the limits of validity of the model and the approximations made. The interpretation of results will be made taking into account all these approximations.

In the following sections are described the numerical code used for simulations, the inversion problem set-up and the two methods applied to solve it: analytical solution and optimization.

4.1 Approximations and limits

The generation of infrasonic waves during a volcanic explosion is a complex phenomenon, involving many physical processes. The bursting of a gas bubble surrounded by a thin magma layer is an extremely impulsive

event, governed by thermo-fluid dynamics of a two-phase flow: a pressurized volcanic gas mixture and magma at a certain degree of fragmentation (Blackburn *et al.*, 1976).

Connected to the whole phenomenon, the actual process of generation of acoustic waves is still unknown, and is probably far from the limits of validity of linear acoustics, at least in the vicinity of the volcanic vent. Nevertheless, during the propagation inside the volcanic conduit there can be a transition zone towards the conditions that permits the use of linear equations.

We considered this assumption, that works similarly to the *Kirchhoff's approach* (Farassat and Myers, 1988; Özyörük and Long, 1994). We placed the acoustic source at a certain depth inside the volcanic conduit: above this surface, the linear acoustic theory is adopted (Figure 4.1). Any information about the process beneath this depth remain unknown, because exceed the limits of validity of our model.

This section illustrates the approximations made and the physical processes that are not considered in our model. The interpretation of results clearly depends on these approximations.

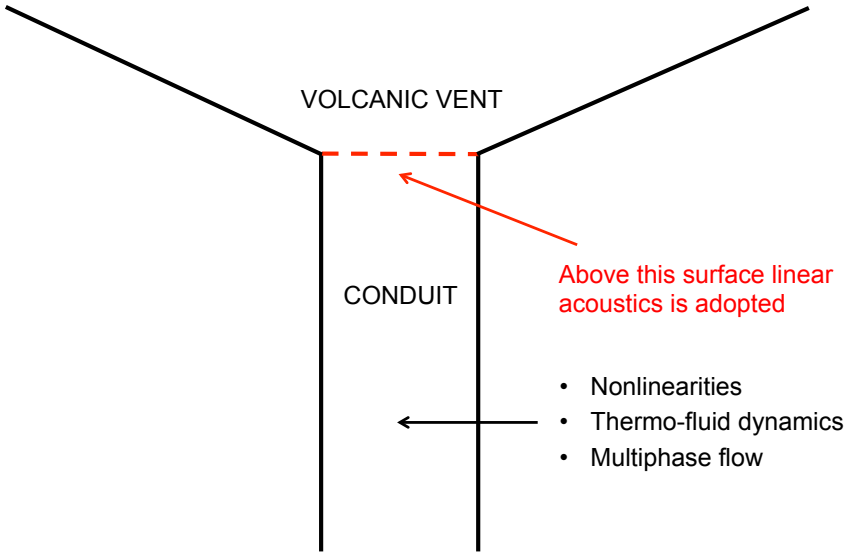

Figure 4.1: Control surface above which linear acoustic theory is adopted. Any information about acoustic propagation beneath this depth are unknown, because governed by a more complex physics.

Nonlinearities and viscosity

In Chapter 2 are illustrated the linearized equations governing the propagation of acoustic waves. The time varying pressure perturbation p is assumed to be small with respect to the ambient pressure p_0, with zero time average. On the basis of this assumption, these quantities appear in equations only at the first power: the linearization consists in neglecting all the higher power, and products such as $\mathbf{u} \cdot \nabla \mathbf{u}$.

The linearized equations of acoustics are valid in most cases for infrasound emitted by volcanic explosions. But at the very onset of the process these approximations could be no more valid, and the sound pressure and corresponding fluid velocity amplitudes can be large enough to be significant; neglecting these terms in the equations can be a source of error (Ingard, 2008).

Performing a linearization of the equations, also the effects of viscosity and heat conduction are neglected, because can be regarded as small perturbations on the overall motion. However, viscosity can be as important as the nonlinear effects, since the magnitude of these terms in the equations of motion can be the same under appropriate conditions (Morse and Ingard, 1968).

The extremely impulsive pressure release and the high velocities associated to a strombolian explosion inside a volcanic conduit can make the effect of nonlinear terms, heat conduction and viscous friction significative, and the acoustic propagation governed by a more complex equation of motion.

If the acoustic source moves during the process of sound generation, the entire physical process lies out of the domain of linear acoustics. This can reasonably occur during volcanic explosions, where the gas-magma mixture moves inside a conduit before escaping in the free air. Furthermore, the acoustic source can be the flow itself, interacting with the solid wall of the volcanic conduit.

In such conditions the equations of generation and propagation of infrasonic waves have to be modified in order to contain the *Mach number* $M = u/c$, representing the ratio between flow velocity and sound speed. Moreover there will be different regimes of flow (subsonic, $u < c$, transonic, $u \approx c$, and supersonic, $u > c$), in which the equations change their form.

The velocities associated to a volcanic explosion could be supersonic in extremely violent eruptions (Donn and Balachandran, 1981; Tahira *et al.*, 1996), with the generation of *shock waves*. Although a strombolian eruption represent the lower-energy explosive volcanic activity, during the onset of the explosions impulsive high velocities inside a duct can affect the acoustic wave generation.

Thermodynamics

Since the pressure perturbation is generated by a high pressure and temperature gas, any effect connected to thermodynamics could affect the wave generation. In connection to this, the compressibility of air can play a role in the process (Ingard, 2008). Moreover, the air can be far away from the standard conditions of temperature and pressure, and the same can occur to the sound speed c.

In connection with the moving source described above, fluctuation of pressure, temperature, velocity and density coupled together recall the use of aerodynamics to accurately describe the flow generating acoustic noise during a volcanic explosion (Pelanti, 2005).

Multiphase flow

Together with high values of pressure and temperature, the thermodynamics of the eruption is governed by a mixture of magma and volcanic gases (mainly H_2O and CO_2).

Gas fraction in a magmatic fluid plays a significant role in the dynamics, and governs the *thrust* phase during the development of a volcanic plume (Wilson, 1980). Moreover the gas bubble dimension and evolution can drive changes in the eruptive style of a volcano (Vergniolle and Jaupart, 1986).

The pressure release and magma fragmentation are strictly related to the exsolution of volcanic gases (Wilson *et al.*, 1980). If the generation of infrasonic wave field occurs inside the magmatic column (Buckingham and Garcés, 1996; Garcés, 1997; Garcés and McNutt, 1997), the magma-air interface acts like an acoustic impedance contrast, modifying the infrasonic signal before it has reached the top of the conduit (where another impedance contrast will be encountered at the free-air level). Furthermore, the value of sound speed c depends on the magmatic fluid properties. Then, the complex features of the magmatic fluid can have an influence both the entire process of generation and propagation of acoustic waves.

Geometry

The geometry of the magmatic conduit and the volcanic edifice have a significative effect on the infrasonic wave propagation. In this work has been studied Stromboli volcano, but the geometry used does not exactly resembles its actual topography. As illustrated in Chapter 2, the wavelengths associated to volcanic infrasound are not affected by any roughness of the terrain. But the overall geometry can alter the results obtained. A refinement of our methodology by the introduction of the actual topography of Stromboli will be topic for future work.

The conduit geometry represents a more complex problem. Even if a volcanic conduit is usually depicted as a cylinder, the actual shape is still

unknown. Furthermore, the depth of the explosion (and then the depth of the acoustic source) is also unknown, and is an independent quantity for each eruption. Our choice was to consider different depths for the acoustic source. The interpretation of results suggested how to deal with the conduit shape in future.

4.2 Boundary Element Method

The Boundary Element Method (BEM) is a numerical technique for solving a wide range of physical and engineering problems. Like other computational techniques as the Finite Element Method (FEM) and the Finite Difference Method (FDM), the BEM is a method for solving Partial Differential Equations (PDEs), expressed in form of integral equations. In the last decades the use of this method has been significantly improved, and successfully applied in different research fields like fluid mechanics, stress analysis, electromagnetics, fracture mechanics and acoustics.

The main advantage of the BEM is that the geometry is defined only by meshing the surfaces: in such a way, the method provides a complete solution in terms of boundary values. Especially in linear acoustics the BEM reveals powerful for problems where the acoustic domain is so large that can be realistically approximated as having infinite dimension (external problem): that can be the actual case of acoustic propagation in free air or in the ocean, where by using the BEM only a mesh of the surface of the body is required (Kirkup, 2007).

The integral equations that the BEM has to solve assume a boundary integral form, relating the solution at any points of the domain to functions defined only on the boundary of the bodies. Such boundary integral equations are discretized by representing surfaces as panels, and defining the boundary function on each panel of the mesh.

The code AcouSTO

AcouSTO (Acoustics Simulation TOol) is an open source BEM solver for the Kirchhoff-Helmholtz Integral Equation (KHIE). The code has been developed by Prof. Umberto Iemma and Eng. Vincenzo Marchese with the aim of a research group of the Department of Mechanical and Industrial Engineering at Roma Tre University in Rome (Italy) (Iemma *et al.*, 2009). The code is written in the language C and has been developed to enable parallel computing in order to solve numerical calculations on a distributed environment. Furthermore, the code can handle 3D boundaries of arbitrary geometry.

The code AcouSTO studies the acoustic problem in the Laplace domain, reducing it to the classical single-frequency formulation along the imaginary axis of the Laplace plane ($s = i\omega$). The problem can be written both in

terms of the velocity potential function φ or pressure perturbation p. As long as this work deals mainly with pressure perturbations, all the equations will be written depending on this quantity. If p and φ represents quantities in time domain, their corresponding in frequency domain, obtained by Laplace transformation, will be indicated as $\tilde{p}$ and $\tilde{\varphi}$.

The problem assumes this form:

$$\nabla^2\tilde{p}(\mathbf{x}) - \kappa^2\tilde{p}(\mathbf{x}) = \tilde{q}, \qquad \text{for } \mathbf{x} \in \mathcal{V} \tag{4.1}$$

with $\tilde{q}$ representing the acoustic sources present in the field, $\kappa = s/c$ being the complex wavenumber, $s = \alpha + i\omega$ the Laplace variable, and c the sound speed.

Wave propagation within the domain $\mathcal{V}$ described by (4.1) is associated to boundary conditions expressed in terms of the unknown function $\tilde{p}$ (or $\tilde{\varphi}$) and its normal derivative:

$$\gamma(\mathbf{x},\kappa)\tilde{p}(\mathbf{x},\kappa) + \lambda(\mathbf{x},\kappa)\frac{\partial\tilde{p}(\mathbf{x},\kappa)}{\partial n} = \tilde{f}(\mathbf{x},\kappa), \qquad \text{for } \mathbf{x} \in \partial\mathcal{V} \tag{4.2}$$

where γ, λ and f are known complex function of position and frequency. Assigning the appropriate values to the functions γ, λ and f it is possible to define different types of boundary conditions (Dirichlet, Neumann or Robin).

Once that the problem (4.1) has been solved in terms of $\tilde{p}$ or $\tilde{\varphi}$, the other quantity (if needed) can be easily obtained by the linearized *Bernoulli's theorem*:

$$\tilde{p} = -s\rho\tilde{\varphi}, \tag{4.3}$$

where ρ is the medium density.

If no acoustic sources are present in the domain ($\tilde{q} = 0$), the boundary integral formulation for $\tilde{p}$ assumes the form:

$$E(\mathbf{y})\tilde{p}(\mathbf{y}) = \oint_{\mathcal{S}} \left(G\frac{\partial\tilde{p}}{\partial n} - \tilde{p}\frac{\partial G}{\partial n} \right) \mathrm{d}\mathcal{S}(\mathbf{x}), \tag{4.4}$$

where the domain function $E(\mathbf{y})$ is defined as:

$$E(\mathbf{y}) = \begin{cases} 1 & \text{if } \mathbf{y} \in \mathcal{V}, \\ 1/2 & \text{if } \mathbf{y} \in \partial\mathcal{V}, \\ 0 & \text{if } \mathbf{y} \notin \mathcal{V}, \end{cases} \tag{4.5}$$

and the boundary $\mathcal{S}$ is defined as:

$$\mathcal{S} = \begin{cases} \partial\mathcal{V} & \text{for internal problems,} \\ \partial\mathcal{V} \setminus \mathcal{S}_\infty & \text{for external problems.} \end{cases} \tag{4.6}$$

The fundamental solution of equation (4.1) is described by the *Green's function*, G, defined as:

$$G(\mathbf{x},\mathbf{y},s) = \frac{-e^{-s\theta}}{4\pi r} = G_0 e^{-s\theta} \qquad \text{with } r = \|\mathbf{x}-\mathbf{y}\|, \text{ and } \theta = \frac{r}{c}. \tag{4.7}$$

Inserting the solution (4.7) in equation (4.4), we obtain the typical KHIE in the form:

$$E(\mathbf{y})\tilde{p}(\mathbf{y}) = \oint_{\mathcal{S}} \left(G_0 \frac{\partial \tilde{p}}{\partial n} - \tilde{p} \frac{\partial G_0}{\partial n} + s\tilde{p} G_0 \frac{\partial \theta}{\partial n} \right) e^{-s\theta} \mathrm{d}\mathcal{S}(\mathbf{x}). \tag{4.8}$$

AcouSTO uses equation (4.8) to solve the Boundary Value Problem (BVP) starting from the boundary conditions (4.2), and to represent the acoustic field once that the solution on the boundary is known (Iemma and Marchese, 2011). When $\mathbf{y} \in \partial\mathcal{V}$, equation (4.8) gives an integro-differential equation for the unknown $\tilde{p}$ on the boundary $\partial\mathcal{V}$ which can be solved from the boundary conditions $\tilde{\chi} = \partial\tilde{p}/\partial n$. Once that the solution in known on $\partial\mathcal{V}$, the code uses equation (4.8) as a boundary integral representation of $\tilde{p}$ at arbitrary points in the field (that play the role of microphones) as a function of the known distribution of $\tilde{p}$ and $\tilde{\chi}$ over the boundary.

AcouSTO solves equation (4.8) by means of a BEM. The boundary of the domain is divided into N quadrilateral panels on which the 0^{th} *order* approximation is performed: all the quantities are considered as constant within each panel. The surface integral in equation (4.8) is approximated with a sum of N panel integrals, using the collocation method: collocation points are located at the center of the panels. Performing this discrete approximation, equation (4.8) transforms in:

$$\frac{1}{2}\tilde{p}_n = \sum_{m=1}^{N} \left[B_{nm}\tilde{\chi}_m + (C_{nm} + sD_{nm})\,\tilde{p}_m \right] e^{-s\theta_{nm}}, \tag{4.9}$$

where n varies from 1 to N and the subscripts indicate the evaluation at the corresponding collocation point, and $\tilde{\chi} = \partial\tilde{p}/\partial n$. The integral coefficients are defined as:

$$B_{nm} = \int_{\mathcal{S}_m} G_0 \mathrm{d}\mathcal{S}, \quad C_{nm} = \int_{\mathcal{S}_m} \frac{\partial G_0}{\partial n} \mathrm{d}\mathcal{S}, \quad D_{nm} = \int_{\mathcal{S}_m} G_0 \frac{\partial \theta}{\partial n} \mathrm{d}\mathcal{S}. \tag{4.10}$$

Integral coefficients expressed by (4.10) are evaluated analytically by the code, and collected into $[N \times N]$ complex matrices B, C and D. Expressing the values of pressure and its normal derivative into $[N \times 1]$ column vectors, equation (4.9) can assume a matrix form:

$$\frac{1}{2}\underline{\tilde{p}} = \mathrm{B}\underline{\tilde{\chi}} + (\mathrm{C} + s\mathrm{D})\,\underline{\tilde{p}}. \tag{4.11}$$

The solution of the problem can be now expressed as:

$$\underline{\tilde{p}} = \mathrm{Y}^{-1}\mathrm{B}\underline{\tilde{\chi}}, \qquad \text{with } \mathrm{Y} = \left(\frac{1}{2}\mathrm{I} - \mathrm{C} - s\mathrm{D} \right), \tag{4.12}$$

which can be solved knowing the boundary conditions (4.2).

Once that the solution of the problem $\underline{\tilde{p}}$ is known on the boundary from equation (4.12), the same formulation is used to evaluate the complex pressure at the M microphones. Collecting the values of pressure $\tilde{p}^M$ at microphones into a $[M \times 1]$ column vector, we obtain:

$$\underline{\tilde{p}}^M = \mathrm{B}^M \underline{\tilde{\chi}} + \left(\mathrm{C}^M + s\mathrm{D}^M\right) \underline{\tilde{p}}, \tag{4.13}$$

where B^M, C^M and D^M are $[M \times N]$ matrices containing the integral coefficients which connect the values of $\tilde{p}$ and $\tilde{\chi}$ on the boundary with the solution $\tilde{p}^M$ at microphones.

AcouSTO can both solve the scattering of planar or spherical waves by multiple, arbitrarily shaped bodies, or propagate the radiation of vibrating closed surfaces with assigned wall motion.

For the task of the present work the code has been used to extract the matrices containing the effect of radiation from collocation points both on body elements (B and Y), and at the microphones (B^M, C^M and D^M). In doing this, the only input data necessary to include in the main file to run the code where:

- *geometry file*, that was built from the actual topography of Stromboli;
- *microphones file*, in which was included the actual position of the microphone where pressure signal has been recorded.

Symmetric geometry

If the geometry of the problem has a certain degree of symmetry, AcouSTO can benefit about that reducing the numerical effort required for the solution.

If a symmetry plane is present, the collocation points used to evaluate the solution can be distributed only along one of the two symmetric halves of the boundary surface, thus dividing by a factor two the number of equations of the resulting BEM system (Iemma and Marchese, 2011). Moreover, if the problem presents an axial symmetry, the code can evaluate the solution only along one half of a meridian circle, and the reduction of the computational effort depends on the number of "slices" in which the axially-symmetric geometry has been divided. Since both memory allocation and computational time grow according to N^2 (where N is the number of collocation points), using k symmetries these quantities will be proportional to $(N/k)^2$, with a clear advantage.

For a problem with no symmetry, the matrices involved in the system of equations will have dimension $[N \times N]$, with N being the number of panels (and in such a case, the number of collocation points), and the number of integral coefficient (4.10) that have to be evaluated to obtain the matrices is equal to $3 \times N \times N$. Differently, if the problem has a level of symmetry

equal to k, the dimension of matrices reduces to $[(N/k) \times (N/k)]$, and the number of integral coefficients reduces to $3 \times (N/k) \times N$. Figure 4.2 shows the reduction of collocation points with increasing symmetry for the case of a sphere.

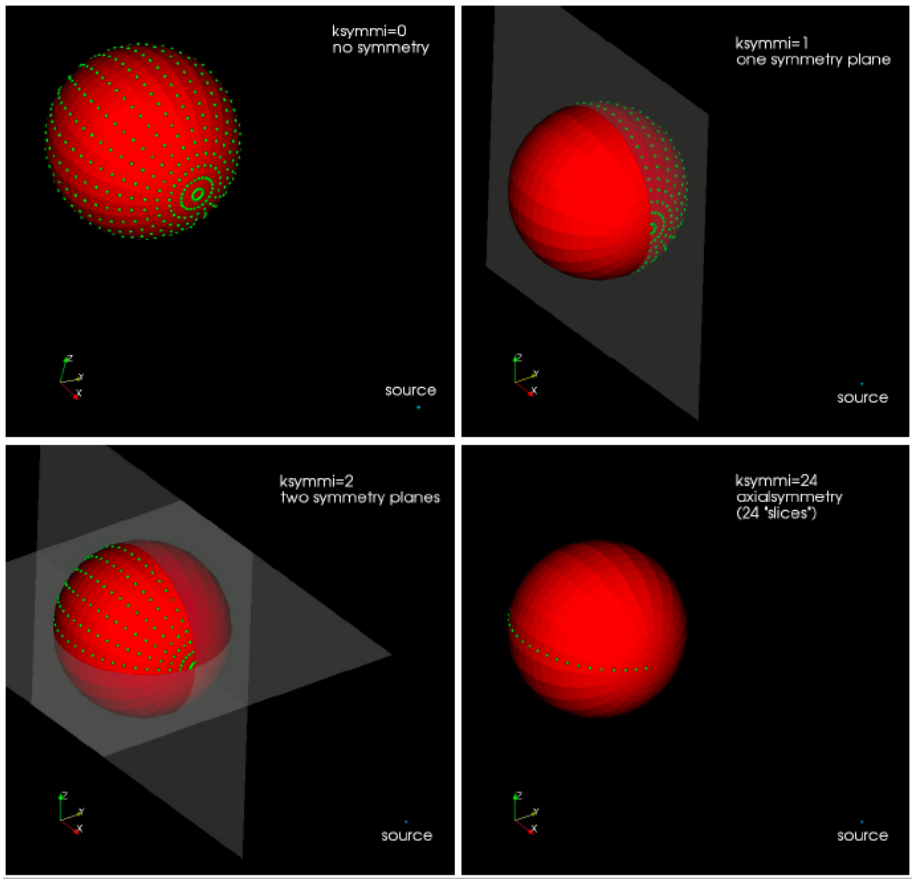

Figure 4.2: Control points (green) for different degrees of symmetry applied to a sphere with 24 "slices" (Iemma and Marchese, 2011).

4.3 Methodology

Since we are interested in obtaining information about the acoustic source in volcanic explosions from pressure recordings, we have to solve an inverse problem. However this kind of approach is possible only having high number of experimental data, like in seismology, where the number of equations exceeds that of the unknowns. In actual cases, with some or just one pressure records for an explosion, this method is ineffective.

Using AcouSTO it is possible to extract the *transfer function* connecting the pressure recorded at microphones around the volcano to boundary conditions on some panels of the mesh (which are considered as "containing" the source); obtaining such boundary conditions can provide some insight about the acoustic source.

In this work, a new methodology has been tested in order to evaluate the possibility to perform a complete acoustic source reconstruction using as input experimental measurements of pressure around the volcanic vent. Since only one microphone was used for this preliminary analysis, results could be considerably improved by using more experimental data.

4.3.1 Experimental data

In order to test this new procedure for volcano acoustic data inversion, accurate and reliable experimental data are needed. A peculiar infrasonic data was provided by Prof. Maurizio Ripepe of Department of Earth Sciences of University of Florence (Italy). The signal is the result of the stacking between 150 pressure signals recorded at Stromboli by the infrasonic sensor PZZ, placed 160 m above the volcanic vents, at a distance of 280 m from the crater terrace (Figure 4.3). Pressure signals refers to ordinary strombolian activity generated by the SW crater. A 100 Hz sampling rate was used for data acquisition. Figure 4.4 shows the shape of this test signal.

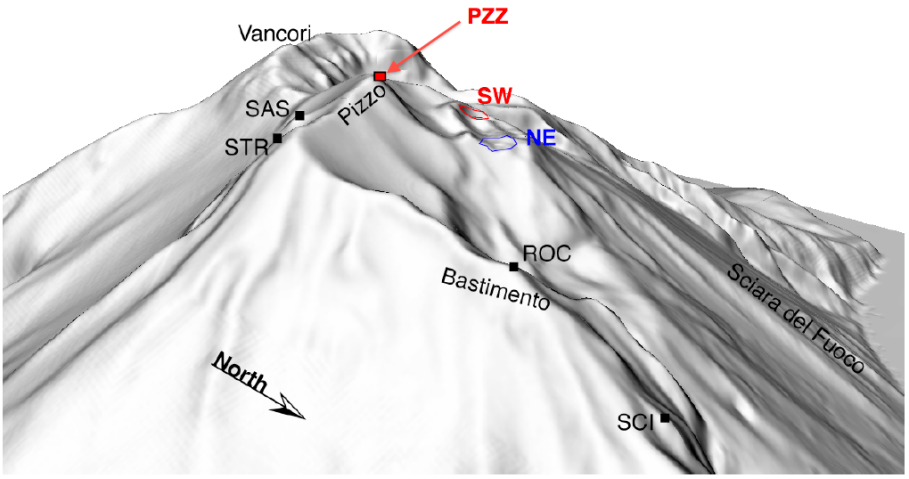

Figure 4.3: Summit craters and infrasonic sensors installed at Stromboli from geologists of University of Florence. The nomenclature is the same of Figure 3.11. SW (red) and NE (blue) represents two active vents of Stromboli volcano (Modified figure of Lacanna, 2010).

Since represents the stacking of many recordings, the signal can be considered as an infrasonic "signature" of SW vent at Stromboli associated to

ordinary explosions. Unfortunately, any information about the explosion depth are completely unknown; furthermore, the stacking operation necessarily mix together signals from explosion occurred at different depths. However, for a preliminary analysis, this data represents a pretty good test signal since has been recorded at a very short distance (it is not so safe to approach an active volcano!), and volcanic vent is perfectly in line of sight.

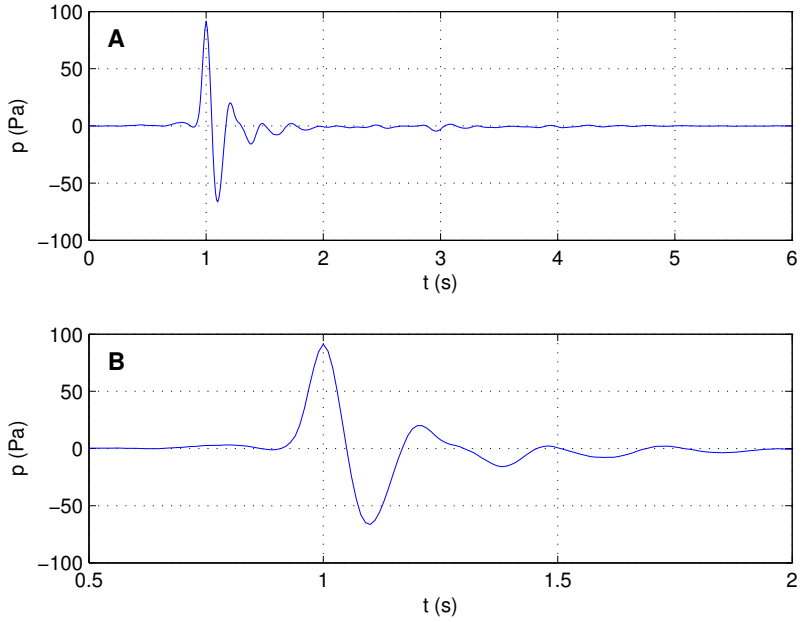

Figure 4.4: A. Stacking of 150 pressure signals recorded at Stromboli at a distance of 280 m from active vents. Ordinary strombolian activity was generated from SW crater. A 100 Hz sampling rate was used for data acquisition. B. Zoom of the first 1.5 s: main oscillation has a duration of about 0.2 s.

4.3.2 Geometry building

Since it will be used an actual pressure signal recorded at Stromboli, it is necessary to build the geometry starting from the Digital Elevation Model (DEM) of the volcano. Figure 4.3 shows a 3D image of the summit zone of Stromboli. Since both the volcanic vent and the microphone are located at the top of the volcano, it can be possible to build the geometry considering only this portion of Stromboli.

As long as the mesh size depends on the wavelength used by the BEM, it is important to accurately define the minimum length for a panel. Usually, the linear length of a panel must be at least 1/5 of the wavelength studied.

Since a maximum frequency of 10 Hz will be used in this analysis, I chose a minimum panel length of $\lambda/10$, in order to have a good accuracy: that gives a minimum panel length of 3.4 m. Since this quantity represents the step used to build the whole geometry, the entire number of panels of the mesh will be in the order of 10^5. This value is pretty high and will require long computational times for the runs.

To overcome this trouble, AcouSTO permits the use of symmetries. In order to use the maximum level of symmetry, the geometry has built as axially-symmetric. This of course represents an approximation of the actual geometry of Stromboli, but the computing power available did not permit a higher level of accuracy. Anyway, since this work represents a first attempt to study the phenomenon of volcano acoustics by an inverse problem, on the basis of our results a more accurate geometry can be a topic for future works.

A topographic section passing for the SW vent and the infrasonic recorder PZZ was used to build the profile of Stromboli, in the zone of interest. In order to use the axial symmetry with AcouSTO, a conic geometry with the volcanic vent on the axis was considered: Figure 4.5 shows the actual section of Stromboli from SW vent to the PZZ station, and the approximated profile used in the analysis.

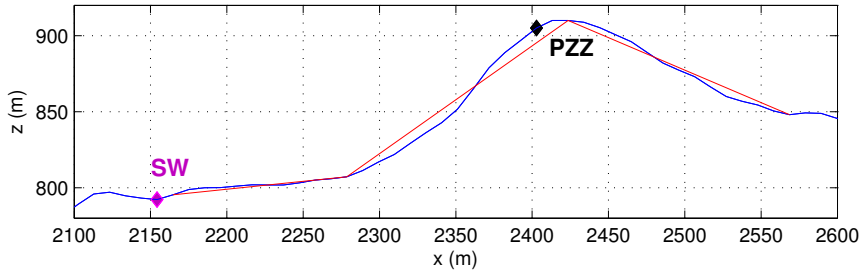

Figure 4.5: Section of Stromboli topography (blue line) from the SW vent (magenta diamond) to the PZZ infrasonic station (black diamond). Red line represents the approximated geometry used for our analysis.

The section showed in Figure 4.5 was used to built the mesh by using the 3D graphic platform Blender. A plugin to convert files from a Blender to an AcouSTO format is provided in the AcouSTO installation package. Since the acoustic source (represented by boundary conditions χ on some mesh panels) will be placed in the volcanic conduit, three geometries with different depth of the source were considered: 0 m (the source lies on the volcanic vent, with no acoustic propagation in the conduit), 20 m and 50 m. Figure 4.6 show the *bezier* curves used in Blender to build the meshes. A slope developing down to 100 m beneath the volcanic vent was considered to avoid any problems connected to boundary effects at the edges of the mesh.

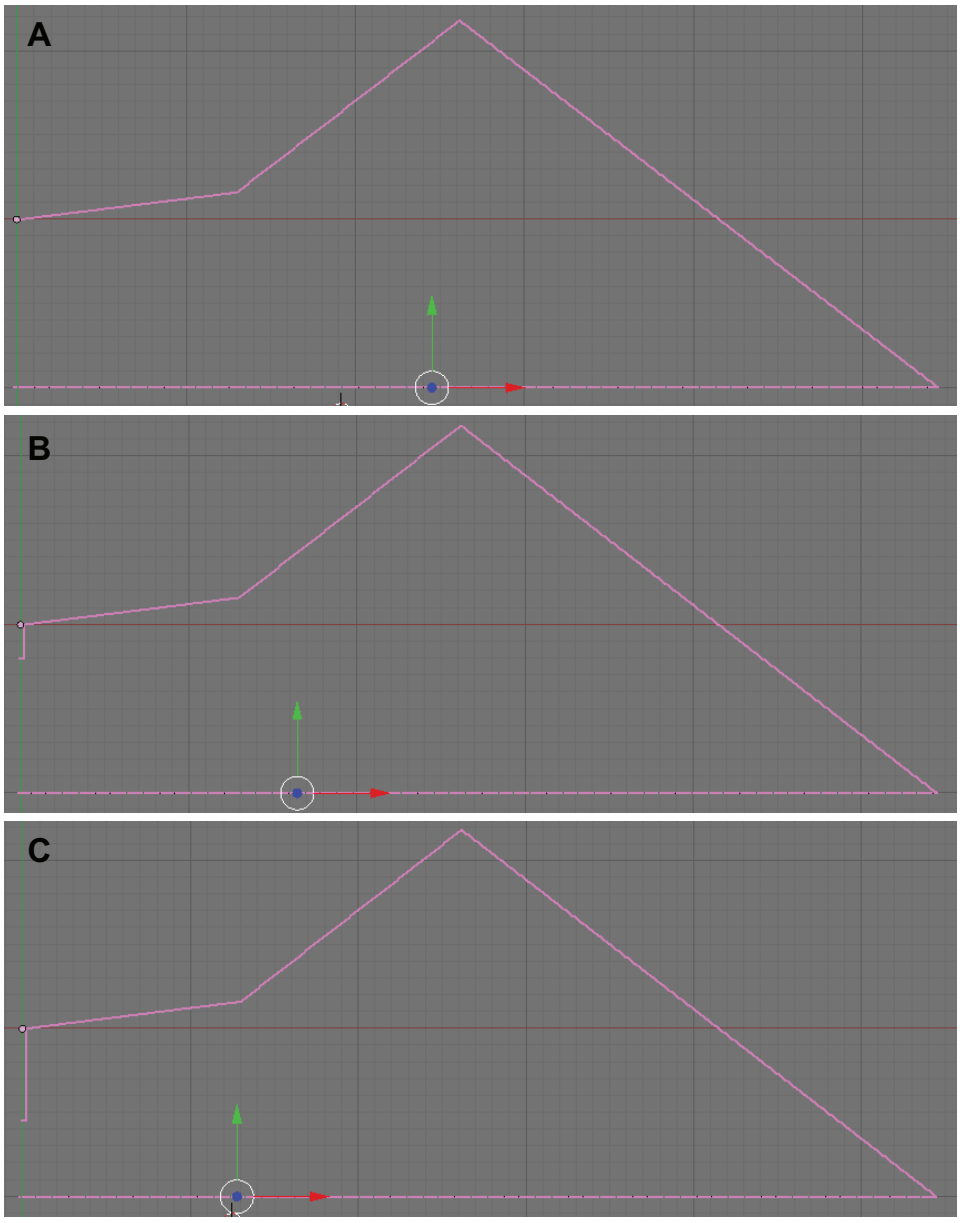

Figure 4.6: *Bezier curves* used in BLENDER to build the geometry. A. No volcanic conduit; source at the free-air level. B. Volcanic conduit with a depth of 20 m. C. Volcanic conduit with a depth of 50 m.

The axially-symmetric geometry was built by revolution of the *bezier* curves showed in Figure 4.6. A number of 512 "slices" was used to accurately maintain the ratio between panel dimension and radiation wavelength. Figure 4.7 shows the final mesh built by BLENDER for the case with a conduit of 0 m of depth.

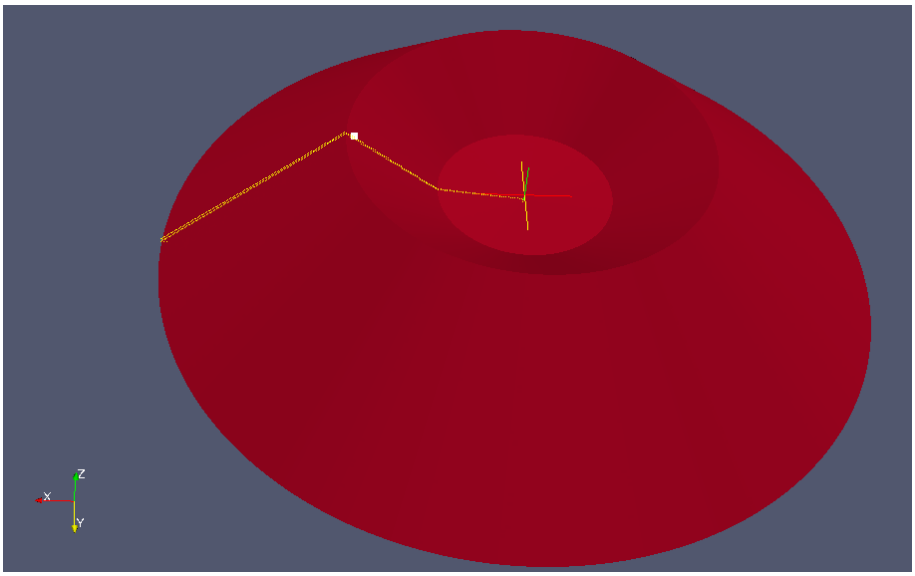

Figure 4.7: Final geometry of the volcanic cone. Yellow lines represent the two thin slices on which the collocation points for integral calculation are placed. White square represents the position of microphone. Image obtained by the software PARAVIEW.

4.3.3 The inverse problem

If we have M microphones and N mesh panels, pressure at microphones $\underline{\tilde{p}}^M$ is described by a $[M \times 1]$ column vector as described by equation (4.13). Inserting the expression of $\underline{\tilde{p}}$ (4.12) in equation (4.13), it is possible to relate the pressure at microphones $\underline{\tilde{p}}^M$ to the boundary conditions $\underline{\tilde{\chi}}$ on panels of the mesh:

$$\underline{\tilde{p}}^M = \mathrm{B}^M \underline{\tilde{\chi}} + \left(\mathrm{C}^M + s\mathrm{D}^M\right) \mathrm{Y}^{-1} \mathrm{B} \underline{\tilde{\chi}} = \mathrm{H}(\omega) \underline{\tilde{\chi}}. \tag{4.14}$$

The transfer matrix $\mathrm{H}(\omega)$ has a $[M \times N]$ dimension, and is defined as:

$$\mathrm{H}(\omega) = \mathrm{B}^M + \left(\mathrm{C}^M + s\mathrm{D}^M\right) \left(\frac{1}{2}\mathrm{I} - \mathrm{C} - s\mathrm{D}\right)^{-1} \mathrm{B}. \tag{4.15}$$

Equation (4.15) contains the whole effect of acoustic propagation from any panel of the mesh to the M microphones, for a given angular frequency ω.

From equation (4.14) the acoustic pressure "recorded" at the n^{th} microphone is defined as:

$$\tilde{p}_n^M = \sum_{m=1}^{N} H_{nm}(\omega)\tilde{\chi}_m. \tag{4.16}$$

The code AcouSTO normally calculates the matrices and use them to evaluate the solution. For this peculiar application, two classes of the code (*matrices.c* and *pre_mic.c*) were modified in order to print all the necessary matrices to build H(ω):

- those containing the effect on body elements: B and Y, with dimension $[N \times N]$;
- those containing the effect on microphones: B^M, C^M and D^M, having dimension $[M \times N]$.

By equation (4.15), it is possible to obtain the matrix H(ω) for a given frequency. Performing many runs for the entire set of frequencies interesting for the analysis, it can be possible by equation (4.14) to extract pressure at microphones $\tilde{p}^M$ from boundary conditions $\tilde{\chi}$ on panels and vice versa.

Transfer matrix extraction using axial symmetry

In absence of symmetries, the body element matrices B, C, and D of equation (4.11) have dimension of $[N \times N]$, where N is the total number of panels of the mesh. An element n of equation (4.11) can be expressed as:

$$\frac{1}{2}\tilde{p}_n = \sum_{m=1}^{N} \left[B_{nm}\tilde{\chi}_m + (C_{nm} + sD_{nm})\,\tilde{p}_m\right], \tag{4.17}$$

where $\tilde{p}_m$ and $\tilde{\chi}_m$ can assume N different values.

If we use a level of symmetry equal to k, the dimension of matrices B, C and D reduces to $[(N/k) \times (N/k)]$. In this condition, the summation in (4.17) assumes the form:

$$\frac{1}{2}\tilde{p}_n = \sum_{m=1}^{N/k} \left[B_{nm}\tilde{\chi}_m + (C_{nm} + sD_{nm})\,\tilde{p}_m\right], \tag{4.18}$$

where now each matrix element B_{nm}, C_{nm} and D_{nm} contains the summation over k symmetric panels, and there is a maximum of N/k possible values for $\tilde{p}_m$ and $\tilde{\chi}_m$.

To understand the process of reduction of dimension in the body matrices, let's look at the simple 2D example depicted in Figure 4.8.

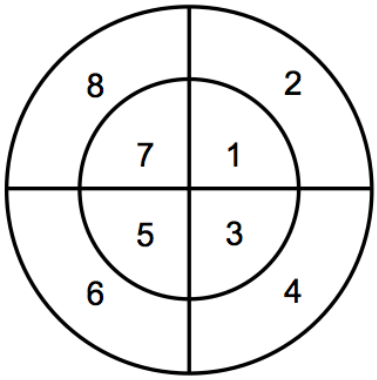

Figure 4.8: Eight-panels mesh with axial symmetry. Only two panels are necessary to calculate the quantities $\tilde{p}$ and $\tilde{\chi}$.

For this problem there is a total of eight panels, then $\tilde{p}$ and $\tilde{\chi}$ can assume eight different values. If we use the maximum level of symmetry, we can assume that:

$$\begin{aligned} &\tilde{\chi}_1 = \tilde{\chi}_3 = \tilde{\chi}_5 = \tilde{\chi}_7; \quad \tilde{p}_1 = \tilde{p}_3 = \tilde{p}_5 = \tilde{p}_7; \\ &\tilde{\chi}_2 = \tilde{\chi}_4 = \tilde{\chi}_6 = \tilde{\chi}_8; \quad \tilde{p}_2 = \tilde{p}_4 = \tilde{p}_6 = \tilde{p}_8. \end{aligned} \tag{4.19}$$

In this case, equation (4.18) becomes:

$$\frac{1}{2}\tilde{p}_n = \sum_{m\ odd} \left(B_{nm}\tilde{\chi}_1 + C_{nm}\tilde{p}_1\right) + \sum_{m\ even} \left(B_{nm}\tilde{\chi}_2 + C_{nm}\tilde{p}_2\right), \tag{4.20}$$

with n and m assuming only values 1 and 2.

The advantage in the use of symmetries in AcouSTO is twofold: from one side makes runs faster and less onerous in terms of memory allocation; from the other gives smaller matrices, that means "lighter" files (body matrixes can easily reach the dimension of some GB), which provide a faster post-processing on the solutions.

Having built a cylindrically-symmetric geometry with a total of N panels on 512 sides, AcouSTO permits a level of symmetry $k = 512$. Unfortunately, the panel numeration made by Blender in building the mesh reduces the highest level of symmetry for a factor two: then the simulation with AcouSTO has been performed with a level of symmetry equal to 256, with a significative gain in terms of memory allocation (but also in computing times) with respect to the case without symmetries. Considering that the meshes of Figure 4.6 were composed respectively by 176640, 179712 and 184832 panels, by using a level of symmetries equal to 256, collocation points were reduced to only 690, 702 and 722: to have an idea about the benefit, for the first geometry memory allocation drops for 176640^2 to only 690^2!!!

In this condition, and considering only one microphone (since we one experimental data), equation (4.16) reduces to:

$$\tilde{p}^M = \sum_{m=1}^{N/256} H_m(\omega)\tilde{\chi}_m. \tag{4.21}$$

where the summation runs over the minimum number of collocation points (Figure 4.7). Now, since the $\tilde{\chi}_m$ represents the source conditions radiating sound, there will be only two panels with $\tilde{\chi} \neq 0$, located inside the vent (Figure 4.9).

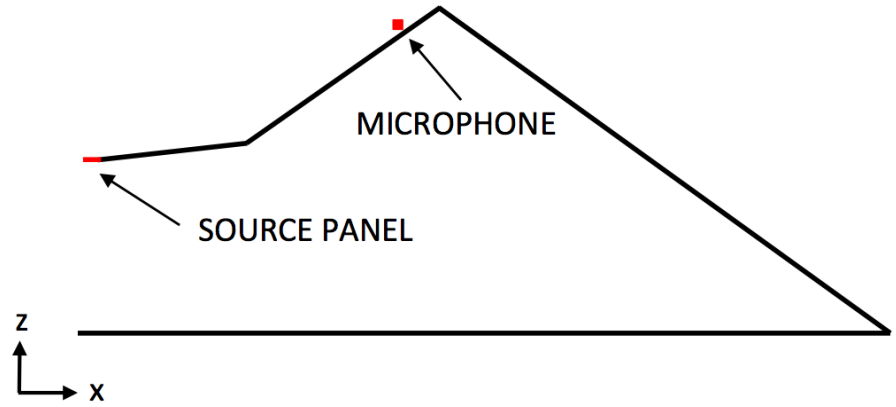

Figure 4.9: Source panels are located at the bottom of volcanic conduit. Only these panels contribute to the generation of sound. The level of symmetry used reduces the number of significative panels to only two.

Considering for the task of simplicity that the indexes of these two panels are 1 and 2, equation (4.21) becomes:

$$\tilde{p}^M = H_1(\omega)\tilde{\chi}_1 + H_2(\omega)\tilde{\chi}_2 = 2H(\omega)\tilde{\chi}, \tag{4.22}$$

because $H_1 = H_2 = H$ and $\tilde{\chi}_1 = \tilde{\chi}_2 = \tilde{\chi}$ (remember that we are using the axial symmetry, although for the simulations is reduced for a factor two).

Since we are solving the problem in the frequency domain, all these quantities $\tilde{p}^M$, H and $\tilde{\chi}$ will be complex. Then, for a given frequency equation (4.22) assumes the form:

$$\mathrm{Re}(\tilde{p}^M) + i\ \mathrm{Im}(\tilde{p}^M) = 2\left[\mathrm{Re}(H) + i\ \mathrm{Im}(H)\right]\left[\mathrm{Re}(\tilde{\chi}) + i\ \mathrm{Im}(\tilde{\chi})\right]. \tag{4.23}$$

Separating equation(4.23) in two equations valid independently for real and imaginary part, we obtained a linear system of two equation depending on two unknowns:

$$\begin{cases} 2\left[\mathrm{Re}(H)\mathrm{Re}(\tilde{\chi}) - \mathrm{Im}(H)\mathrm{Im}(\tilde{\chi})\right] = \mathrm{Re}(\tilde{p}^M) \\ 2\left[\mathrm{Im}(H)\mathrm{Re}(\tilde{\chi}) + \mathrm{Re}(H)\mathrm{Im}(\tilde{\chi})\right] = \mathrm{Im}(\tilde{p}^M) \end{cases} \tag{4.24}$$

Depending on the case, the couple of unknowns can be the pressure at the microphone $\tilde{p}^M$ or the source condition $\tilde{\chi}$ ($\mathrm{Re}(H)$ and $\mathrm{Im}(H)$ are two numbers calculated by the code). The second case is that studied in this work, where for a given frequency $\mathrm{Re}(\tilde{p}^M)$ and $\mathrm{Im}(\tilde{p}^M)$ are the real and imaginary part of the Fourier transform of the signal showed in Figure 4.4.

If the linear system admits real solutions, for a given frequency it is possible to obtain the normal derivative of pressure $\tilde{\chi}$ on "source panels" that generated the pressure perturbation $\tilde{p}^M$ measured by the infrasonic station PZZ.

4.3.4 Frequency set

Since the code AcouSTO works in frequency domain, but we deal with pressure signals varying with respect to the time, a certain number of frequencies has to be chosen for the analysis to perform an accurate reconstruction of time dependent quantities.

Transforming a digital signal from time to frequency domain by means of a Fourier transform, the frequency spectrum obtained will depend on temporal axis features:

- the maximum detectable frequency is equal to the half of sampling rate (*Nyquist-Shannon sampling theorem*);
- frequency step $\Delta\nu$ is equal to the inverse of total duration T of signal in time:

$$\Delta\nu = 1/T. \tag{4.25}$$

Similarly, performing an inverse Fourier transform, the temporal axis depends on the frequency used. Then, the choice of frequencies to run with AcouSTO will determine the features of reconstructed signals in time.

Obviously, the best frequency set is the complete spectrum provided by the Fourier transform. However, since the reference pressure signal used in this work has a total duration of 10 s and was acquired at a sampling rate of 100 Hz, the number of frequencies would be 501. Since the computing time and power available does not permit the use of such a huge number of frequencies, the choice of a reliable subset reveals necessary.

Figure 4.10 shows the frequency spectrum obtained from the pressure signal depicted in Figure 4.4. Since the peak frequency occurs around 4 Hz (related to the first pressure pulse in time), and the frequency content above 10 Hz drops significantly, we chose to confine our analysis between 0 and 10 Hz. When we perform the Fourier inversion, that choice determines a time domain signal subsampled down to a 20 Hz rate (the double of maximum frequency).

The choice of the frequency step between 0 and 10 Hz is even more tricky: that will determine from equation (4.25) the total duration of the

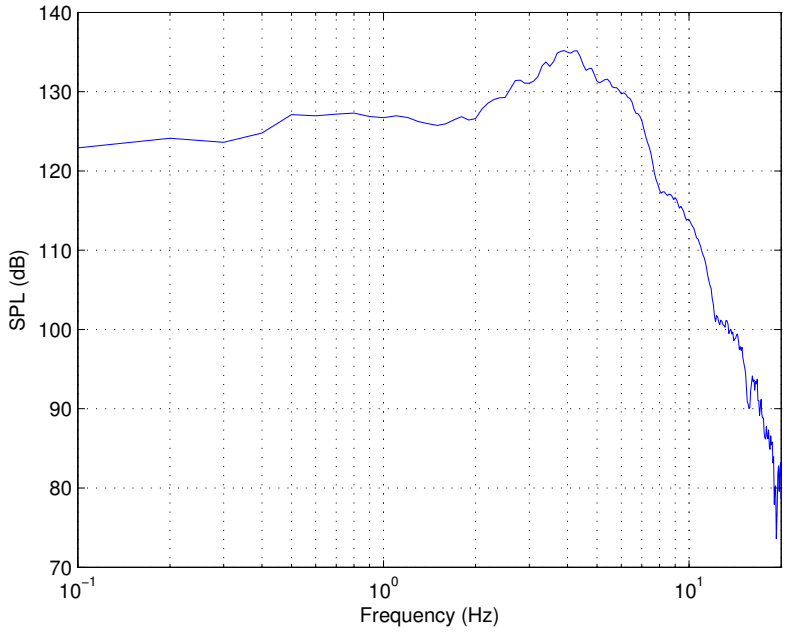

Figure 4.10: Power spectrum (SPL) of pressure signal showed in Figure 4.4.

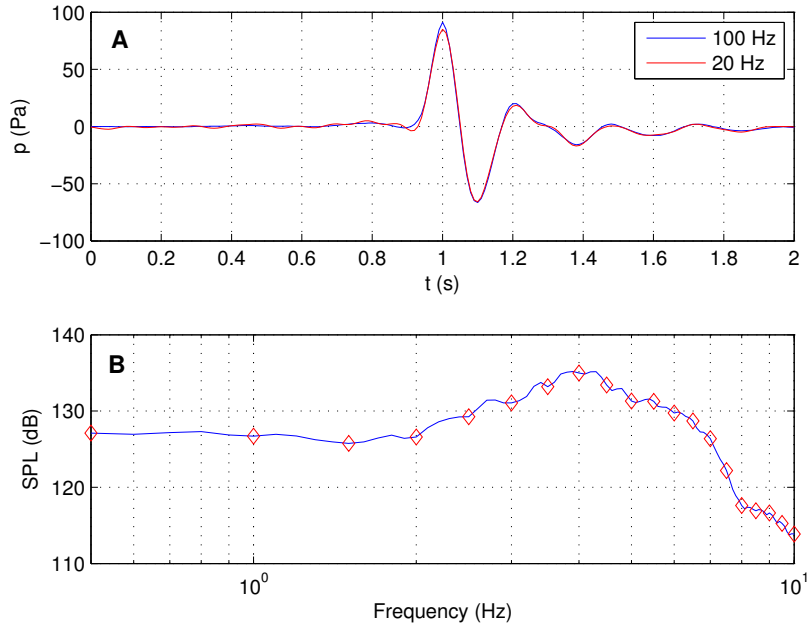

Figure 4.11: A. Pressure signal measured with a 100 Hz sampling frequency (blue), and signal reconstruction from Fourier inversion at a sampling rate of 20 Hz (red line). B. Entire power spectrum of test signal (blue line) and the 21 values (red diamonds) used for our analysis.

reconstructed signal. Since the process is extremely impulsive, and first pressure oscillations (connected more to the source process that to propagation effects) have a duration of about 1 s (Figure 4.4), we chose to perform a reconstruction of 2 s of signal: setting the frequency step $\Delta\nu$ to 0.5 Hz, gives a total number of 21 frequencies. Of course this is an approximation, based on the supposed short-duration of the entire source process: since the explosion of a gas bubble during a strombolian eruption is an impulsive event, the same has been considered for the generation of the infrasonic signal. However, any refinements can be performed in the future to improve the accuracy of this methodology.

Figure 4.11A shows the reconstruction of pressure signal on the basis of the assumption made. Although red line was obtained by a subsampling at 20 Hz, its shape fits almost perfectly the original signal (blue line). Figure 4.11B show the set of frequencies used for the analysis (red diamonds); the 21 frequencies seems to accurately represent the entire spectrum (blue line).

With such a frequency set, 21 runs with ACOUSTO were performed, to extract the transfer matrix $\mathrm{H}(\omega)$ for each value of ω. By the previously described methodology, the normal derivatives of pressure $\tilde{\chi}$ on source panels has been obtained solving the linear system (4.24) for each of the 21 frequencies.

4.4 Optimization method

Since the linear system (4.24) comes from the use of a high level of symmetry, any future refinement (as the use of the actual topography of Stromboli) will prevent such analytical solution. To overcome this limitation we developed a bi-objective optimization, that permits to obtain the source conditions $\tilde{\chi}$ at any panel of the mesh also for more complex geometries. By comparing the results with those obtained solving the system (4.24) we tested the performances of our optimization methodology, to confidently use it for future works.

The optimization is a mathematical procedure designed to find the "best values" for a given set of N variables $\mathbf{x} = [x_1, ..., x_n]$ that makes an *objective function* $f(\mathbf{x})$ assuming a peculiar value (the maximum or the minimum, depending on the case). Usually the problem contains also some constraints, and a general formulation assumes this form:

$$\begin{aligned} &\text{minimize (or maximize)} f(\mathbf{x}), \quad \text{with } \mathbf{x} \in \mathcal{D} \\ &\text{subjected to } g_{m1}(\mathbf{x}) \leq 0, \\ &\text{and to } h_{m2}(\mathbf{x}) = 0, \end{aligned} \tag{4.26}$$

where $\mathcal{D}$ is the domain of existence of variables $\mathbf{x}$, and $g_{m1}(\mathbf{x})$ and $h_{m2}(\mathbf{x})$ are respectively M_1 inequality and M_2 equality constraints.

Many physical and engineering applications involves more objective functions, sometimes competing, that should be optimized simultaneously. A simple example is the case of maximization of the performance of a system while minimizing its cost. The possible cases in multi-objective optimization problems are two:

- cooperative problems, in which the optimum solution is the same for all the objectives;
- competing problems, where an improvement in one objective causes a degradation in another.

A typical multi-objective optimization problem has a definition similar to equation (4.26), but instead of having a single objective function $f(\mathbf{x})$, appears the function $\mathbf{J} = [J_1(\mathbf{x}), ..., J_z(\mathbf{x})]$, where each of the Z objective functions $J_i(\mathbf{x})$ depends on the entire set of N variables $\mathbf{x}$. The simplest way to solve a multi-objective problem is to reduce to a minimization of a unique objective function defined as (Kim and de Weck, 2005):

$$\min_{\mathbf{x}} \tilde{J} = \sum_{i=1}^{z} \frac{\lambda_i}{sf_i} J_i(\mathbf{x}), \tag{4.27}$$

where $\tilde{J}$ represents a weighted-sum of the individual objectives J_i, and sf_i and λ_i are respectively the scaling factor and the weight of the i^{th} objective function $J_i(\mathbf{x})$. Typically the weights λ_i are defined to satisfy the condition:

$$\sum_{i=1}^{z} \lambda_i = 1, \quad \text{with } \lambda_i \geq 0 \ \forall i. \tag{4.28}$$

In multi-objective optimizations, instead of having a unique solution for $\mathbf{x}$, there is a *Pareto optimal set* (Pareto, 1906), in which the the "best solution" can be chosen. Comparing two solutions $\mathbf{x}_1$ and $\mathbf{x}_2$, $\mathbf{x}_1$ is said to *dominate* solution $\mathbf{x}_2$ if satisfy the following conditions (Deb, 2001; Antoine, 2004):

1. solution $\mathbf{x}_1$ is no worse than $\mathbf{x}_2$ for all objectives;
2. solution $\mathbf{x}_1$ is strictly better than $\mathbf{x}_2$ for at least one objective.

The complete set of solutions that are non-dominated by any other solution represents the Pareto optimal set, or non-dominated set. For a bi-objective optimization, these solutions can be graphically represented by the so-called *Pareto front* (Figure 4.12). The optimal solution of the problem will be found on the Pareto front. The choice of a point along the Pareto front depends on the physical meaning of the non-dominated solutions.

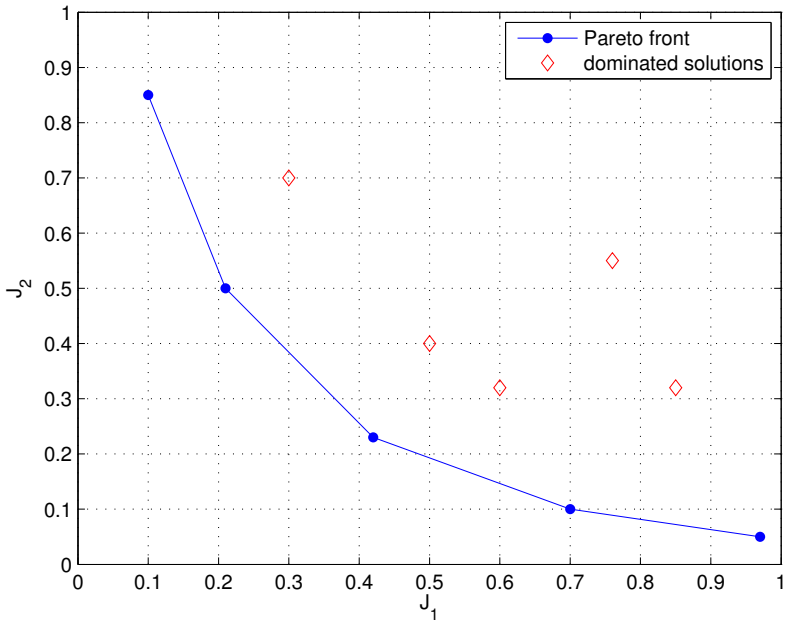

Figure 4.12: Non-dominated solutions along the Pareto front (blue) and dominated solutions (red diamonds) above it.

In last decades many methods were developed in order to find the optimal set of solutions and outline the Pareto front. One of the most widely used methods is the weighted-sum introduced by Zadeh (1963): the method consists in transforming a vectorial multi-objective problem in a set of single-objective scalar problems as in equation (4.27). A development of this method was proposed by Kim and de Weck (2005), and is the one followed in the present work. Two other methods commonly used to find Pareto optimal solutions are the Evolutionary Algorithms (Fonseca and Fleming, 1995) and the Normal-Boundary Intersection (NBI), which provides a uniform spacing between solutions and can manage problems with non-convex Pareto fronts (Das and Dennis, 1998).

4.4.1 Adaptive weighted-sum optimization

Since the optimization for the present work had to deal with two objective functions, we chose to follow the Adaptive Weighted-Sum (AWS) method proposed by Kim and de Weck in 2005. With respect to the standard weighted-sum method, the AWS had the advantage that is capable to identify the solutions even in presence of varying curvature in the Pareto front. This can be a pretty good advantage, since we don't have any *a priori* information about the features of the Pareto front.

A typical weighted-sum problem work with a function defined as:

$$\min_{\mathbf{x}} \left[\lambda \frac{J_1(\mathbf{x})}{sf_1(\mathbf{x})} + (1-\lambda) \frac{J_2(\mathbf{x})}{sf_2(\mathbf{x})} \right], \tag{4.29}$$

subjected to the constraints $g(\mathbf{x}) \leq 0$ and $h(\mathbf{x}) = 0$, with $\lambda \in [0, 1]$. $J_1(\mathbf{x})$ and $J_2(\mathbf{x})$ are the two objective function to be mutually minimized, and sf_1 and sf_2 are normalization factors.

Solving the problem by a typical weighted-sum method, if the Pareto front has a varying curvature most solutions concentrate in the region whose curvature is relatively high (near the anchor points and the inflection point), with no solutions found in the concave region. Moreover, the solutions will be not uniformly distributed.

The AWS provide many advantages with respect to the standard weighted-sum method (Kim and de Weck, 2005):

- permits to obtain solutions in convex regions of the Pareto front with non-uniform curvature (Figure 4.13A);
- permits to obtain solutions in non-convex regions of non-dominated solutions of the Pareto front (Figure 4.13B);
- permits to obtain solutions in non-convex regions of dominated solutions of the Pareto front (Figure 4.13C);
- provides more uniformly distributed solutions.

Main steps followed by the AWS method consist in:

1. apply a usual weighted-sum method with a small number for the weighting factor λ;
2. identify feasible regions between solutions in which refinements have to be performed;
3. apply another weighted-sum method in each feasible region, with additional inequality constraints that ensure to obtain only non-dominated solutions (if present);
4. repeat the operations at points 2 and 3 until a termination criterion is satisfied.

Figure 4.14 illustrates briefly the steps followed by the AWS method.

The first step of the methodology consist in performing a bi-objective optimization using the weighted-sum method, with a small number of initial division $n_{initial}$. This parameter determines the step of the weighting factor λ as $\Delta\lambda = 1/n_{initial}$. A large step $\Delta\lambda$ provides a small number of solutions.

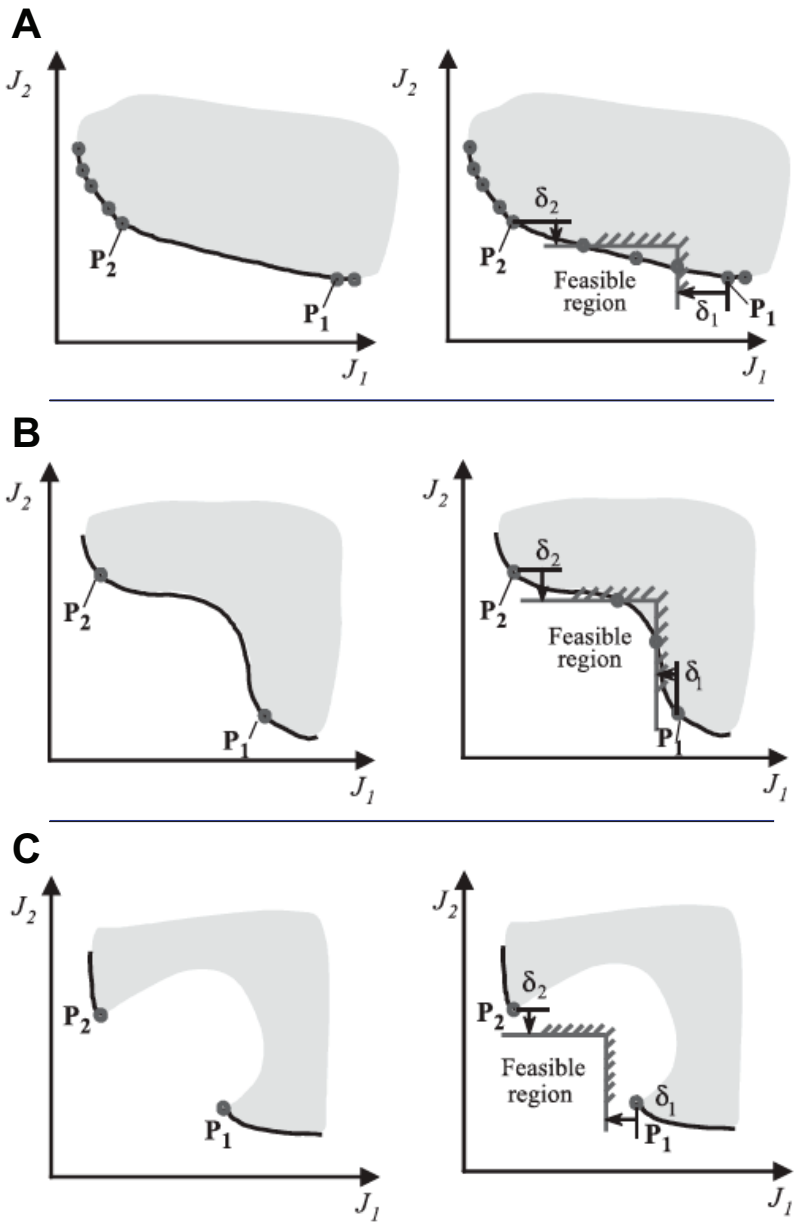

Figure 4.13: Advantages of the ASW method with respect to the standard weighted-sum. A. Pareto front with non-uniform curvature. B. Pareto front with non-convex regions of non-dominated solutions. C. Pareto front with non-convex regions of dominated solutions (Kim and de Weck, 2005).

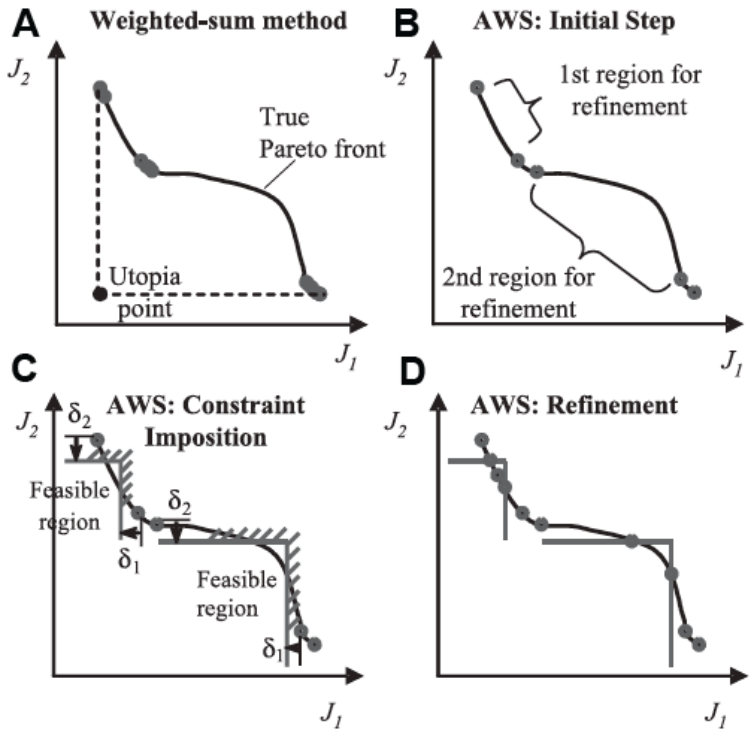

Figure 4.14: Main steps of the AWS optimization method. A. Initial weighted-sum optimization. B. Identification of feasible regions for further refinements. C. Sub-optimization in the feasible regions with additional inequality constraints. D. Iteration of the method until a uniform Pareto front is obtained (Kim and de Weck, 2005).

Once the first solutions are obtained, the next step consists in removing overlapping solutions. Often the weighted-sum method provided nearly identical solutions. Comparing the Euclidean distances between all the neighboring solutions with a threshold value ϵ, all solutions with distances lower than ϵ are deleted, except one.

In the third step is calculated the number of further refinements necessary in each of the regions between two neighboring solutions. This quantity is determined as:

$$n_i = round\left(C\frac{l_i}{l_{av}}\right), \tag{4.30}$$

where n_i is the number of further refinements for the i^{th} region, l_i is the length of the i^{th} segment, l_{av} the average length of all the segments, and C is a constant. In order to have an integer number, the function *round* is applied to the right member of equation (4.30). If $n_i \leq 1$ no more refinements are needed in the i^{th} region. Otherwise, the procedure goes to the following step.

In the regions were a refinement is required, the user choose an offset distance δ_J along the segment connecting the end points $\mathbf{P}_1$ and $\mathbf{P}_2$ (Figure 4.15): this quantity will determine the final density of the solutions along the Pareto front. No more refinements are conduced between two point distant less than δ_J. The offset value δ_J determines also the additional conditions to be satisfied during the sub-optimization inside a feasible region, defined as offset distances parallel to the objective axes (Figure 4.15).

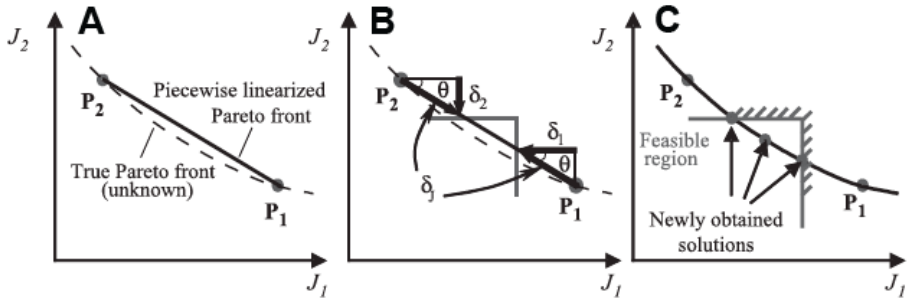

Figure 4.15: Sub-optimization in a feasible region. A. segment connecting two neighboring points. B. Set up of the additional inequality constraint from δ_1 and δ_2. C. New points on the Pareto front found by the sub-optimization (Kim and de Weck, 2005).

The slope of the segment connecting $\mathbf{P}_1$ and $\mathbf{P}_2$ is calculated as:

$$\theta = \arctan\left(-\frac{P_1^y - P_2^y}{P_1^x - P_2^x}\right), \tag{4.31}$$

with $\mathbf{P}_1 = (P_1^x, P_1^y)$ and $\mathbf{P}_2 = (P_2^x, P_2^y)$. The offset distances δ_1 and δ_2 illustrated in Figure 4.15 are defined as:

$$\begin{aligned} \delta_1 &= \delta_J \cos\theta, \\ \delta_2 &= \delta_J \sin\theta. \end{aligned} \tag{4.32}$$

A sub-optimization with the weighted-sum method in the form of equation (4.29) is then performed in the feasible region, with the additional inequality constraints:

$$\begin{aligned} J_1(\mathbf{x}) &\leq P_1^x - \delta_1, \\ J_2(\mathbf{x}) &\leq P_2^y - \delta_2. \end{aligned} \tag{4.33}$$

After a first sub-optimization inside a feasible region, any nearly overlapping solutions are deleted as described above. If there are solutions distant more than δ_J, a further sub-optimization with the additional inequalities (4.33) is performed again.

The segments in which no converged optimum solutions are obtained are removed from the set for further refinement, because in this case these regions are non-convex and do not contain Pareto optimal solutions (Kim and de Weck, 2005).

When no more segments between neighboring points are longer than the fixed distance δ_J, the optimization procedure is completed.

4.4.2 Objective functions description

The definition of our objective functions $J_1(\mathbf{x})$ and $J_2(\mathbf{x})$ starts from the linear system (4.24). With the AWS optimization we developed a method alternative to (4.24) to find the normal derivative of pressure on source panels $\tilde{\chi}$, from the measured signal. In doing this, we concentrated on a sound matching between two signals:

- the experimental pressure signal measured at Stromboli, $\tilde{p}_E^M$;
- the pressure that would be measured at the microphone, for a given source function $\tilde{\chi}$:
$$\tilde{p}_O^M = \mathbf{H}\tilde{\chi}.$$

All these quantities $\tilde{p}^M$, H and $\tilde{\chi}$ depends on frequency.

Varying the source parameters $\tilde{\chi}$, the optimal solutions are obtained by matching the two sounds. Since we are working in the frequency domain, we have to deal with amplitude and phase (or real and imaginary part) of the signal. That leads to two independent objective functions, defined as the sound matching between real part, J_{Re} and imaginary part, J_{Im}. Such objectives are both function of 42 parameters: the real and the imaginary part of $\tilde{\chi}$ for the 21 frequencies studied.

To define the difference between two functions we used the concept of L^p-norm. This application is rather diffuse and permits to obtain an accurate matching between two functions, taking in account both local differences and the overall shape of the functions (Diez and Iemma, 2011).

The L^p-norm for the function f is defined as:

$$\|f\|_p = \|f\|_{L_p} = \left[\frac{1}{\mu(\mathcal{D})}\int_{\mathcal{D}} |f|^p \mathrm{d}\mathcal{D}\right]^{\frac{1}{p}}, \qquad \text{with } p \geq 1, \tag{4.34}$$

where the term $1/\mu(\mathcal{D})$ represents the normalization with respect to the measure of the domain $\mathcal{D}$. A useful property of the L^p-norm is that satisfy the following condition:

$$\|f\|_\infty = \lim_{x\to\infty} \|f\|_p = \lim_{x\to\infty} \left[\frac{1}{\mu(\mathcal{D})}\int_{\mathcal{D}} |f|^p \mathrm{d}\mathcal{D}\right]^{\frac{1}{p}} = \max\{|f|\}. \tag{4.35}$$

Defining the difference between two function f and g from equation (4.34), we obtain:

$$\|f-g\|_p = \left[\frac{1}{\mu(\mathcal{D})}\int_{\mathcal{D}} |f-g|^p \mathrm{d}\mathcal{D}\right]^{\frac{1}{p}}. \tag{4.36}$$

Equation (4.36) define the difference between two arbitrary functions depending on the order p. The value of p governs the "dimension" of the significative differences between the function f and g: increasing the value of p will give more importance to local differences.

Since we are interested to match the overall shape of the signals, we chose a value of $p = 2$. As the integration is performed in the frequency domain, we approximated the operation with a summation over the values of ν. The two objective function were defined as:

$$\begin{aligned} J_{Re} &= \left[\frac{1}{\mu}\int_{\nu_{min}}^{\nu_{max}} \left|\mathrm{Re}\left(\tilde{p}_E^M(\nu) - \tilde{p}_O^M(\nu)\right)\right|^2 \mathrm{d}\nu\right]^{\frac{1}{2}} \qquad (4.37)\\ &\simeq \left[\frac{1}{\mu}\sum_k \left|\mathrm{Re}\left(\tilde{p}_E^M(\nu_k) - \tilde{p}_O^M(\nu_k)\right)\right|^2 \Delta\nu\right]^{\frac{1}{2}} \\ &= \left[\frac{1}{\mu}\sum_k \left|\mathrm{Re}\left(\tilde{p}_E^M(\nu_k)\right) - 2\left[\mathrm{Re}(H)\mathrm{Re}(\tilde{\chi_k}) - \mathrm{Im}(H)\mathrm{Im}(\tilde{\chi_k})\right]\right|^2 \Delta\nu\right]^{\frac{1}{2}}, \end{aligned}$$

and

$$\begin{aligned} J_{Im} &= \left[\frac{1}{\mu}\int_{\nu_{min}}^{\nu_{max}} \left|\mathrm{Im}\left(\tilde{p}_E^M(\nu) - \tilde{p}_O^M(\nu)\right)\right|^2 \mathrm{d}\nu\right]^{\frac{1}{2}} \qquad (4.38)\\ &\simeq \left[\frac{1}{\mu}\sum_k \left|\mathrm{Im}\left(\tilde{p}_E^M(\nu_k) - \tilde{p}_O^M(\nu_k)\right)\right|^2 \Delta\nu\right]^{\frac{1}{2}} \end{aligned}$$

$$= \left[\frac{1}{\mu}\sum_{k}\left|\mathrm{Im}\left(\tilde{p}_E^M(\nu_k)\right) - 2\left[\mathrm{Im}(H)\mathrm{Re}(\tilde{\chi_k}) + \mathrm{Re}(H)\mathrm{Im}(\tilde{\chi_k})\right]\right|^2 \Delta\nu\right]^{\frac{1}{2}},$$

where $\mu = \nu_{max} - \nu_{min}$, $\Delta\nu = 0.5$ Hz and the summation runs over the 21 values of frequency from 0 to 10 Hz with a uniform step $\Delta\nu$. Both J_{Re} and J_{Im} are function of 42 variables represented by real and imaginary parts of $\tilde{\chi}$ for the complete set of frequencies.

Performing an AWS optimization for the three cases of study described in subsection 4.3.2, we obtained the optimal solution from the Pareto front.

Chapter 5

Results

5.1 Analytical solution

Solving the linear system (4.24) it was possible to find the real and imaginary part of the normal derivative of pressure $\tilde{\chi}$ on source panels. Table 5.1 shows the values obtained for the case with no acoustic propagation in the volcanic conduit. Power spectrum in SPL for the obtained $\tilde{\chi}$ is shown in Figure 5.1. Peak frequencies occur between 4 and 6 Hz, similarly to the pressure signal recorded at the microphone.

Normal acceleration a_n and velocity v_n directed outside the source panels can be obtained from Bernoulli's theorem:

$$\tilde{p} = -i\omega\rho\tilde{\varphi}, \tag{5.1}$$

considering that:

$$\tilde{\chi} = \frac{\partial\tilde{p}}{\partial n} = \frac{\partial}{\partial n}\left[-i\omega\rho\ \tilde{\varphi}\right] = -i\omega\rho\frac{\partial\tilde{\varphi}}{\partial n} = -i\omega\nabla\tilde{\varphi}\cdot\hat{n} = -i\omega\rho\ \vec{v}\cdot\hat{n}. \tag{5.2}$$

Since in the Fourier space, the derivative operation reduces to the product for a factor $(i\omega)$, normal acceleration $\tilde{a}_n$ and velocity $\tilde{v}_n$ in the frequency domain can be obtained as:

$$\tilde{a}_n = -\frac{1}{\rho}\tilde{\chi}, \tag{5.3}$$

and

$$\tilde{v}_n = -\frac{1}{i\omega\rho}\tilde{\chi}. \tag{5.4}$$

By an inverse Fourier transform, it was possible to obtain the time series of a_n and v_n. Figures 5.2-5.3 illustrate the normal acceleration and velocity obtained for the case with no volcanic conduit.

	Source depth 0 m	
ν **(Hz)**	**Re**$(\tilde{\chi})$	**Im**$(\tilde{\chi})$
0.0	-3890.57	0.00
0.5	969.22	755.77
1.0	-48.44	-710.02
1.5	-207.43	-397.54
2.0	-441.10	-630.25
2.5	-716.72	-311.87
3.0	-648.90	83.51
3.5	-464.63	780.08
4.0	426.13	829.18
4.5	725.01	378.50
5.0	538.00	-197.63
5.5	385.04	-446.99
6.0	117.35	-582.09
6.5	-277.94	-339.22
7.0	-294.46	-78.29
7.5	-125.87	105.38
8.0	-64.48	120.51
8.5	-44.54	140.53
9.0	14.42	174.00
9.5	70.33	65.96
10.0	89.79	13.68

Table 5.1: Real and imaginary part of normal derivative of pressure $\tilde{\chi}$ obtained by equation (4.24) as a function of frequency, for the case with no volcanic conduit.

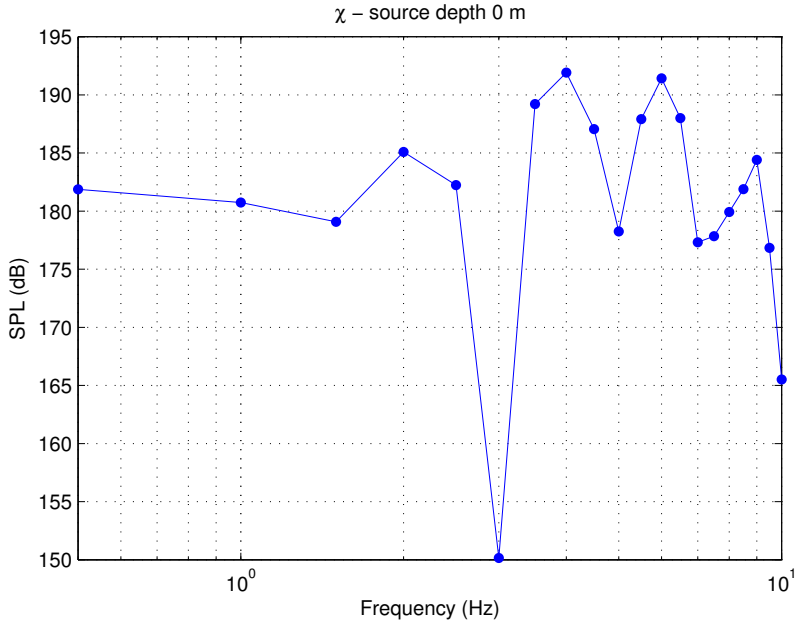

Figure 5.1: Power spectrum (SPL) of $\tilde{\chi}(\omega)$ for a source depth of 0 m.

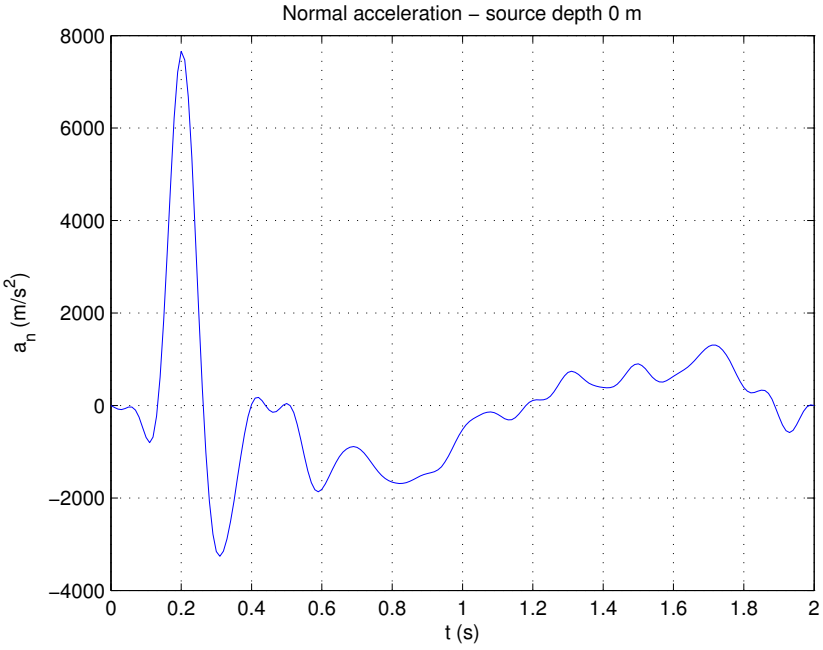

Figure 5.2: Normal acceleration on the radiating panels. Source depth 0 m.

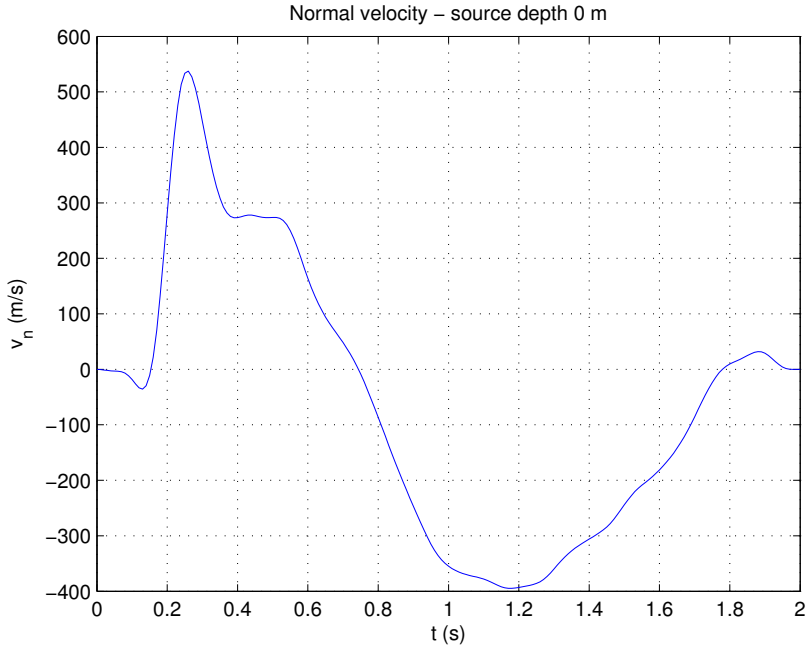

Figure 5.3: Normal velocity on the radiating panels. Source depth 0 m.

Physical interpretation

Figure 5.2 shows the normal acceleration on the source panels (*i.e.* at the volcanic vent) obtained by solving the problem for a source depth of 0 m. As it can be supposed for a strombolian explosion, the event reveals extremely impulsive, with a high amplitude signal concentrated in a time lapse of 0.2 s.

The acoustic normal velocity time series for the same event is illustrated in Figure 5.3. Also for v_n the shape is rather impulsive, with a rapid increase to a maximum value, followed by a slow decay. Normal velocity peaks at a value of about 540 m s^{-1}. Such a result seems to reveal a supersonic velocity. Nevertheless, considering that the air on the acoustic source is probably hot or, at least, far from the standard conditions (remember that beneath our acoustic source there are many complex fluid dynamic processes), sound speed is reasonably higher than 340 m s^{-1}. Moreover taking into account the assumptions made in the previous chapter, acoustic signal may have been generated inside the magmatic body, where the sound speed can reach values more than twice compared to its value in free air (Buckingham and Garcés, 1996; Garcés, 1997); anyway, the actual value of c remains unknown in the gas-magma mixture, since it depends on many thermodynamic and rheological properties (Murase and McBirney, 1973; Kieffer, 1977).

Furthermore, the normal velocities v_n has to be considered as *acoustic velocities* associated to the transit of the acoustic wave. In this view, these velocities does not directly represent the actual velocity of the gas-magma mixture. As a matter of fact the acoustic source was placed at a depth such that the acoustic propagation was completely decoupled from the fluid motion. Any information about the fluid motion had to be investigated at a higher depth beneath our acoustic source, but this method does not permits it. Further investigations on fluid dynamics on the basis of our boundary conditions could be topic for future works.

5.2 Optimization

Figure 5.4 shows the Pareto front obtained by the AWS method for the objective functions (4.37) and (4.38) in the case with no volcanic conduit. As one can see, Pareto front shows the typical almost-hyperbolic shape, with limit values rather low. This seems a good result and make us confident about the method, since the objective functions have to reach a value as most as possible near to zero. The precision of course depends on the features of the minimization tool. We used a minimization function of the commercial software MATLAB that demonstrates valid to find the first points, but pretty slow during the sub-optimization. This is the reason for a non-uniformly sampled Pareto front. Nevertheless, the high curvature zone of the Pareto front (the hyperbola vertex), is sufficiently dense to make us confident about the results.

Figure 5.5 shows the normal accelerations obtained from all points of the Pareto front of Figure 5.4. The points in the high-curvature region (where the objective functions assumes similar weights) provides for a_n shapes similar to that obtained from the linear system (4.24).

To compare the results from the optimization with that obtained by solving equation (4.24), we choose as *optimal* solution the one having the higher congruency with the values shown in Table 5.1. The congruency criterion was defined as:

$$\min \sum |\tilde{\chi}_{LS} - \tilde{\chi}_{OPT}|^2, \tag{5.5}$$

where $\tilde{\chi}_{LS}$ represents the values of real and imaginary part of $\tilde{\chi}$ of Table 5.1, joined in a 42-element array, and the sum runs over the entire set of Pareto points.

Table 5.2 shows the optimal values for $\mathrm{Re}(\tilde{\chi})$ and $\mathrm{Im}(\tilde{\chi})$ obtained by the congruency criterion (5.5). Figure 5.6 illustrates graphically the congruency between $\mathrm{Re}(\tilde{\chi})$ and $\mathrm{Im}(\tilde{\chi})$ as function of frequency obtained by the two methods. The agreement is remarkable.

Figure 5.7 illustrates the time series of normal acceleration for the optimal Pareto solution obtained by the criterion (5.5) superimposed to the

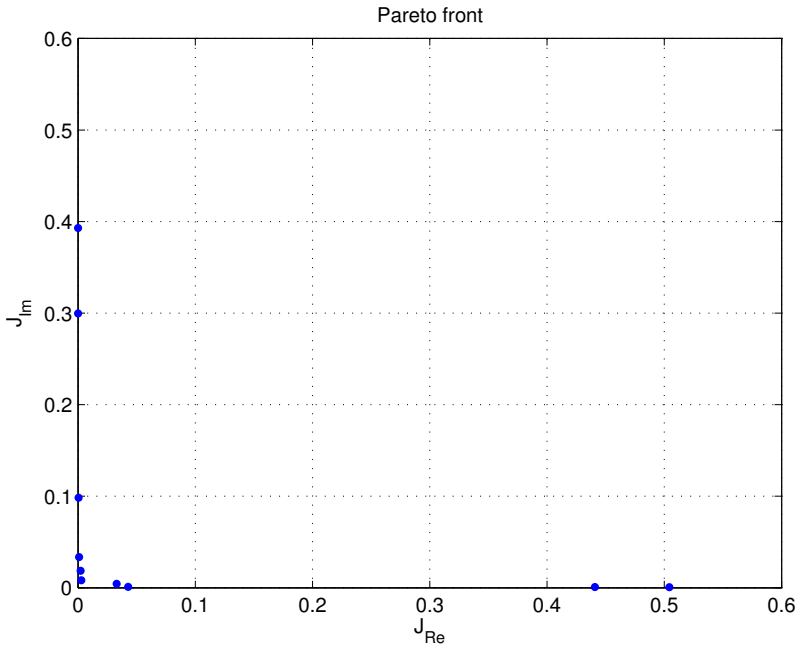

Figure 5.4: Pareto front obtained by the AWS optimization. Source depth 0 m.

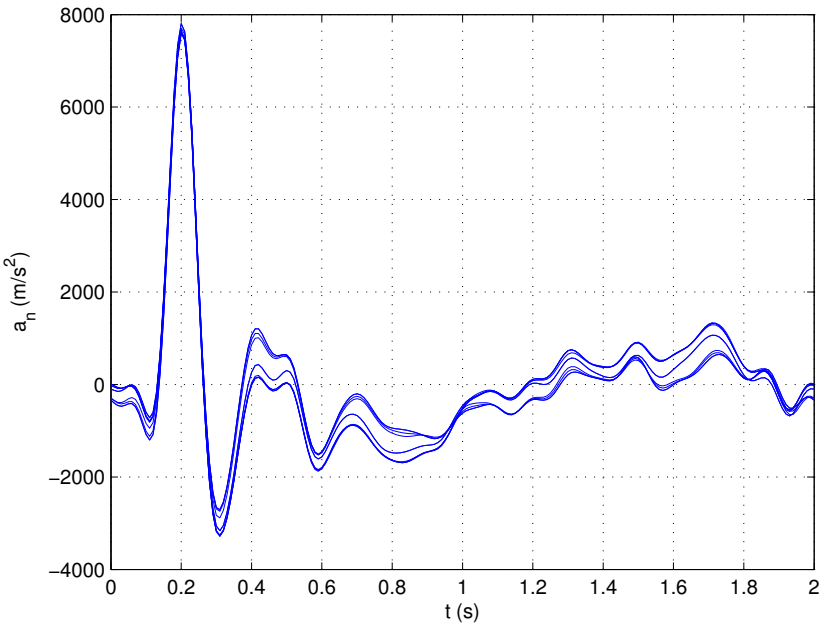

Figure 5.5: Normal accelerations obtained from each point of the Pareto front of Figure 5.4. Source depth 0 m.

time series of a_n of Figure 5.2, solution of the equation (4.24).

The perfect congruency between the results obtained from the two methodologies make us confident about the potentialities of the optimization in solving such inversion problem. If we will introduce any improvement in the future, as a better geometry with no symmetries, the possibility to solve a linear system like (4.24) and obtain a unique solution could vanish. In such a condition, we can confidently use the optimization to extract the "optimal" boundary conditions of the problem.

	Source depth 0 m	
ν **(Hz)**	$\mathbf{Re}(\tilde{\chi})$	$\mathbf{Im}(\tilde{\chi})$
0.0	-3685.21	10^{-12}
0.5	959.66	757.61
1.0	-47.40	-709.15
1.5	-205.77	-396.73
2.0	-439.34	-629.70
2.5	-720.96	-309.33
3.0	-651.87	86.93
3.5	-465.01	775.92
4.0	428.16	831.22
4.5	728.33	380.57
5.0	540.09	-198.15
5.5	381.11	-443.71
6.0	114.33	-576.16
6.5	-277.75	-338.59
7.0	-293.97	-77.69
7.5	-126.44	105.37
8.0	-65.99	121.34
8.5	-43.99	139.83
9.0	13.98	176.15
9.5	69.48	64.47
10.0	90.31	13.91

Table 5.2: Optimal real and imaginary part of normal derivative of pressure $\tilde{\chi}$ as a function of frequency obtained by the criterion (5.5), for the case with no volcanic conduit.

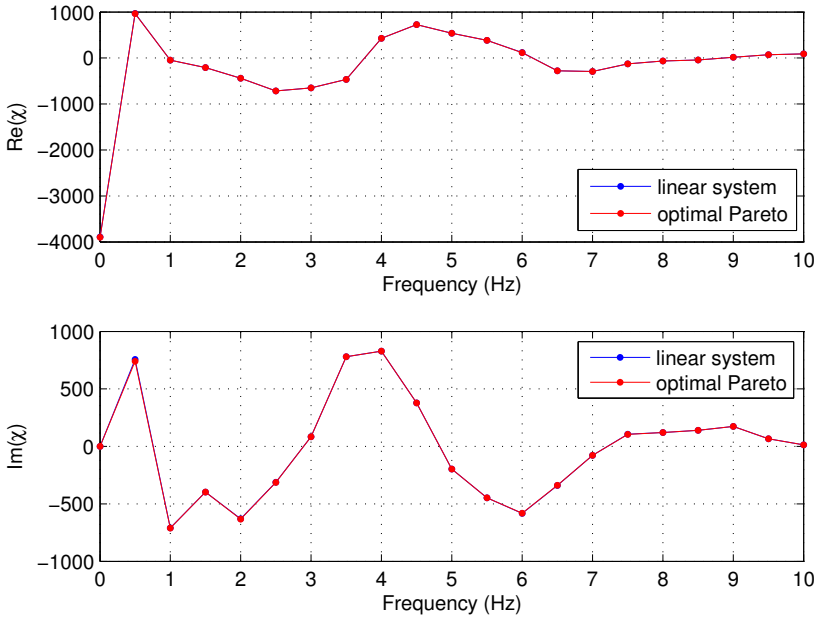

Figure 5.6: Matching of $\mathrm{Re}(\tilde{\chi})$ and $\mathrm{Im}(\tilde{\chi})$ between the two methodologies: linear system (blue) and AWS optimization (red). Source depth 0 m.

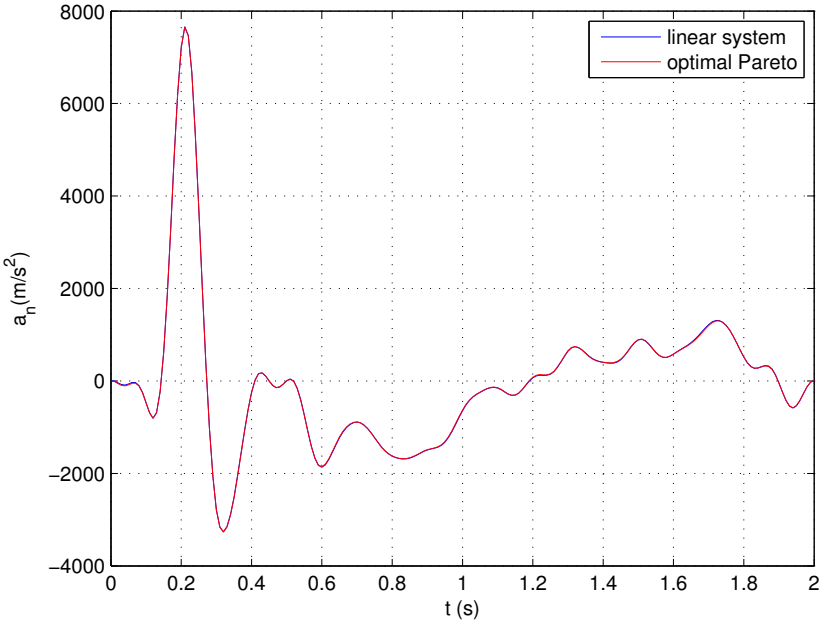

Figure 5.7: Matching of normal accelerations on source panels between the two methodologies: linear system (blue) and AWS optimization (red). Source depth 0 m.

5.3 Validation of the model

In order to check the reliability of our inversion, we made a validation with the commercial software COMSOL. COMSOL is a solver for PDEs and integral equations based on a FEM. The field of physical applications for the solver is rather wide, however in order to maintain the same approximations made using AcouSTO we considered only the *Acoustics Module* of COMSOL, studying the problem in the time domain.

We imposed the boundary conditions obtained by the inversion as input values for COMSOL, propagating the acoustic field in the surrounding space, and recording the pressure signal at a microphone placed in the approximated position of the actual sensor PZZ at Stromboli. If our boundary conditions are correct, pressure signal measured at the microphone have to look like the actual recorded at Stromboli (Figure 4.4).

The same 3D geometry studied with AcouSTO (Figure 4.6) was built in COMSOL, taking advantage of the axial symmetry. With respect to the BEM where only the surfaces are meshed to solve the integrals, the FEM builds the entire mesh of the space. Then we considered a "box" in which the volcano surface was defined as "scattering surface" (*Sound Hard Boundary*), whereas on the remaining surfaces to close the box we put "radiation conditions" (*Plane Wave Radiation*), in order to prevent boundary effects. One side was considered as revolution axis to obtain the 3D geometry. Figure 5.8 illustrates the geometry built in COMSOL.

The spatial scale of the mesh has to be smaller than the minimum wavelength used in the analysis. To accurately maintain a ratio 1/10 between the mesh size and λ, we use the finest mesh provided by COMSOL (Figure 5.9).

COMSOL is capable to radiate in the space the acoustic sound generated by a boundary condition. We defined in the same "radiating panels" used in AcouSTO some boundary conditions expressed in terms of normal acceleration a_n as a function of time.

Figure 5.10 illustrates three snapshots of the pressure field propagating around the volcanic vent. The change of slope give rise to a focusing of the acoustic energy in the direction of the microphone. Then, the actual acoustic pressure measured at the station PZZ at Stromboli is higher with respect to that measured in conditions of free propagation. Such results are in agreement with that obtained by Lacanna (2010) using a 2D FDM.

Figure 5.11 shows the shape of the pressure signal recorded at microphone propagating by COMSOL the boundary conditions obtained by our inversion methodology, compared to the actual pressure signal recorded at the sensor PZZ. Figures 5.12 shows the comparison between frequency spectra in SPL of the same signals.

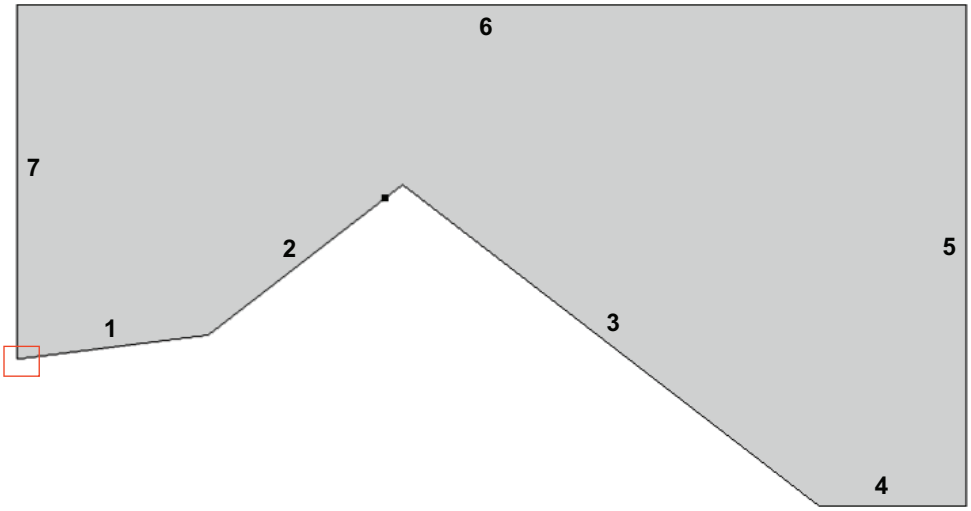

Figure 5.8: Mesh built in COMSOL (gray). Sides 1, 2 and 3 represent the slope of volcano and were defined as *Sound Hard Boundaries*. On sides 4, 5 and 6 we put *Plane Wave Radiation* conditions, in order to propagate radiation outside the mesh without any reflection. Side 7 represents the symmetry axis around which is performed the revolution. Black square represents the microphone. Red rectangle indicates the position of the acoustic source at a depth of 0 m.

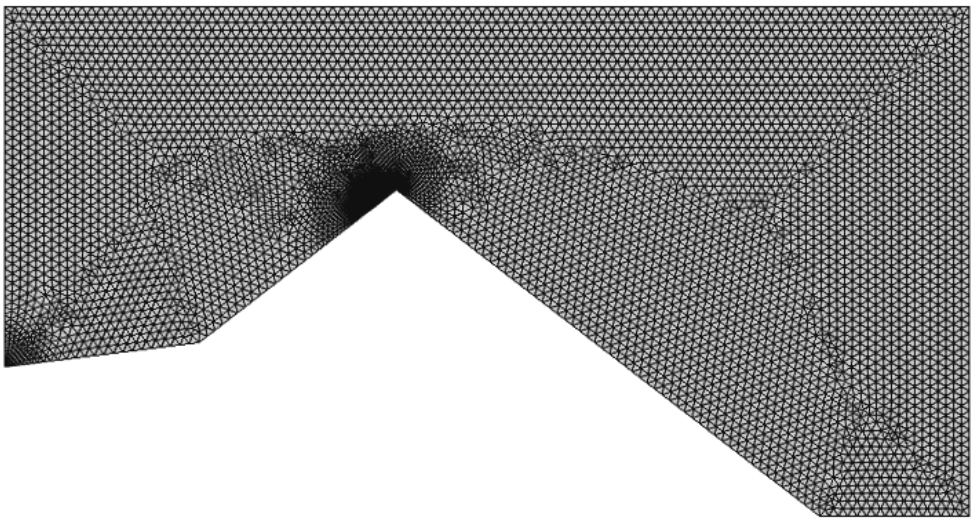

Figure 5.9: Extremely-fine mesh built in COMSOL. Around the vent and the microphone the mesh is finer. Source depth 0 m.

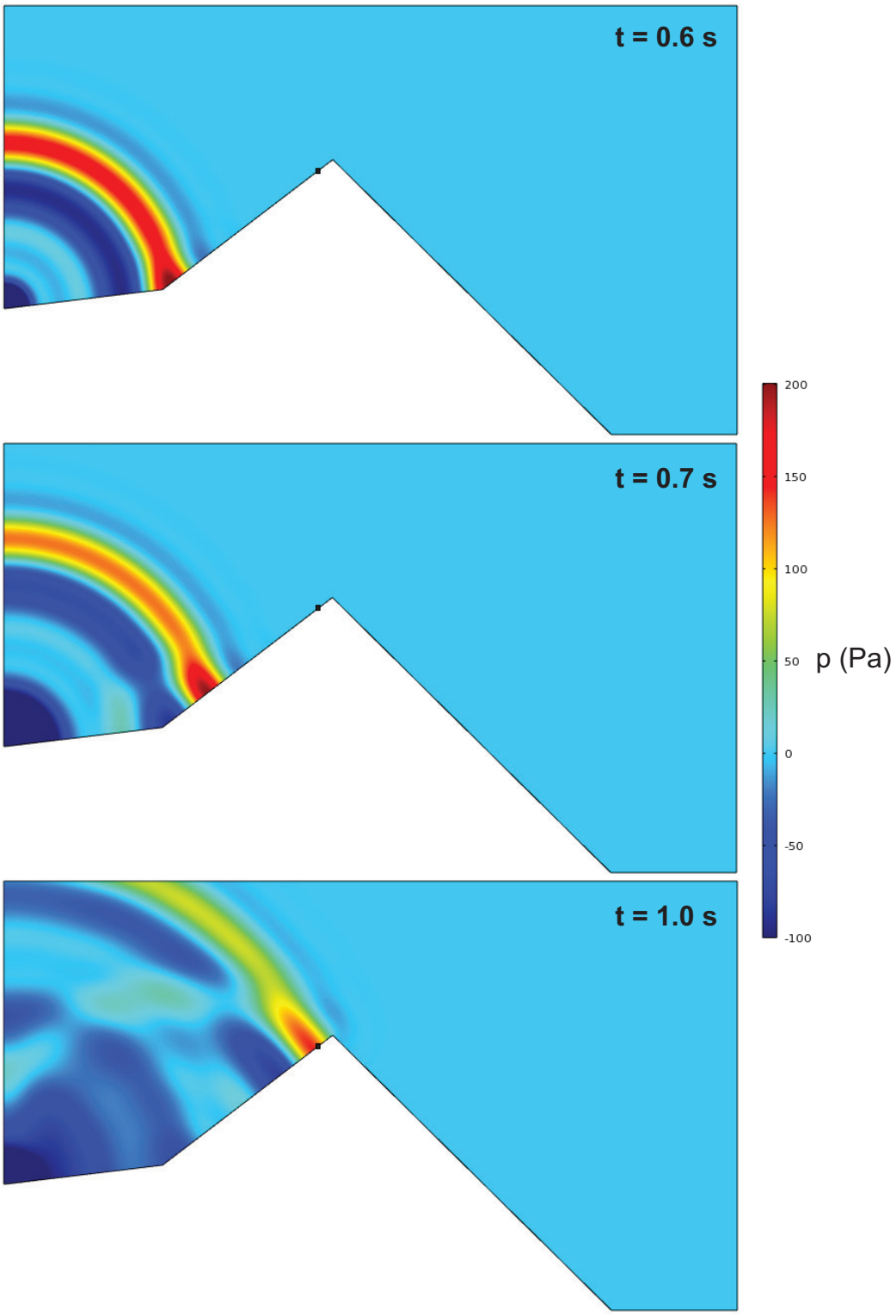

Figure 5.10: Pressure perturbation propagating from volcanic vent. The change in slope causes a focusing of acoustic energy towards the microphone (black square).

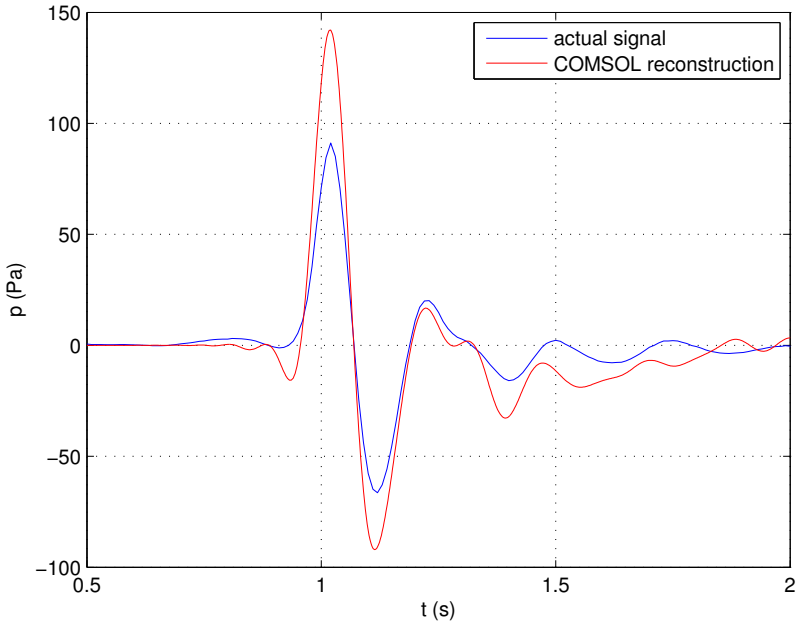

Figure 5.11: Pressure signals recorded by the station PZZ at Stromboli (blue) and calculated by COMSOL radiating the boundary conditions on a_n obtained by our inversion solving the system (4.24). Source depth 0 m.

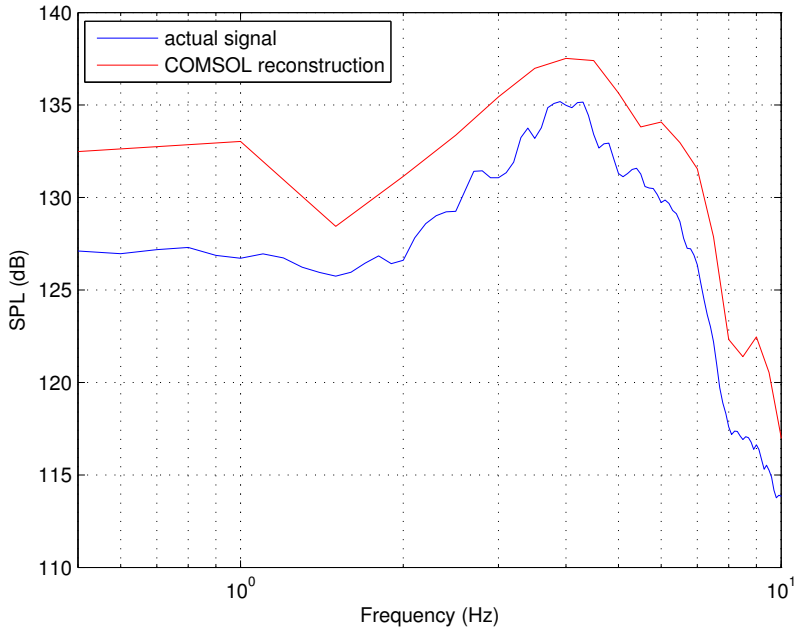

Figure 5.12: Power spectra (SPL) of pressure signals recorded by the station PZZ at Stromboli (blue) and calculated by COMSOL radiating the boundary conditions on a_n obtained by our inversion solving the system (4.24). Source depth 0 m.

From Figure 5.11 is noticeable the good reconstruction of both the main pressure peak and the subsequent secondary pulses. That is a surprising good result, because indicates that the impulsive boundary conditions obtained for $\tilde{\chi}$ (or similarly, for a_n, Figure 5.2) accurately represent source conditions for the actual pressure signal measured at PZZ station at Stromboli. Although the amplitude is higher for the reconstructed signal, the shape (mostly for the main pressure peak) is pretty similar to the actual signal. Also the frequency spectrum (Figure 5.12), despite the higher amplitude and the low number of frequencies, shows a similar frequency content between the two signals.

The mismatch in the amplitude between signals can be addressed both to the approximated geometry, and to a poor convergence in one of the two integral methods used (AcouSTO-BEM and COMSOL-FEM). Any refinement in the mesh could improve the convergence. The use of the actual topography of Stromboli with an almost uniform size of panels could probably provide a higher accuracy in the identification of source conditions.

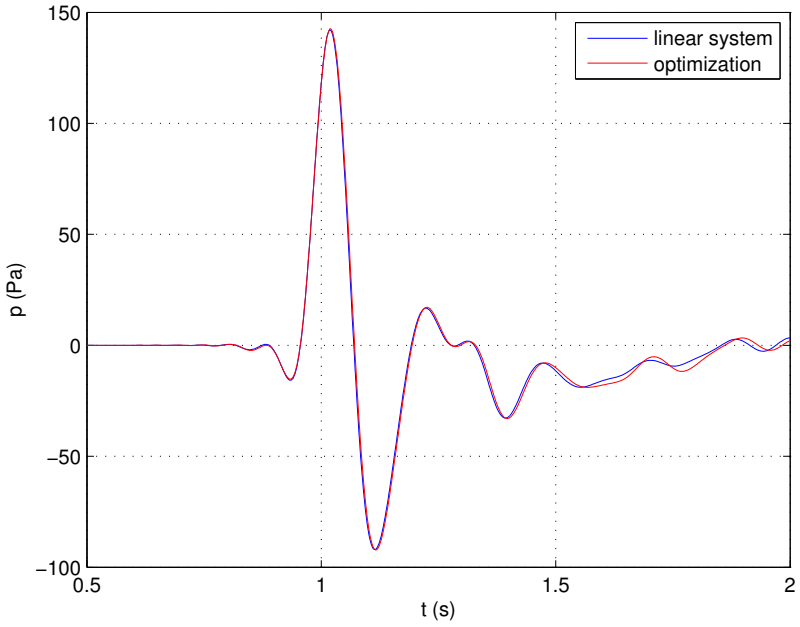

Figure 5.13: Matching between pressure signals at microphone radiating the initial conditions obtained by the linear system (4.24) (blue) and the optimization (red). Source depth 0 m.

A similar result was obtained propagating by COMSOL the optimal boundary conditions of Table 5.2 provided by the AWS optimization. Figure 5.13 shows the good matching between the two methodologies, confirming

the validity of the optimization to find accurate results.

5.4 Acoustic source inside the volcanic conduit

5.4.1 Solutions for $\tilde{\chi}$

Since the inversion provided good results for the case with the acoustic source lying on the volcanic vent, we repeated the entire methodology placing the acoustic source at the bottom of the volcanic conduit. We studied two cases, with conduit depths of 20 and 50 m (Figure 4.6).

Table 5.3 shows the results for $\tilde{\chi}$ obtained solving the linear system (4.24) for the cases with the source placed inside the volcanic conduit.

	Source depth 20 m		Source depth 50 m	
ν **(Hz)**	**Re**$(\tilde{\chi})$	**Im**$(\tilde{\chi})$	**Re**$(\tilde{\chi})$	**Im**$(\tilde{\chi})$
0.0	-4460.90	0.00	-3123.31	0.00
0.5	1143.30	648.07	1032.35	221.15
1.0	-59.88	-571.27	13.59	-261.59
1.5	-31.79	-98.81	19.96	29.09
2.0	-221.36	-336.45	50.34	234.53
2.5	446.89	41.73	210.20	347.79
3.0	-151.74	1.64	378.17	196.85
3.5	-51.01	41.34	371.41	-209.37
4.0	-16.17	-51.11	80.56	-361.91
4.5	-157.38	-100.01	2.97	-23.02
5.0	-256.67	-113.15	171.21	-67.11
5.5	-213.09	152.23	185.89	-222.87
6.0	-93.58	226.30	42.75	-316.09
6.5	112.76	303.40	-200.43	-221.35
7.0	141.77	52.21	-96.37	-29.32
7.5	98.38	-78.28	2.59	-4.03
8.0	73.98	-52.06	-18.15	-42.61
8.5	59.44	-75.74	-30.53	-85.54
9.0	-3.47	-7.87	-67.75	-94.55
9.5	50.37	-12.74	-84.62	-6.60
10.0	-31.58	-6.43	-31.47	7.31

Table 5.3: Real and imaginary part of normal derivative of pressure $\tilde{\chi}$ obtained by equation (4.24) as a function of frequency, for the two cases with the acoustic source at the bottom of the volcanic conduit.

Figures 5.14-5.15 show the power spectra in SPL for $\tilde{\chi}$ in the two cases

with the acoustic source inside the volcanic conduit. Normal accelerations a_n are shown in Figures 5.16-5.17.

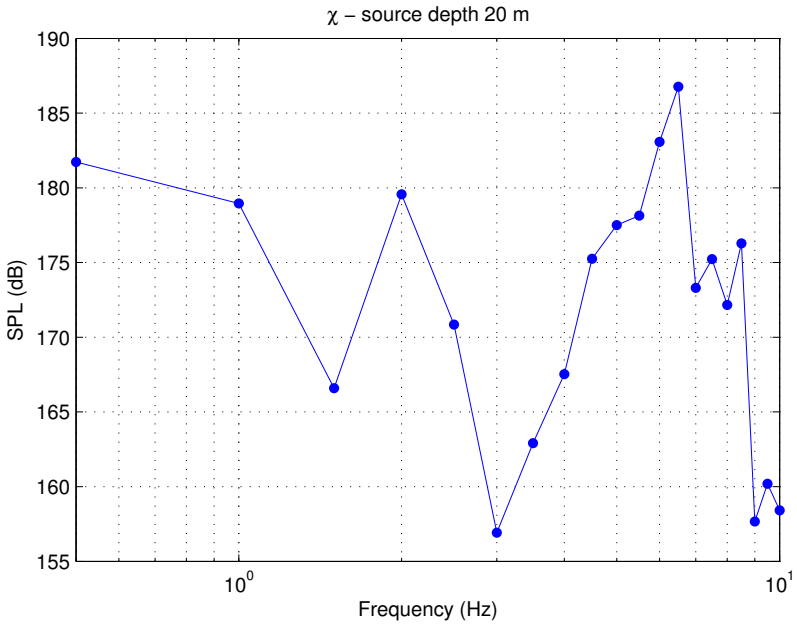

Figure 5.14: Power spectrum (SPL) of $\tilde{\chi}(\omega)$ for a source depth of 20 m.

Figures 5.16 and 5.17 show the normal acceleration on source panels for the cases with a source embedded inside the volcanic conduit, at a depth of 20 and 50 m. Both Figures show two interesting features, different with respect to Figure 5.2:

- the time series of a_n has an initial offset;
- there are some high-amplitude oscillations.

Such a result seems a little bit strange since an oscillating source has to generate at the microphone an impulsive signal, with an initial high-amplitude oscillation followed by secondary oscillations with lower amplitude. Any problems connected to this features of normal accelerations a_n are highlighted by the validation made by COMSOL.

Figures 5.18-5.19 shows the Pareto fronts obtained by the AWS method for the objective functions 4.37 and 4.38 for the two cases with the acoustic source placed inside the volcanic conduit. Like Figure 5.4, Pareto fronts show the typical almost-hyperbolic shape, with limit values rather low.

Table 5.4 shows the optimal values for $\mathrm{Re}(\tilde{\chi})$ and $\mathrm{Im}(\tilde{\chi})$ obtained by the congruency criterion (5.5) for the cases with volcanic conduit. Figures 5.20-5.21 illustrate graphically the congruency between $\mathrm{Re}(\tilde{\chi})$ and $\mathrm{Im}(\tilde{\chi})$ as

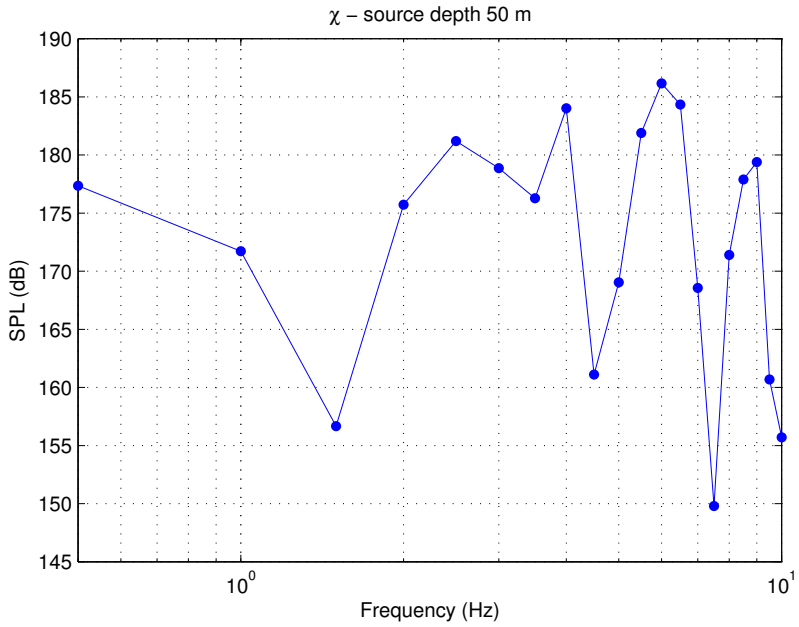

Figure 5.15: Power spectrum (SPL) of $\tilde{\chi}(\omega)$ for a source depth of 50 m.

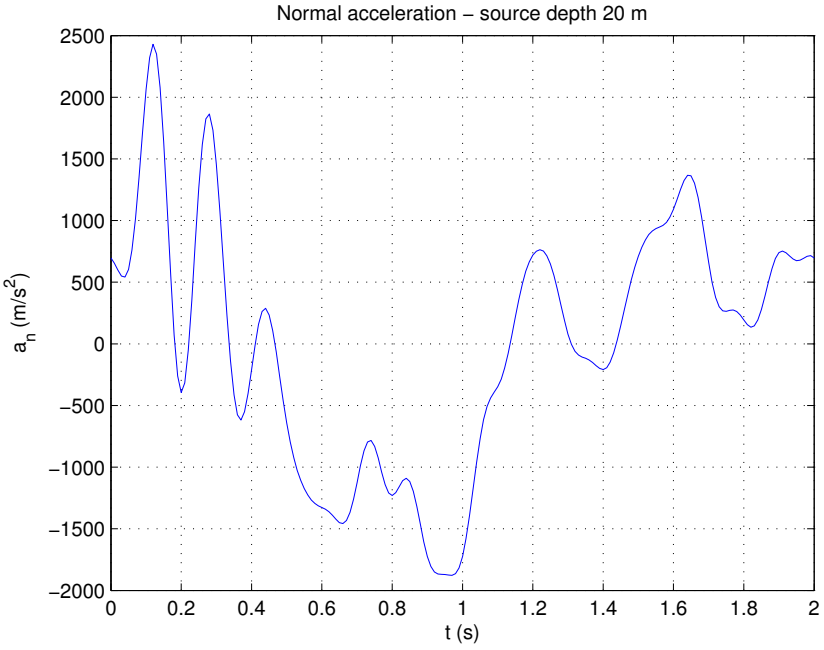

Figure 5.16: Normal acceleration on the radiating panels. Source depth 20 m.

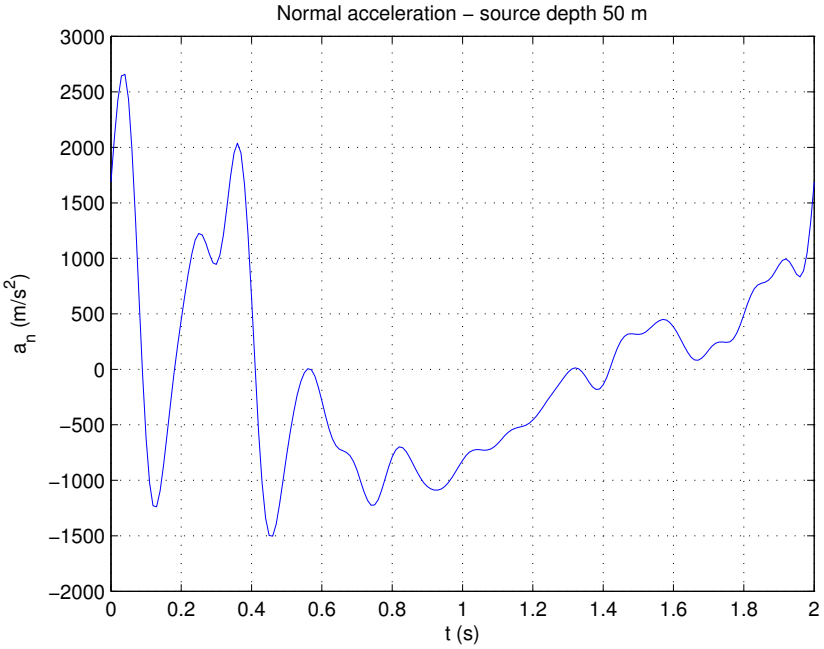

Figure 5.17: Normal acceleration on the radiating panels. Source depth 50 m.

function of frequency obtained by the two methods. Also for the cases with acoustic source placed at the bottom of volcanic conduit the agreement is remarkable.

Figures 5.22-5.23 illustrate the time series of normal acceleration for the optimal Pareto solution obtained by the criterion (5.5) superimposed to the time series of a_n of Figures 5.16-5.17, solution of the equation (4.24). Also for these cases the congruency is remarkable.

The agreement between the two methods occurs in all the three cases of study. This indicate that the strange oscillating character of a_n (or χ) for an acoustic source embedded in the volcanic conduit represent the real solution of the problem. The validation of our methodology helped us in the interpretation of such results.

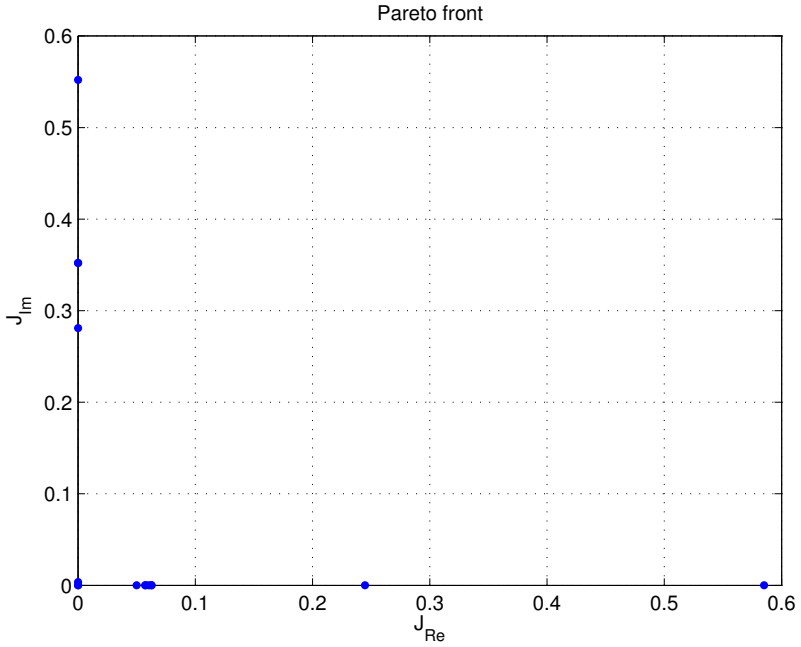

Figure 5.18: Pareto front obtained by the AWS optimization. Source depth 20 m.

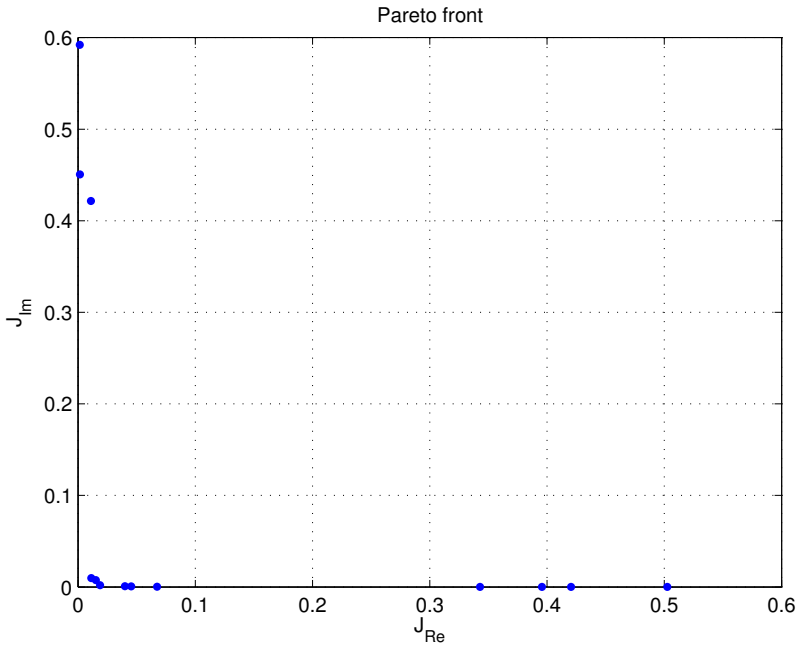

Figure 5.19: Pareto front obtained by the AWS optimization. Source depth 50 m.

	Source depth 20 m		Source depth 50 m	
ν **(Hz)**	$\mathbf{Re}(\tilde{\chi})$	$\mathbf{Im}(\tilde{\chi})$	$\mathbf{Re}(\tilde{\chi})$	$\mathbf{Im}(\tilde{\chi})$
0.0	-4460.90	-10^{-13}	-4378.41	0.00
0.5	1143.30	648.07	1040.20	217.98
1.0	-59.88	-571.27	13.62	-262.00
1.5	-31.79	-98.81	19.97	29.03
2.0	-221.36	-336.45	50.11	235.09
2.5	446.87	41.73	210.89	348.00
3.0	-151.74	1.64	378.02	196.32
3.5	-51.01	41.34	371.35	-210.11
4.0	-16.17	-51.11	80.49	-362.23
4.5	-157.38	-100.01	2.98	-23.00
5.0	-256.67	-113.15	170.95	-66.87
5.5	-213.09	152.23	186.30	-223.75
6.0	-93.58	226.30	43.04	-316.91
6.5	112.76	303.40	-200.21	-220.81
7.0	141.77	52.21	-96.16	-29.18
7.5	98.38	-78.28	2.60	-4.04
8.0	73.98	-52.06	-18.34	-42.17
8.5	-3.47	-7.87	-30.21	-85.46
9.0	59.44	-75.74	-66.93	-95.44
9.5	50.37	-12.74	-85.56	-6.88
10.0	-31.58	-6.43	-31.47	7.31

Table 5.4: Optimal real and imaginary part of normal derivative of pressure $\tilde{\chi}$ as a function of frequency obtained by the criterion (5.5), for the two cases with volcanic conduit.

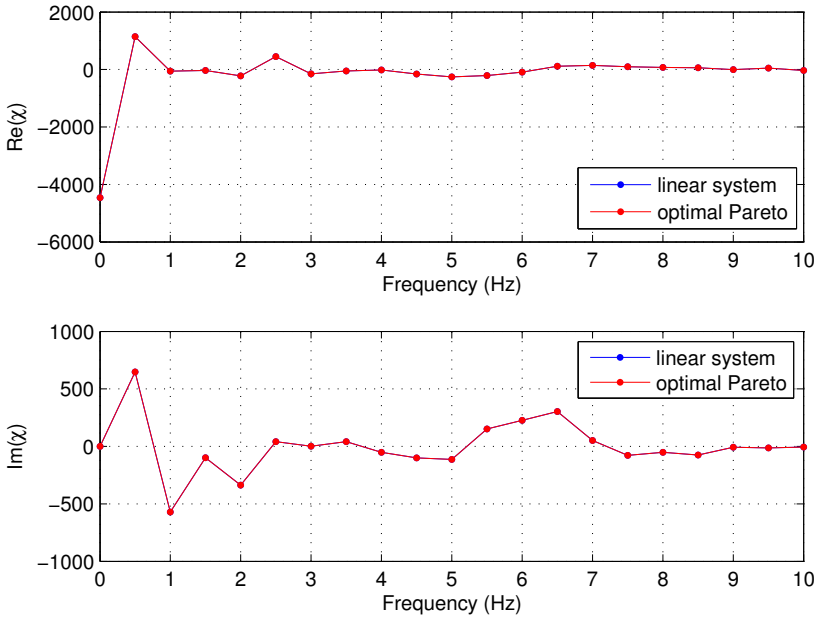

Figure 5.20: Matching of $\mathrm{Re}(\tilde{\chi})$ and $\mathrm{Im}(\tilde{\chi})$ between the two methodologies: linear system (blue) and AWS optimization (red). Source depth 20 m.

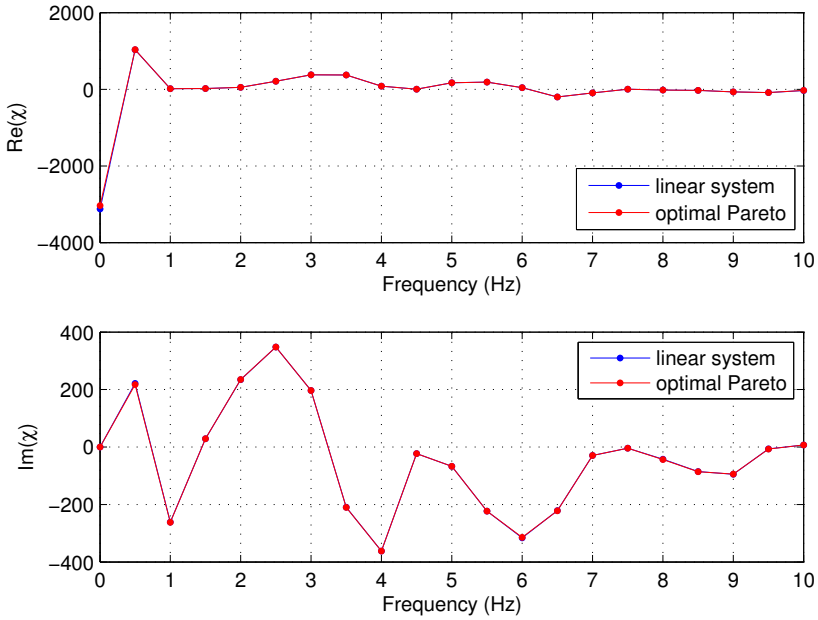

Figure 5.21: Matching of $\mathrm{Re}(\tilde{\chi})$ and $\mathrm{Im}(\tilde{\chi})$ between the two methodologies: linear system (blue) and AWS optimization (red). Source depth 50 m.

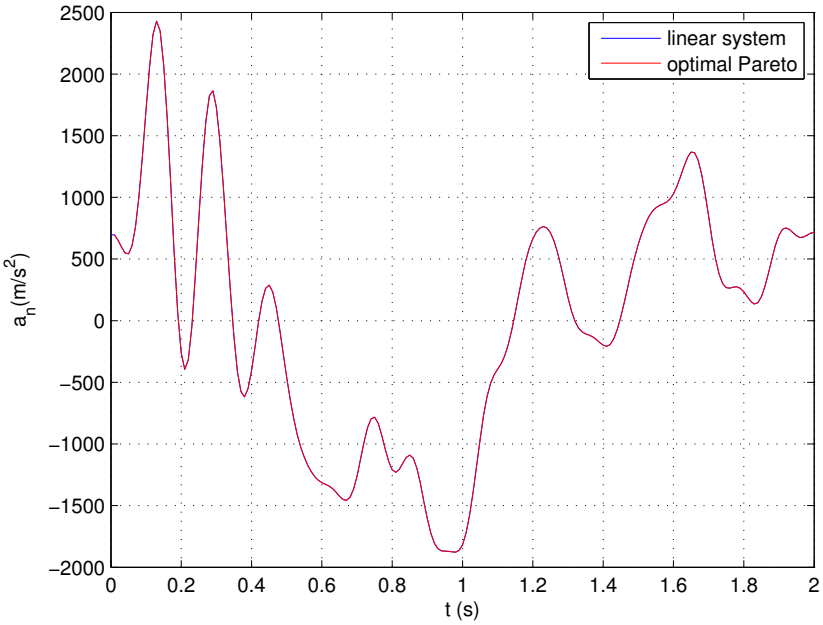

Figure 5.22: Matching of normal accelerations on source panels between the two methodologies: linear system (blue) and AWS optimization (red). Source depth 20 m.

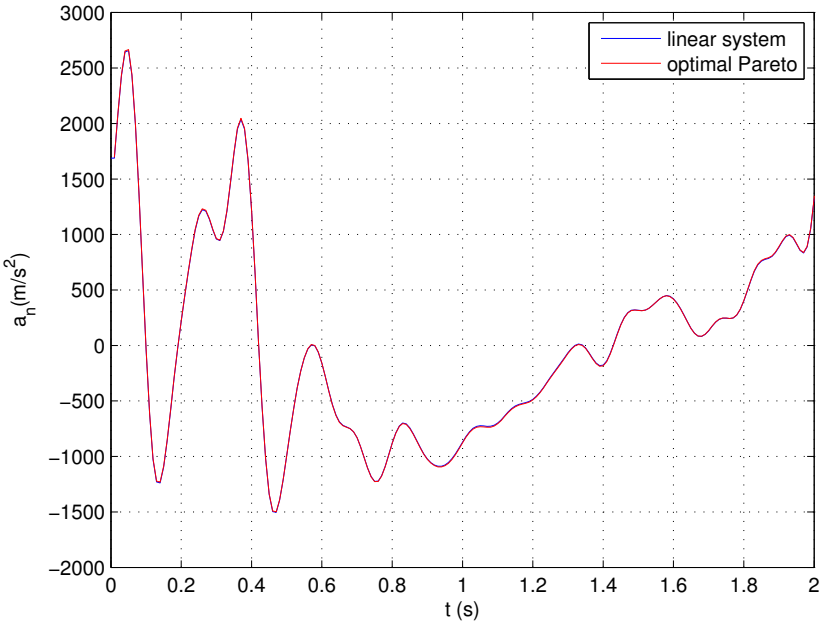

Figure 5.23: Matching of normal accelerations on source panels between the two methodologies: linear system (blue) and AWS optimization (red). Source depth 50 m.

5.4.2 Validation for the cases with volcanic conduit

The same validation made for the case with the the acoustic source at the vent level was made also for results obtained with the acoustic source placed at the bottom of the volcanic conduit. Figures 5.24-5.25 show the comparison between the pressure signals recorded at microphone propagating by COMSOL the boundary conditions obtained by our inversion methodology, and the actual pressure signal recorded at the sensor PZZ.

In both the two cases (source at a depth of 20 and 50 m inside the volcanic conduit), the shape of the main pulse is still reconstructed with a pretty good accuracy, but instead of having a decay, there are several high amplitude oscillations. Such a result seems to suggest that the methodology does not work accurately in these conditions.

Since the case with the acoustic source at the top of conduit works well, we can confidently state that the weakness of our method lies in the volcanic conduit, identifying two possible causes for the problem:

1. A significative problem could lie in the thin panels that make up the mesh of the tube: since we are representing the circular section of the volcanic conduit having a radius of 2 m with a polygonal line composed of 512 segments, each segment has a length of about 2.45 cm. As long as the vertical length of the panels along the tube is 3.4 m ($\lambda/10$), volcanic conduit is composed by many thin panels with one side about 10^2 times smaller than the other (Figure 5.26). This of course could give rise to errors during the integral calculation made by AcouSTO.

2. The second cause could be addressed to the nonlinearities associated to the propagation inside the tube. Maybe the linear acoustic source can not be placed inside the conduit, regardless the geometry of the mesh, because nonlinear effects are too high.

A refinement of the mesh inside the volcanic conduit could put some insight to the actual problem at the base of our results, checking the possibility to put the acoustic source inside the conduit, if nonlinear effects are neglectable.

Similar results were obtained propagating by COMSOL the optimal boundary conditions of Table 5.4 provided by the AWS optimization. Figures 5.27-5.28 show the good matching between the two methodologies, confirming the validity of the optimization to find accurate results.

Despite the problems encountered putting the acoustic source inside the volcanic conduit, the good agreement between the actual signal and that reconstructed by COMSOL in the first case (no volcanic conduit) makes us confident about the potentiality of the methodology. Since also the optimization provided significative results, it is possible to confidently perform any improvement of the methodology in the future, reproducing accurately the actual features of Stromboli.

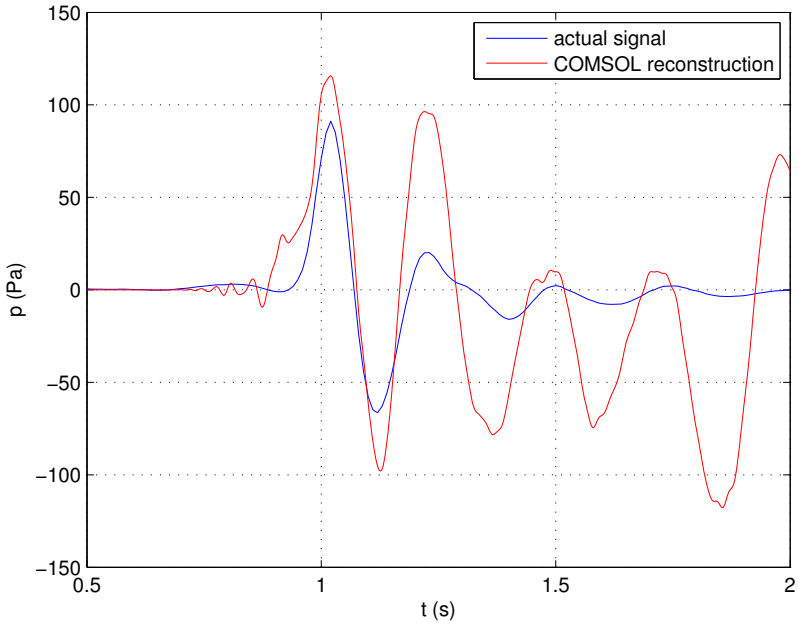

Figure 5.24: Pressure signals recorded by the station PZZ at Stromboli (blue) and calculated by COMSOL radiating the boundary conditions on a_n obtained by our inversion solving the system (4.24). Source depth 20 m.

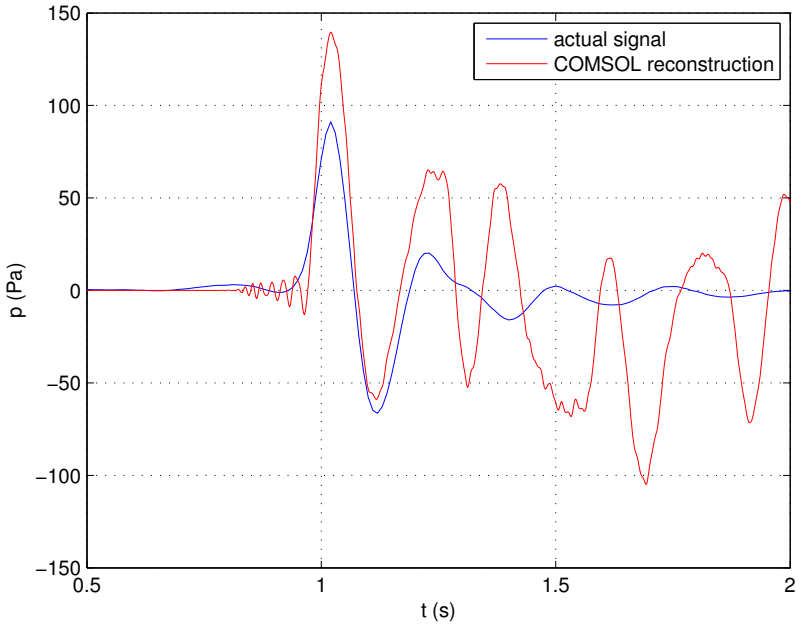

Figure 5.25: Pressure signals recorded by the station PZZ at Stromboli (blue) and calculated by COMSOL radiating the boundary conditions on a_n obtained by our inversion solving the system (4.24). Source depth 50 m.

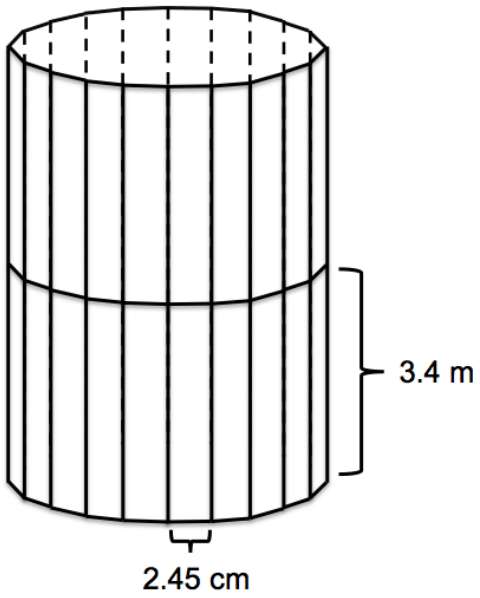

Figure 5.26: Panels inside volcanic conduit have a rectangular shape with sides of 3.4 m and 2.45 cm. Such geometry may have generated problems in the convergence of AcouSTO.

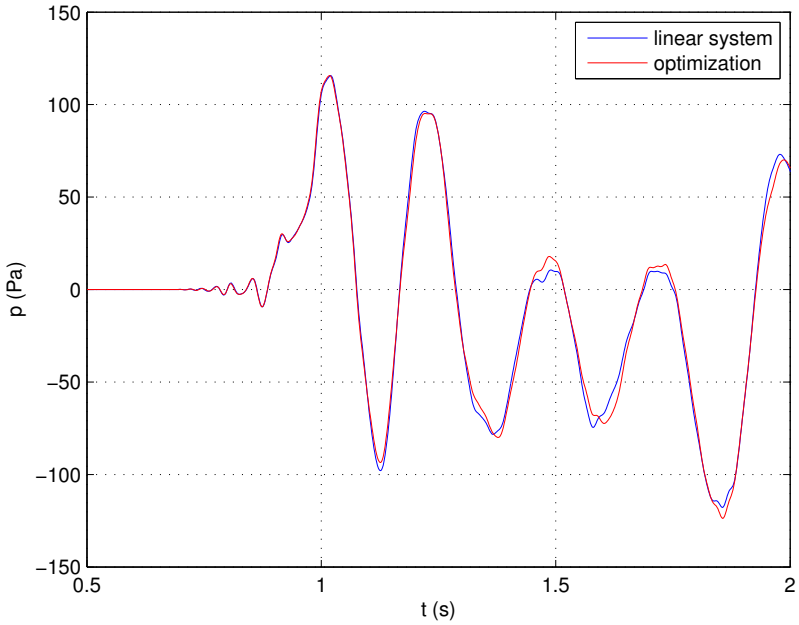

Figure 5.27: Matching between pressure signals at microphone radiating the initial conditions obtained by the linear system (4.24) (blue) and the optimization (red). Source depth 20 m.

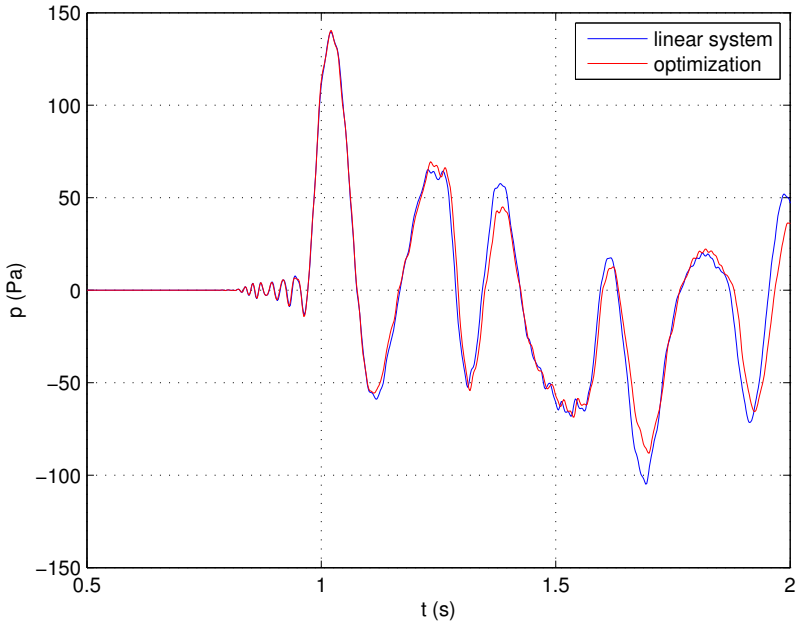

Figure 5.28: Matching between pressure signals at microphone radiating the initial conditions obtained by the linear system (4.24) (blue) and the optimization (red). Source depth 50 m.

Conclusions and future works

In this PhD thesis a critical approach in data analysis and a method for acoustic inversion were presented. The aim of these work was to perform a validity analysis of commonly used formulas to extract physical parameters from infrasonic recordings and to propose a new inversion model for acoustic source characterization from data.

An accurate review of equations relating the infrasonic pressure to gas velocity, based both on theoretical considerations and data analysis, demonstrated that the actual cases of applicability of such equations are rather sparse. All compact source models are defined in an infinite free-space, but the acoustic source during a strombolian eruption can be located at an unknown depth inside volcanic conduit: that makes the use of equations for free-space propagation no more valid.

Dipole model contains two main unknowns: dipole length and angle θ from the axis. Without any information about such quantities, the model results completely ineffective. Equations describing quadrupole are too complicated to enable the extraction of velocity. Just the comparison of power spectrum of the signal with similarity spectrum of jet noise can give an indication for the presence of turbulence as source of sound. Monopole model, although implies many simplifications and a complete symmetry in the explosion, results the more effective model to extract gas velocity during a strombolian explosion. However, also the cases of actual applicability of monopole are few.

In order to extract some information about the acoustic source directly from experimental data, we set up an inversion problem, connecting the pressure recorder at a microphone to the normal derivative of pressure at the source. By means of an BEM, we extracted the transfer matrix containing the effect of acoustic propagation from source panels to the microphone. A simplified geometry of Stromboli volcano was used to reduce the computing power required for the simulations.

Source conditions were extracted from the inverse problem by two different methods: an analytical solution provided by the symmetric geometry, and a generally-valid optimal solution obtained performing an AWS optimization. Thanks to this peculiarity of the problem, we were able to test the accuracy of the optimization in the achievement of the actual solution.

The comparison of results obtained by the two methods makes use confident about the validity of the optimization.

A further validation of our methodology was performed by using a FEM, radiating in time domain the source conditions obtained by the inversion. Such validation provided a powerful tool to correctly interpret our results. In the case with no propagation inside the volcanic conduit, the signal reconstructed at microphone by the FEM accurately reproduced the actual pressure signal recorded at Stromboli. Such a result proves the accuracy of our methodology to extract reliable condition on acoustic source. In the other cases, with the source located at the bottom of volcanic conduit, the characterization of the source is less effective. Such a mismatch can be addressed to two possible causes:

1. the acoustic source can not be located inside the conduit because nonlinear effects are too high to enable the use of linear equations;

2. the geometry used to mesh the volcanic conduit does not work correctly, because the dimension of panels does not couple efficiently with the mesh outside the volcanic vent.

Any refinement of the mesh inside the volcanic conduit could put some insight on this problem.

The good matching between the actual pressure signal recorded at Stromboli, and that obtained at the microphone by radiating our source conditions, makes use confident about the inversion methodology. Considering that such a result was obtained using only one experimental data and a simplified geometry, a higher accuracy could be reached. That could provide an accurate determination of the acoustic source conditions, enabling the extraction of new information from infrasonic signals.

On the basis of our results, some improvements of the methodology can be performed, in order to reach a higher accuracy in the acoustic source characterization.

First refinement lies in the use of the actual topography of Stromboli. That could solve definitely the effect of sound propagation, enabling a more accurate study on vent radius. Source depth of course has to be 0 m, since our work demonstrated the goodness of such condition. By using no symmetries, it could be possible to have no analytical solution from the inversion: however, the optimization proved its worth to obtain a reliable solution.

The second improvement is the use of a higher number of frequencies and a lower step $\Delta\nu$, in order to perform a reconstruction of the entire pressure signal in time domain, considering also the secondary oscillations.

A further refinement lies in the use of many experimental data for the inversion. Moreover, the validation performed radiating the boundary conditions obtained by the inversion, can be performed to reconstruct the pressure

signal at many microphones: in such a way, it could be possible to design an optimal distribution of microphones around a volcano, in order to have the better characterization of the acoustic source.

All of these refinement have to be made considering no volcanic conduit. An accurate design of conduit geometry can prove the actual possibility to solve the problem putting the acoustic source at the bottom of the conduit. If such condition can not be satisfied, a more accurate physical model (considering effects of nonlinearities and fluid dynamics) could be performed, to study the back-propagation inside the volcanic conduit of the boundary condition obtained at vent.

A different study, but complementary to the numerical simulations, could be performed carrying out an experiment designed to study the effect of source depth inside a duct. Surrounding the tube end by an array of microphones, and changing the depth of the acoustic source (that could be described by the bursting of a membrane), an investigation on signals features could be performed, checking if pressure signals contains any information about the source depth.

References

Andronico D., Cristaldi A., 2007. *Il parossismo del 23-24 novembre 2007 al Cratere di SE: caratteristiche del deposito di caduta.* Internal report no. UFVG2007/073, INGV, Sezione di Catania, Italy.

Andronico D., Pistolesi M., 2010. *The November 2009 paroxysmal explosions at Stromboli.* J. Volcanol. Geoth. Res. **196**, 120-125.

Antoine N.E., 2004. *Aircraft optimization for minimal environmental impact.* Ph.D. Thesis, Stanford University, Stanford, CA, US.

Barbot B., Lavandier C., Cheminèe P., 2008. *Perceptual representation of aircraft sounds.* Appl. Acoust. **69** (11), 1003-1016.

Barsotti S., Neri A., Scire J.S., 2008. *The VOL-CALPUFF model for atmospheric ash dispersal: 1. Approach and physical formulation.* J. Geophys. Res. **113** (B3), 1-12. doi: 10.1029/2006JB004623.

Bass H.E., Bauer H.J., Evans L.B., 1972. *Atmospheric absorption of Sound: Analytical expressions.* J. Acoust. Soc. Am. **52** (3B), 821-825.

Blackburn E.A., Wilson L., Sparks R.S.J., 1976. *Mechanisms and dynamics of strombolian activity.* J. Geol. Soc. Lond. **132**, 429-440.

Bonadonna C., Connor C.B., Houghton B.F., Connor L., Byrne M., Laing A., Hincks T.K., 2005. *Probabilistic modeling tephra dispersal: Hazard assessment to a multiphase rhyolitic eruption at Tarawera, New Zealand.* J. Geophys. Res. **110** (B3), 1-21. doi:10.1029/2003JB002896.

Braun T., Ripepe M., 1993 *Interaction of seismic and airwaves recorded at Stromboli volcano.* Geophys. Res. Lett. **20** (1), 65-68.

Buckingham M.J., Garcés M.A., 1996. *Canonical model of Volcano acoustics.* J. Geophys. Res., **101**, 8129-8151.

Burton M., Neri M., 2007. *Stato attuale e osservazione dell'Etna 25 novembre 2007.* Internal report, INGV, Sezione di Catania, Italy.

Cannata A., Montalto P., Privitera E., Russo G., Gresta S., 2009. *Tracking eruptive phenomena by infrasound: May 13, 2008 eruption at Mt. Etna*, Geophys. Res. Lett. **36**, L05304, doi:10.1029/2008GL036738.

Caplan-Auerbach J., Bellesiles A., Fernandes J.K., 2010. *Estimates of eruption velocity and plume height from infrasonic recordings of the 2006 eruption of Augustine Volcano, Alaska.* J. Volcanol. Geoth. Res. **189**, 12-18.

Caves B.E., Jenkinson L.R., Rhodes D.P., 1997. *Adapting Civil Aircraft Conceptual Design Methods to Account for Broader Based Constraints.* AIAA Paper 97-5595, in proc. of World Aviation Congress, Anaheim, CA, US.

Costa A., Macedonio G., Folch A., 2006. *A three-dimensional Eulerian model for transport and deposition of volcanic ashes.* Earth Planet. Sci. Lett. **241**, 634-647.

Curle N., 1955. *The influence of solid boundaries upon aerodynamic sound.* Proc. R. Soc. Lond. A231, 505-514.

Das I., Dennis J.E., 1998. *Normal-Boundary Intersection: A New Method for Generating Pareto Optimal Points in Multicriteria Optimization Problems.* SIAM J. Optim. **8**, 631-657.

Deb K., 2001. *Multi-objective Optimization Using Evolutionary Algorithms.* Wiley, Chichester, U.K., 497 pp.

Deihl T., Carlson F.R., 1968. *N waves from bursting balloons.* Am. J. Phys. **36** (5) 441-444.

Delle Donne D., Lacanna G., Marchetti E., Ripepe M., Ulivieri G., 2006. *Monitoring explosive volcanic activity using thermal images, Stromboli Volcano, Italy.* Eos Trans. AGU 87 (52) Fall Meet. Suppl., Abstract V43B-1795.

Diez M., Iemma U., Marchese V., 2007. *A sound-matching-based approach for aircraft noise annoyance alleviation via MDO.* AIAA Paper 2007-3667, in proc. of 13th AIAA/CEAS Aeroacoustics Conference, Rome, Italy.

Diez M., Iemma U., 2011. *Multidisciplinary conceptual design optimization of aircraft using a sound-matching-based objective function.* Eng. Optim., subm.

Donn W.L., Balachandran N.K., 1981. *Mount St. Helens eruption of 18 May 1980: Air waves and explosive yield.* Science **213**, 539-541.

Farassat F., Myers M.K., 1988. *Extension of the Kirchhoff's formula to radiation from moving surfaces.* J. Sound Vibr. **123** (3), 451-460.

Fee D., Garcés M.A., Steffke A., 2010. *Infrasound from Tungurahua Volcano 2006-2008: Strombolian to Plinian eruptive activity.* J. Volcanol. Geoth. Res. **19** (1-2), 67-81, doi:10.1016/j.jvolgeores.2010.03.006.

Fonseca C., Fleming P., 1995. *An overview of evolutionary algorithms in multiobjective optimization.* Evol. Comput. **3**, 1-18.

Foshag W.F., Gonzalez-Reyna J., 1956. *Birth and development of Paricutin volcano.* U.S. Geol. Surv. Bull. 965-D, 355-489.

Firstov P.P., Kravchenko N.M., 1996. *Estimation of the amount of explosive gas released in volcanic eruptions using air waves.* Volcanol. Seismol. **17**, 547-560.

Garcés M.A., 1997. *On the volcanic waveguide.* J. Volcanol. Geoth. Res. **102** (B10), 22,547-22,564.

Garcés M.A., McNutt. S.R., 1997. *Theory of the airborne sound field generated in a resonant magma conduit.* J. Volcanol. Geoth. Res. **78**, 155-178.

Garcés M.A., Hansen R.A., Lindquist K.G., 1998. *Traveltimes for infrasonic wave propagating in a stratified atmosphere.* Geophys. J. Int. **135**, 255-263.

Giacomelli L., Scandone R., 2007. *Vulcani d'Italia.* Liguori ed., Napoli, Italy, 475 pp.

Gorshkov G.S., 1960. *Determination of the explosion energy in some volcanoes according to barograms.* Bull. Volcanol. **23**, 141-144.

Gresta S., Ripepe M., Marchetti E., D'Amico S., Coltelli M., Harris A.J.L., Privitera E., 2004. *Seismoacoustic measurements during the July-*

August eruption of Mt. Etna volcano, Italy. J. Volcanol. Geotherm. Res. **137**, 219-230.

Hort M., Seyfried R., 1998. *Volcanic eruption velocities measured with a micro radar.* Geophys. Res. Lett. **25** (1), 113-116.

Iemma U., Marchese V., Gori R., 2009. *AcouSTO - a new open-source project for acoustic simulation.* 16th International Congress on Sound and Vibration, Cracovia, Polonia.

Iemma U. and Marchese V., *AcouSTO 1.3 User's Guide*, 2011.

Ingard U., 2008. *Notes on acoustics.* Infinity Science Pr Llc, Hingham, MA, US, 436 pp.

Jaupart C., Vergniolle S., 1988. *Laboratory models of Hawaiian and Strombolian eruptions.* Nature **331**, 58-60.

Johnson J.B., 2003. *Generation and propagation of infrasonic airwaves from volcanic explotions,.* J. Volcanol. Geoth. Res. **121**, 1-14.

Johnson J.B., 2007. *On the relation between infrasound, seismicity, and small pyroclastic explosions at Karymsky Volcano.* J. Geophys. Res. **112**, B08203, doi: 10.1029/2006JB004654.

Johnson J.B., Aster R., Jones K., Kyle P.R., McIntosh W.C., 2008. *Acoustic source characterization of impulsive Strombolian eruptions from the Mount Erebus lava lake.* J. Volcanol. Geoth. Res. **177**, 673-686.

Johnson J.B., Lees J., Varley N., 2011. *Characterizing complex eruptive activity at Santiaguito, Guatemala using infrasound semblance in networked arrays.* J. Volcanol. Geoth. Res. **199** (1-2), 1-14, doi: 10.1016/j.jvolgeores.-2010.08.005.

Kieffer S.W., 1977. *Sound Speed in Liquid-Gas Mixtures: Water-Air and Water-Steam.* J. Geophys. Res. **82** (20), 2895-2904.

Kieffer S.W., Sturtevant B., 1984. *Laboratory studies of volcanic jets.* J. Geophys. Res. **89** (B10), 8253-8268.

Kim I.Y., de Weck O.L., 2005. *Adaptive weighted-sum method for bi-objective optimization: Pareto front generation.* Struct. Multidisc. Optim. **29**, 149-158, doi:10.1007s00158-004-0465-1.

Kirkup S., 2007. *The Boundary Element Method in Acoustics.* Integrated Sound Software, 161 pp. Free e-book, http://www.boundary-element-method.com/.

Lacanna G., 2010. *Modeling the propagation of acoustic waves at the ground-atmosphere interface.* Ph.D. Thesis, University of Florence, Florence, Italy.

Landau L.D., Lifshitz E.M., 1987. *Fluid Mechanics: Volume 6 (Course of Theoretical Physics).* Pergamon Press, Oxford, 536 pp.

Landi P., Corsaro R.A., Francalanci L., Civetta L., Miraglia L., Pompilio M., Tesoro R. 2009. *Magma dynamics during the 2007 Stromboli eruption (Aeolian Islands, Italy):Mineralogical, geochemical and isotopic data.* J. Volcanol. Geoth. Res. **182**, 255-268, doi:10.1016/j.jvolgeores.2008.11.010.

Leehey P., Hanson C.E., 1971. *Aeolian tones associated with resonant vibration.* J. Sound Vibr. **13** (4), 465-483.

Lighthill M.J., 1952. *On sound generated aerodynamically, I: General Theory.* Proc. R. Soc., A211 (1107), 564-587.

Lighthill M.J., 1954. *On sound generated aerodynamically, II: Turbulence as a Source of Sound.* Proc. R. Soc., A222 (1148), 1-32.

Lighthill M.J., 1963. *Jet noise.* AIAA J. **1**, 1507-1517.

Lighthill M.J., 1978. *Waves in fluids.* Cambridge University Press, New York, NY, US, 504 pp.

Macedonio G., Pareschi M.T., Santacroce R., 1988. *A numerical simulation of the Plinian fall phase of 79 A.D. eruption of Vesuvius.* J. Geophys. Res. **93**, 14817-14827.

Macedonio G., Costa A., Longo A., 2005. *A computer model for volcanic ash fallout and assessment of subsequent hazard.* Comput. Geosci. **31**, 837-845.

Manneville A., Pilczer D., Spakovszky, Z.S., 2004. *Noise Reduction Assessments and Preliminary Design Implications for a Functionally-Silent Aircraft.* AIAA Paper 2004-2925, in proc. of 10th AIAA/CEAS Aeroacoustics Conference, Manchester, GB.

Marchetti E., Ripepe M., Harris A.J.L., Delle Donne D., 2009. *Tracing the differences between Vulcanian and Strombolian explosions using infrasonic and thermal radiation energy.* Earth Planet. Sci. Lett. **279**, 273-281, doi:10.1016/j.epsl.2009.01.004.

Matoza R.S., Fee D., Garcés M.A., Seiner J.M., Ramon P.A., Hedlin M.A.H., 2009. *Infrasonic jet noise from volcanic eruptions.* Geophys. Res. Lett. **36**, L08303, doi:10.1029/2009GL036486.

Meecham W.C., 1967. *Effect of Solid Boundaries on Aerodynamic Sound,.* J. Acoust. Soc. Am. **42** (5), 1159-1159.

Mikumo T., Bolt B.A., 1985. *Excitation mechanism of atmospheric pressure waves from the 1980 Mount St. Helens eruption.* Geophys. J. R. Astron. Soc. **81**, 445-461.

Morse P. M., Ingard K.U., 1968. *Theoretical Acoustics.* Princeton Univ. Press, Princeton, NJ, US, 927 pp.

Morton B., Taylor G.I., Turner J.S., 1956. *Turbulent gravitational convection from maintained and instantaneous sources.* Proc. R. Soc. **225**, 1-23.

Murase T., McBirney A.R., 1973. *Properties of Some Common Igneous Rocks and Their Melts at High Temperatures.* Geophys. Res. Lett., **21**, 749-752.

Ogden D.E., Wohletz K.H., Glatzmaier G.A., Brodsky E.E., 2008. *Numerical simulations of volcanic jets: Importance of vent overpressure.* J. Geophys. Res. **113**, B02204.

Özyörük Y., Long L.N., 1994. *A Navier-Stokes/Kirchhoff method for noise radiation from ducted fans.* AIAA Paper 1994-0462, in proc. of AIAA 32nd Aerospace Sciences Meeting, Reno, NV, US.

Pareto V., 1906. *Manuale di Economia Politica.* Società Editrice Libraria, Milano, Italy, 335 pp.

Parfitt E.A., Wilson L., 1995. *Explosive volcanic eruptions - IX. The transition between Hawaiian-style lava fountaining and Strombolian explosive activity.* Geophys. J. Int. **121**, 226-232.

Patrick M.R., Harris A.J.L., Ripepe M., Dehn J., Rothery D., Calvari S., 2007. *Strombolian explosive styles and source conditions: Insights from*

thermal (FLIR) video. Bull. Volcanol. **69**, 769-784. doi:10.1007/s00445-006-0107-0.

Pelanti M., 2005. *Wave propagation algorithms for multicomponent compressible flows with applications to volcanic jets.* Ph.D. Thesis, University of Washington, Seattle, WA, US.

Perret F.A., 1950. *Volcanological observations.* Carnegie Inst. Wash. Publ. 549, 126 pp.

Reed J.W., 1972. *Attenuation of blast waves by the atmosphere.* J. Geophys. Res. **77**, 1616-1622.

Reed J.W., 1977. *Atmospheric attenuation of explosion waves.* J. Acoust. Soc. Am. **61**, 39-47.

Richards A.F., 1963. *Volcanic sounds: Investigation and analysis.* J. Geophys. Res. **68**, 919-928.

Ripepe M., Poggi P., Braun T., Gordeev E., 1996, *Infrasonic waves and volcanic tremor at Stromboli.* Geophys. Res. Lett., **23**, 181-184.

Ripepe M., Gordeev E., 1999. *Gas bubble dynamics model for shallow volcanic tremor at Stromboli.* J. Geophys. Res. **104**, (B5) 10639-10654.

Ripepe M., Marchetti E., 2002. *Array tracking of infrasonic sources at Stromboli volcano.* Geophys. Res. Lett. **29** (22) 2076, doi: 10.1029/2002GL-015452.

Ripepe M., Poggi P., Marchetti E., 2004. *Small aperture infrasonic array monitors activity at Stromboli volcano.* Inframatics **7**, 1-14.

Ripepe M., De Angelis S., Lacanna G., Poggi P., Williams C., Marchetti E., Delle Donne D., Ulivieri G., 2009a. *Tracking Pyroclastic Flows at Soufrière Hills Volcano.* Eos Trans. AGU, 90, 27, 229-236.

Ripepe M., Delle Donne D., Lacanna G., Marchetti E., Ulivieri G., 2009b. *The onset of the 2007 Stromboli effusive eruption recorded by an integrated geophysical network.* J. Volcanol. Geoth. Res. **182**, (3-4), 131-136.

Scandone R., Giacomelli L., 1998. *Vulcanologia.* Liguori ed., Napoli, Italy, 660 pp.

Scharff L., Hort M., Harris A.J.L., Ripepe M., Lees J.M., Seyfried R., 2008. *Eruption dynamics of the SW crater of Stromboli volcano, Italy - An interdisciplinary approach.* J. Volcanol. Geoth. Res. **176**, 565-570.

Searcy C., Dean K., Stringer W., 1998. *PUFF: A high resolution volcanic ash tracking model.* J. Volcanol. Geoth. Res. **80**, 1-16.

Seyfried R., Hort M., 1999. *Continuous monitoring of volcanic eruption dynamics: a review of various techniques and new results from a frequency-modulated radar Doppler system.* Bull. Volcanol. **60**, 627-639.

Snodgrass J.M., Richards A.F., 1956. *Observations of underwater volcanic acoustics at Barcena volcano, San Benedicto Island, Mexico, and Shelikof Strait, Alaska.* Trans., Am. Geophys. Union **37**, 97-104.

Sparks R.S.J., Bursik M.I., Carey S.N., Gilbert J.S., Glaze L.S., Sigurdsson H., Woods A.W., 1997. *Volcanic Plumes.* John Wiley & Sons, Chichester, UK, 574 pp.

Sutherland L.C., Bass H.E., 2004. *Atmospheric absorption in the atmosphere up to 160 km.* J. Acoust. Soc. Am. **115**, 1012-1032.

Tahira M., Nomura M., Sawada Y., Kamo K., 1996. *Infrasonic and acoustic-gravity waves generated by the Mount Pinatubo eruption of June 15, 1991.* Fire and Mud. University of Washington Press, Seattle, 601-614.

Tam C.K.W., 1998. *Jet noise: Since 1952.* Theor. Comput. Fluid Dyn. **10**, 393-405.

Tam C.K.W., Golebiowski M., Seiner J.M., 1996. *On the two components of turbulent mixing noise from supersonic jets.* AIAA Paper 96-1716.

Ulivieri G., Delle Donne D., Lacanna G., Marchetti E., Ripepe, M., 2008. *Infrasonic analysis of Strombolian explosions and fire fountaining at Etna Volcano.* AGU, Fall Meet. Suppl., Abstract V51E-2090.

Vergniolle S., Jaupart C., 1986. *Separated two-phase flow and basaltic eruptions.* J. Geophys. Res. **91** (B12), 12,842-12,860.

Vergniolle S., Jaupart C., 1990. *Dynamics of degassing at Kilauea Volcano, Hawaii.* J. Geophys. Res. **95**, 2793-2809.

Vergniolle S., Brandeis G., 1994. *Origin of the sound generated by Strombolian explosions.* Geophys. Res. Lett. **21**, 1959-1962.

Vergniolle S., Brandeis G., 1996. *Strombolian explosions: A large bubble breaking at the surface of a lava column as a source of sound.* J. Geophys. Res. **101** (9), 20433-20448.

Vergniolle S., Brandeis G., Mareschal J.-C., 1996. *Strombolian explosions: Eruption dynamics determined from acoustic measurements.* J. Geophys. Res. **101** (9), 20449-20466.

Vergniolle S., Boichu M., Caplan-Auerbach J., 2004. *Acoustic measurements of the 1999 basaltic eruption of Shishaldinvolcano, Alaska: 1) Origin of Strombolian activity.* J. Volcanol. Geotherm. Res. **137**, 109-134.

Vergniolle S., Caplan-Auerbach J., 2004. *Acoustic measurements of the 1999 basaltic eruption of Shishaldin volcano, Alaska: 2) Precursor to the Subplinian activity.* J. Volcanol. Geotherm. Res. **137**, 135-151.

Vergniolle S., Caplan-Auerbach J., 2006. *Basaltic Subplinian plumes and thermals: constraints from acoustic measurements at Shishaldin volcano, Alaska.* Bull. Volcanol. **68**, 611-630.

Wilson L., Sparks R.S.J., Huang T.C., Watkins N.D., 1978. *The Control of Volcanic Column Heights by Eruption Energetics and Dynamics.* J. Geophys. Res. **83** (B4), 1829-1836.

Wilson L., 1980. *Relationships between pressure, volatile content and ejecta velocity in three types of volcanic explosion.* J. Volcanol. Geotherm. Res. **8**, 297-313.

Wilson L., Sparks R.S.J., Walker G.P.L., 1980. *Explosive volcanic eruptions - IV. The control of magma properties and conduit geometry on eruption column behaviour.* Geophys. J. R. astr. Soc. **63**, 117-148.

Woulff G., McGetchin T.R., 1976. *Acoustic noise from volcanoes: Theory and experiments.* Geophys. J. R. Astron. Soc. **45**, 601-616.

Zadeh L., 1963. *Optimality and Non-Scalar-Valued Performance Criteria.* IEEE Trans. Autom. Control. **8**, 59-60.

Acknowledgements

I would like to express my gratitude to my tutor Prof. Roberto Scandone for the support during these three years, and for his advices about the physics on volcanism.

I am grateful to Prof. Umberto Iemma for the great enthusiasm demonstrated in testing his code for this volcanological application....and for introducing me to Fosco Maraini!

I would to thank Prof. Maurizio Ripepe for providing me the experimental data used in this thesis, and for our helpful discussions on volcano acoustics.

I am also thankful to Dario Delle Donne for the help during data analysis, his friendship, and for the "couch surfing"!

I am sincerely grateful to Cecilia Leotardi and Lorenzo Burghignoli for the help in the development of the optimization and for supporting me during the most intense months of this PhD.

I also would like to thank the people with whom I collaborated over these years. Prof. Wolfango Plastino for the scientific research in environmental radioactivity. Prof. Aldo Altamore, Enrico Bernieri and Paolo Aloe for the education and outreach projects.

I would like to say thank you to my dear friend Paolo Montini who shared with me these three years of PhD, and to Lorenzo and Ivan for bearing me in the "aquarium".

I am definitely grateful to my parents for their constant help, and to my grandfather for believing in me.

My most sincere gratitude goes to my lovely Serena who tirelessly supported me every day, providing me energy in the moments of difficulty.

Thanks to my great Teachers for their precious presence in my life. May the light of their wisdom spread in all directions!